

# Fluctuations in Quantum Degenerate Fermi Gases

# Fluctuations in Quantum Degenerate Fermi Gases

by

Christian Sanner

## Abstract

Ultracold neutral Fermi gases provide a novel platform for the experimental quantum simulation of correlated many-body systems. The study of fluctuations and correlations in Fermi gases and the development of appropriate measurement methods are the subject of this thesis.

Spatial atom noise analysis performed for expanded clouds of an ideal Fermi gas reveals Pauli suppression of density fluctuations for cold gas samples deep in the quantum degenerate regime. Measuring the level of suppression provides sensitive thermometry at low temperatures.

Spin fluctuations and density fluctuations are studied for a two-component gas of strongly interacting fermions along the Bose-Einstein condensate - BCS crossover. This is done by in situ imaging of dispersive speckle patterns. Compressibility and magnetic susceptibility are determined from the measured fluctuations. Speckle imaging easily resolves a tenfold suppression of spin fluctuations below shot noise, and can be universally applied to trapped quantum gases.

A degenerate Fermi gas is rapidly quenched into the regime of strong effective repulsion near a Feshbach resonance. The spin fluctuations are monitored using speckle imaging and, contrary to several theoretical predictions, the samples remain in the paramagnetic phase for an arbitrarily large scattering length. Over a wide range of interaction strengths a rapid decay into bound pairs is observed over times on the order of a few Fermi times, preventing the study of equilibrium phases of strongly repulsive fermions. This suggests that a Fermi gas with strong short-range repulsive interactions does not undergo a ferromagnetic phase transition.

December 2012

## **Acknowledgments**

Having too much stress in your life? Go visit the zoo! Building 26 floor 2 is a zoo. It is a marvelous zoo, a microcosm of scientific leisure almost completely shielded from all annoyances that normally constrain life. Being one of the shy animals I am very thankful to the zookeeper for letting me hide from visitors, cookie hours, daylight, seminars and other forms of harsh reality. I am thankful to Wolfgang for a lot of other things.

MIT is a research institute and not a Zen eldorado, but most of the time it felt like it anyway. This is because of the patience and humility of many people that I had the privilege to work with over the years. Many thanks to all my wonderful colleagues, among them in particular Jit Kee Chin, Dan Miller, Marko Cetina, Yingmei Liu, Widagdo Setiawan, Aviv Keshet, Edward Su, Ralf Gommers, Yong-il Shin, Wujie Huang and Jonathon Gillen. Thank you also for mostly sharing a passion for terminated photodiodes!

Special thanks to Markus Oberthaler and Selim Jochim.

Finally I am thankful to Conrad Fischer, Larry Hagman, Friedrich Küppersbusch, Paul Pranzo, Saint Bruno of Cologne, Louise Clancy, Jerry Shine, Yuri Gagarin, Mother Teresa, Heiner Müller, Heinz Heimsoeth, Richard Slotkin, Justin Pierce, Princess Leia and Luke Skywalker for providing insight beyond imagination. Ahoy!

# Contents

<b>1</b>	<b>Introduction</b>	<b>7</b>
1.1	Mean values and fluctuations . . . . .	8
1.1.1	Why is the physics of fluctuations interesting? . . . . .	8
1.2	Fluctuations and experiments with cold atoms . . . . .	9
1.2.1	New ways to probe interesting quantum phases . . . . .	9
1.2.2	Noise and correlation measurements - The state of the field . .	10
1.2.3	A universal approach to noise measurements - Synopsis and outline . . . . .	11
<b>2</b>	<b>Theory of fluctuations in Fermi gases</b>	<b>14</b>
2.1	The fluctuation-response relation . . . . .	14
2.2	Bosons vs. Fermions - Different noise properties . . . . .	17
2.3	Density fluctuations in a non-interacting Fermi gas . . . . .	18
2.3.1	Large probe volume limit . . . . .	18
2.3.2	Small probe volume limit . . . . .	20
2.4	Fluctuations in an interacting Fermi gas . . . . .	23
2.5	Density fluctuations and light scattering . . . . .	25
<b>3</b>	<b>Measuring fluctuations in an ideal Fermi gas</b>	<b>27</b>
3.1	Measurements in trap and after ballistic expansion . . . . .	28
3.2	The experimental procedure . . . . .	30
3.2.1	Fermi gas apparatus . . . . .	30
3.2.2	Sample preparation . . . . .	31

3.3	How to count atoms in a box - Experimental challenges and constraints	33
3.3.1	Different imaging methods . . . . .	33
3.3.2	Atom noise and other noise sources . . . . .	35
3.3.3	Nonlinear effects and other limitations . . . . .	42
3.4	The imaging system for noise measurements . . . . .	46
3.4.1	Overview of the imaging system . . . . .	47
3.4.2	Detector optimization for noise measurements . . . . .	50
3.4.3	Further improvement strategies - Coherent vs. incoherent illumination . . . . .	56
3.4.4	Depth of field considerations . . . . .	60
3.5	Data acquisition and analysis . . . . .	61
3.5.1	Horizontal statistics vs. vertical stack analysis . . . . .	62
3.5.2	The vertical noise measurement procedure . . . . .	64
3.5.3	Scattering cross section calibration . . . . .	66
3.6	Measurement results and interpretation . . . . .	68
3.6.1	Comparison of theory and experiment . . . . .	68
3.6.2	Atom counting contrast saturation . . . . .	70
3.6.3	Noise in the noise . . . . .	71
<b>4</b>	<b>Measuring fluctuations in a strongly interacting Fermi gas</b>	<b>73</b>
4.1	Properties of an interacting two component Fermi gas . . . . .	74
4.1.1	From elastic collisions to Feshbach resonances . . . . .	74
4.1.2	A Fermi gas in the unitary limit . . . . .	75
4.2	In-situ noise measurements - Advantages and challenges . . . . .	79
4.2.1	A short review of Fourier optics . . . . .	80
4.2.2	Dispersive imaging . . . . .	81
4.2.3	Initial experimental strategy . . . . .	84
4.3	From laser speckle to speckle imaging . . . . .	86
4.3.1	Laser speckle . . . . .	86
4.3.2	Out-of-focus speckle . . . . .	87

4.4	Data acquisition and analysis . . . . .	89
4.4.1	Experimental setup and sample preparation . . . . .	89
4.4.2	Noise extraction and mapping procedure . . . . .	90
4.4.3	Determination of the superfluid to normal phase boundary . . . . .	94
4.5	Results and interpretation . . . . .	95
<b>5</b>	<b>Exploring correlations in a repulsively interacting Fermi gas</b>	<b>98</b>
5.1	Ferromagnetic instability of a repulsive Fermi gas . . . . .	98
5.1.1	The critical interaction strength . . . . .	100
5.1.2	Pairing instability vs. ferromagnetic instability . . . . .	101
5.2	Experimental strategy . . . . .	102
5.3	Experimental results - Discussion and interpretation . . . . .	104
5.3.1	Spin fluctuation measurements . . . . .	104
5.3.2	Pair formation measurements . . . . .	105
5.3.3	Rate comparison . . . . .	107
5.3.4	Temperature considerations . . . . .	108
5.3.5	Kinetic energy and release energy . . . . .	109
5.3.6	Time scales for domain growth vs. experimental resolution . . . . .	112
5.4	Conclusions . . . . .	113
<b>6</b>	<b>Conclusions and outlook</b>	<b>115</b>
<b>A</b>	<b>Suppression of Density Fluctuations in a Quantum Degenerate Fermi Gas</b>	<b>117</b>
<b>B</b>	<b>Speckle Imaging of Spin Fluctuations in a Strongly Interacting Fermi Gas</b>	<b>122</b>
<b>C</b>	<b>Correlations and Pair Formation in a Repulsively Interacting Fermi Gas</b>	<b>127</b>

# Chapter 1

## Introduction

The field of ultracold quantum gases continues to expand. Bose-Einstein condensation of dilute alkali vapors [1, 2] opened up a multitude of research possibilities and led eventually to the experimental study of quantum degenerate Fermi gases [3] and new phases in optical lattices [4]. Particularly in this context it is evident that the expansion of the field is not mere diversification. Instead, cold quantum gases are becoming a model system to investigate universal physics [5] and to address long-standing questions relevant for solid state many-body systems [6].

The experiments described in this thesis follow this concept. Individually they demonstrate fundamental effects of quantum mechanics, reveal pair correlations in a superfluid and attempt to investigate the possibilities for itinerant ferromagnetism in a strongly interacting quantum gas. However, altogether they want to contribute towards the implementation of a quantum simulator for solid state systems.

This chapter will provide a motivation and general introduction to fluctuation and correlation experiments with cold atoms.

## 1.1 Mean values and fluctuations

### 1.1.1 Why is the physics of fluctuations interesting?

Every experimentalist is confronted with fluctuations in the quantity of interest. Often these fluctuations have a technical origin, e.g. uncertainties caused by residual mechanical vibrations in a measurement setup, and contribute to the error budget of the experiment. In the absence of technical noise the outcome of a measurement is typically still noisy, but now the noise reflects fundamental properties of the studied system.

Measuring the voltage drop across an electrical resistor is a good example. Initially technical noise in the measurement device - for instance an oscilloscope - might be the limiting factor, but eventually one finds that irreducible forms of noise are associated with every resistor. The random thermal motion of the charge carriers in the conductor gives rise to thermal Johnson noise, and for very low currents through the resistor the quantization of charge results in significant shot noise type statistical fluctuations of the current [7].

However, identifying the physical origins of a noise effect is not only insightful on the level of a particular system. It rather leads to the understanding of a very fundamental relation between the fluctuations in any thermodynamic system at equilibrium and the response of the system to applied external forces. This relation, explicated as the fluctuation-dissipation theorem [8], allows one vice versa to determine relevant thermodynamic quantities without affecting the equilibrium: One can interpret fluctuations as being caused by spontaneous infinitesimal perturbations constantly probing the response of the system. Fluctuations are not just a distraction from the mean values, they carry additional information.

From a historical viewpoint the discovery and explanation of Brownian motion [9] is another very prominent example for the relevance and impact of understanding noise effects in physics. Like the thermal noise in a resistor Brownian motion can be analyzed and interpreted within the framework of the fluctuation-dissipation theorem. Again the system's response to an applied force is linked to thermally driven

microscopic fluctuations. Many years before a general formulation of the fluctuation-dissipation theorem was given, Einstein [10] and Smoluchowski [11] carefully modeled Brown's experimental observations. They derived via statistical mechanics the connection between the kinetic noise of erratically moving microscopic particles characterized by the diffusion constant  $D = \langle(\Delta x)^2\rangle/(2t)$ , i.e. mean square displacement per time  $t$ , and a mobility parameter  $\mu = v_d/F$  that quantifies the particles' mean drift velocity  $v_d$  under the influence of an externally applied force  $F$ . By finding

$$D = \mu k_B T \tag{1.1}$$

with  $k_B$  being the Boltzmann constant and  $T$  being the absolute temperature, Einstein and Smoluchowski wrote down an early version of the fluctuation-dissipation theorem.

Many more examples - in particular exciting recent developments like squeezed quantum states [12] - could be given to further motivate the exploitation of noise phenomena, but in the focus of this thesis is the application of noise measurements in the context of many-body physics with ultracold quantum gases.

## 1.2 Fluctuations and experiments with cold atoms

### 1.2.1 New ways to probe interesting quantum phases

Given the universal relevance of fluctuations it is not surprising that they can also play an important role in the field of cold atoms. Consider for instance a three-dimensional optical lattice loaded with a two-component interacting Fermi gas so that there is on average one atom per lattice site. Assuming appropriate values for temperature, lattice depth and interaction strength it is expected that such a system undergoes a phase transition to a Mott insulating [13] and an antiferromagnetic [14] state as depicted in Fig. 1-1. Diagnosing these phase transitions can be challenging because the mean density distribution of one atom per lattice site (i.e. half filling in a

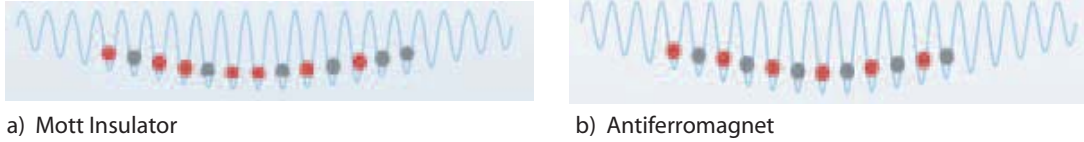


Figure 1-1: Illustration of atom distributions in an optical lattice for a) a Mott insulating state and b) an antiferromagnetic state. The red and gray dots represent atoms of the two different spin components. Both quantum states have exactly one atom per lattice site. While the Mott insulator randomly assigns the spin state for each site, the antiferromagnet is an ordered system alternating between the two spin components.

system with two spin components) is not changing. However, by measuring differential density fluctuations the various states can easily be distinguished. With  $n_1$  ( $n_2$ ) being the number density of spin component 1 (2) it is clear that both quantum phases exhibit suppressed noise for the sum density  $n_1 + n_2$ . But while the Mott insulator will show fluctuations in the difference density  $n_1 - n_2$ , they will be suppressed for the antiferromagnet.

Although noise measurements are not the only method to experimentally identify these quantum phases, developing the ability to precisely measure fluctuations is going to be a significant advantage at the ultracold atoms research frontier.

### 1.2.2 Noise and correlation measurements - The state of the field

Over the past decade progress has been made towards accessing the wealth of information hidden in the density fluctuations and correlations of ultracold gases. Several experiments successfully demonstrated the deterministic sub-Poissonian preparation of small clouds of bosons with typically a few hundred atoms [15, 16, 17, 18].

In 2004 Altman et al. [19] suggested to directly reveal density-density correlations by carefully analyzing the atom shot noise in the image of an expanding gas cloud. Their proposal led to experiments that reported the atom shot noise resolved detection of local and nonlocal pair correlations between the constituents of dissociated weakly bound Feshbach molecules [20]. Furthermore, following similar concepts

Fölling et al. [21] and Rom et al. [22] could find density correlations in images of gas clouds released out of an optical lattice potential. The obtained correlations in momentum space are a consequence of the momentum projection happening when the periodic lattice potential is abruptly switched off. Accordingly, after ballistic expansion the correlations are revealed in the spatial frequency domain by calculating the two-dimensional autocorrelation functions of the density distributions and averaging appropriately.

In a more recent experiment [23] studying a two-dimensional Mott-insulator of bosonic Caesium atoms it was possible to directly observe in a spatially resolved way the reduction of number fluctuations accompanying the incompressible Mott state. A localized atom counting in repeated absorption images was performed to obtain the number statistics. In this regard this experiment was paradigmatic for a new generation of cold atoms experiments that can now provide single-site resolved imaging of atoms in optical lattices allowing high fidelity atom counting and statistics [24].

All approaches mentioned here delivered insight into interesting quantum states by employing noise or fluctuation related measurements. However, they all rely in some way on specialized preparation schemes, two-dimensional confinement geometries or other requirements. The work presented in this thesis wants to further expand the applicability of noise measurements by introducing and demonstrating a simple experimental infrastructure for universal fluctuation measurements in ultracold atoms systems.

### **1.2.3 A universal approach to noise measurements - Synopsis and outline**

Measurements of an observable  $A$  in a system at thermal equilibrium fluctuate around their expectation value  $\langle A \rangle$ . These fluctuations  $\Delta A$  are a fundamental property of the system and can be linked via the fluctuation-dissipation theorem to corresponding thermodynamic susceptibilities. Applying a small external force to a system and

observing its response in the conjugate quantity is equivalent to measuring the fluctuations of the system at equilibrium. Assuming that  $A$  stands for the volume-integral of a density one finds that for large macroscopic subsystems of volume  $V$  the relative fluctuations  $\Delta A/\langle A \rangle$  are usually proportional to  $\sqrt{V}/V$  and therefore negligibly small and hidden in the experimental noise floor.

This also applies to typical experiments in the field of cold atoms. When analyzing the density distribution in clouds of cold gases the thermodynamic limit is assumed and relevant quantities are derived from spatially resolved measurements of  $\langle A \rangle$ . However, recently several experiments have demonstrated that fluctuations and more generally correlations are experimentally directly accessible. In particular for neutral fermions observations of pair-correlations [20], Hanbury Brown and Twiss-type anti-correlations [21] and local antibunching [22] in the noise have been reported.

This thesis introduces a universal experimental strategy to measure fluctuations in ultracold gases and demonstrates several applications. First, a theoretical overview about fluctuations in Fermi gases is given in the next chapter. A brief discussion of the fluctuation-dissipation theorem and a comparison between bosonic and fermionic systems is followed by a derivation of density fluctuations for non-interacting fermions. Subsequently the effects of interactions and the relation between density fluctuations and light scattering properties are discussed.

The third chapter focuses on the experimental demonstration of Pauli suppression of density fluctuations in a quantum degenerate ideal Fermi gas of  ${}^6\text{Li}$  atoms. This well-understood ideal gas makes it possible to directly observe the dramatic unobstructed consequences of Fermi statistics at low temperature and it serves at the same time as a clean test system for the noise measurements performed on an expanded gas cloud. A detailed account of the experimental methods is provided and the measurement results are quantitatively analyzed.

Chapter four presents a modified and extended version of the fluctuation measurements called speckle imaging, adapted to trapped samples of interacting gases and allowing balanced detection in a two-component mixture, i.e. accessing  $\Delta(n_1 - n_2)$

directly without measuring the densities  $n_1$  and  $n_2$  of the two components individually. The underlying principles of this new method, in particular aspects of dispersive imaging and the role of laser speckle, are discussed extensively. Speckle imaging is applied to a strongly interacting Fermi gas in the BEC-BCS crossover and resulting measurements of spin  $\Delta(n_1 - n_2)$  and density fluctuations  $\Delta(n_1 + n_2)$  are reported. By means of the fluctuation-dissipation theorem these quantities are mapped to the magnetic susceptibility and the compressibility of the gas. A short review of Landau's Fermi liquid theory contributes to a further interpretation of the results.

As another application of speckle imaging chapter five reports on the measurement of correlations and pair formation in a repulsively interacting Fermi gas. Starting from a previous publication [25] that had found evidence for itinerant ferromagnetism in a Fermi gas with repulsive interactions but could not determine the size of the ferromagnetic domains, speckle imaging was utilized to clarify the previous measurements and look for domain growth. After an introduction to the concept of itinerant ferromagnetism and a discussion about the special features of a metastable Fermi gas with repulsive interactions, the connection between domain size and spin noise enhancement is exemplified and the experimental constraints are described, particularly emphasizing the fast switching of interaction strengths. Given the surprising result that no significant domain growth was found, a detailed discussion of the competition between domain formation and pairing instability follows.

Finally conclusions and an outlook for future noise experiments are presented. Three appendices containing printouts of relevant publications conclude the thesis.

# Chapter 2

## Theory of fluctuations in Fermi gases

### 2.1 The fluctuation-response relation

In view of its universal character it is appropriate to begin the theoretical overview of fluctuations in Fermi gases with a short review of the fluctuation-dissipation theorem. Rather than discussing it in a more general form assuming frequency-dependent dynamic susceptibilities, its static precursor, the fluctuation-response relation, is introduced emphasizing the aspects particularly relevant for the purpose of this thesis. A general derivation at full length can be found in [26].

Consider a thermodynamic system with Hamiltonian  $H$  and an external force  $f$  with corresponding conjugate operator  $\hat{A}$  and  $[\hat{A}, H] = 0$ . Examples for such forces are a magnetic field or a tension, corresponding to magnetic moment or length operators for  $\hat{A}$ . The density matrix of such a system can be written as

$$\rho = \frac{e^{-\beta(H-f\hat{A})}}{\mathbf{Tr} e^{-\beta(H-f\hat{A})}} = e^{-\beta(H-f\hat{A}-K)} \quad (2.1)$$

with the generalized potential  $K$  defined via  $e^{\beta K} = 1/\mathbf{Tr} e^{-\beta(H-f\hat{A})} = 1/\mathcal{Z}$  and  $\beta = 1/k_B T$ , where  $\mathcal{Z}$  denotes the partition function,  $k_B$  the Boltzmann constant and

$T$  the absolute temperature. Under the influence of the external force the value of a variable  $B$  is then calculated as

$$B = \langle \hat{B} \rangle = \mathbf{Tr} [\rho \hat{B}] = \mathbf{Tr} [\hat{B} e^{-\beta(H-f\hat{A})} e^{\beta K}]. \quad (2.2)$$

The differential change of  $B$  with  $f$  is therefore

$$\frac{\partial B}{\partial f} = \beta \mathbf{Tr} [\hat{B} \hat{A} \rho] + \frac{\partial e^{\beta K}}{\partial f} \mathbf{Tr} [\hat{B} e^{-\beta(H-f\hat{A})}] = \beta \mathbf{Tr} [\hat{B} \hat{A} \rho] + \beta \frac{\partial K}{\partial f} \mathbf{Tr} [\hat{B} \rho], \quad (2.3)$$

which turns with

$$\frac{\partial K}{\partial f} = -\frac{1}{\beta} \frac{\partial \ln \mathcal{Z}}{\partial f} = -\frac{1}{\beta \mathcal{Z}} \beta \mathbf{Tr} [\hat{A} e^{-\beta(H-f\hat{A})}] = -\mathbf{Tr} [\hat{A} \rho] = -\langle \hat{A} \rangle \quad (2.4)$$

into

$$\frac{\partial B}{\partial f} = \frac{1}{k_B T} [\langle \hat{B} \hat{A} \rangle - \langle \hat{B} \rangle \langle \hat{A} \rangle] = \frac{1}{k_B T} \langle \hat{B} \hat{A} \rangle_C. \quad (2.5)$$

The last equation - often called fluctuation-response theorem - relates in a thermodynamic system the correlation  $\langle \hat{B} \hat{A} \rangle_C$  to the differential susceptibility  $\chi = \partial B / \partial f$  that characterizes the system's response to the external force.

Assuming that the operators represent extensive quantities of order  $\mathcal{O}(N^1)$ , e.g. the particle number  $N$  itself, and the derivative is taken with respect to an intensive quantity of order  $\mathcal{O}(N^0)$ , e.g. the chemical potential  $\mu$ , one typically expects correlations of order  $\mathcal{O}(N^1)$ . In other words, for macroscopic systems with microscopic interactions density-density correlations are expected to be of order  $\mathcal{O}(N^1)$  and therefore  $\Delta N = \mathcal{O}(N^{1/2})$ . Systems undergoing a phase transition or developing long-range order by other means can exhibit very different behaviors [27, 28].

To continue with the above example suppose  $\hat{A} = \hat{B} = \hat{N}$  in an open system, where  $N$  is the number of particles. As mentioned the grand-canonical ensemble identifies the corresponding force as the chemical potential  $\mu$  and (2.5) reads

$$\frac{\partial N}{\partial \mu} = \frac{1}{k_B T} \langle \hat{N}^2 \rangle_C = \frac{1}{k_B T} (\Delta N)^2. \quad (2.6)$$

Employing the Maxwell relations shows  $\partial N / \partial \mu = V n \partial n / \partial p = \kappa_T N^2 / V$  with volume  $V$ , density  $n = N/V$ , pressure  $p$  and isothermal compressibility  $\kappa_T$ , leading to

$$\frac{1}{n k_B T} \frac{(\Delta N)^2}{N} = \kappa_T. \quad (2.7)$$

Equation (2.7) represents a well-known result from the grand-canonical ensemble, connecting the relative number fluctuations  $(\Delta N)^2 / N$  with the corresponding susceptibility, i.e. the isothermal compressibility  $\kappa_T$ . This makes it possible to determine the compressibility by measuring the fluctuations. For a classical ideal gas the fluctuations are directly obtained from<sup>1</sup>

$$(\Delta N)^2 = \int d^3 \mathbf{r}_1 d^3 \mathbf{r}_2 \langle \rho(\mathbf{r}_1) \rho(\mathbf{r}_2) \rangle_C = V \int d^3 \mathbf{r} \langle \rho(\mathbf{r}) \rho(0) \rangle_C = V n, \quad (2.8)$$

which recovers together with (2.6) the ideal gas law  $pV = Nk_B T$ .

---

<sup>1</sup>For a homogeneous system  $\langle \rho(\mathbf{r}_1) \rho(\mathbf{r}_2) \rangle_C$  only depends on the relative distance  $\mathbf{r} = \mathbf{r}_1 - \mathbf{r}_2$ . Furthermore, for the ideal gas the conditional probability to find an atom at  $\mathbf{r}$  given that there is an atom at the origin is  $\delta(\mathbf{r}) + n$ . Therefore  $\langle \rho(\mathbf{r}) \rho(0) \rangle = n (\delta(\mathbf{r}) + n)$ , where  $\rho(\mathbf{r})$  denotes the probability to find an atom at position  $\mathbf{r}$ . For more details about the explicit calculation of correlations confer [29, 30].

## 2.2 Bosons vs. Fermions - Different noise properties

Despite focusing on Fermi gases, it is often insightful to compare the different consequences of Bose and Fermi statistics. Along the lines of the previous paragraph the fluctuations for an ideal quantum gas can be obtained by differentiating the corresponding thermodynamic potentials. More explicitly, keeping the notation and assuming  $\hat{A} = \hat{B}$ , equations (2.4) and (2.5) lead to

$$-\frac{\partial^2 K}{\partial f^2} = \frac{\partial \langle \hat{A} \rangle}{\partial f} = \frac{1}{k_B T} \langle \hat{A}^2 \rangle_C \quad (2.9)$$

with the potential  $K = -k_B T \ln \mathcal{Z}$ . In the framework of the occupation number formalism, the partition function  $\mathcal{Z}$  of an ideal quantum gas is given by

$$\ln \mathcal{Z} = \frac{1}{a} \sum_{k=1}^{\infty} \ln[1 + a e^{-\beta(\epsilon_k - \mu)}]. \quad (2.10)$$

Here  $k$  is indexing the single-particle states with eigenenergies  $\epsilon_k$  and the constant  $a$  specifies the particular distribution, i.e.  $a = 1$  for the Fermi-Dirac distribution,  $a = -1$  for the Bose-Einstein distribution and  $a = 0$  (interpreted as  $\lim_{a \rightarrow 0}$ ) for the classical Maxwell-Boltzmann distribution.

By identifying  $f$  with the energy  $\epsilon_k$  and the corresponding  $\hat{A}$  with the occupation number operator  $-\hat{n}_k$ , equation (2.9) can be applied to these distributions yielding for the occupation number fluctuations

$$\sigma_{n_k}^2 = \langle \hat{n}_k^2 \rangle - \langle \hat{n}_k \rangle^2 = -k_B T \frac{\partial^2 K}{\partial f^2} = k_B T \frac{\partial \langle \hat{A} \rangle}{\partial f} = -k_B T \frac{\partial}{\partial \epsilon_k} \langle \hat{n}_k \rangle. \quad (2.11)$$

Together with the well-known expectation values for the occupation numbers

$$\langle \hat{n}_k \rangle = n_k = \frac{1}{e^{\beta(\epsilon_k - \mu)} + a}, \quad (2.12)$$

equation (2.11) results in

$$\sigma_{n_k}^2 = \frac{e^{\beta(\epsilon_k - \mu)}}{[e^{\beta(\epsilon_k - \mu)} + a]^2} = \langle \hat{n}_k \rangle - a \langle \hat{n}_k \rangle^2, \quad (2.13)$$

i.e. compared to a classical Maxwell-Boltzmann gas ( $a = 0$ ) the fluctuations are enhanced for a Bose gas ( $a = -1$ ) and suppressed for a Fermi gas ( $a = 1$ ).

By examining an individual single-particle state  $k$ , the last result becomes very intuitive for Fermions: The probability  $p$  to find the state occupied with exactly one Fermion is  $p = \langle \hat{n}_k \rangle$ , no Fermion is found with probability  $1 - p$ . This binomial distribution has obviously a variance  $\sigma^2 = p(1 - p)$ , in agreement with equation (2.13). For small probabilities, i.e. high temperatures  $e^{\beta\mu} \ll 1$ , one finds  $\sigma^2 \approx \langle \hat{n}_k \rangle$ , resembling the classical result.

So far this introduction to noise properties focused on occupation number fluctuations, but a typical *in situ* experiment would rather measure density fluctuations. In the language of the discussion above one has to integrate the binomial variance  $\langle \hat{n}_k \rangle(1 - \langle \hat{n}_k \rangle)$  over all momentum states  $k$  in the local Fermi sea.

## 2.3 Density fluctuations in a non-interacting Fermi gas

### 2.3.1 Large probe volume limit

Following the above proposal the number variance in a large<sup>2</sup> subvolume  $V$  of a homogeneous non-interacting Fermi gas is

---

<sup>2</sup>large compared to the inverse momentum width of the Fermi surface, i.e.  $\delta k V^{1/3} \gg 1$  with  $\delta k$  defined via  $\hbar^2 k_F \delta k / m = k_B T$  and Fermi wave vector  $k_F$

$$\sigma_N^2 = \sum_k n_k(1 - n_k) \approx \frac{V}{(2\pi)^3} \int d^3k n_k(1 - n_k) \quad (2.14)$$

and the integral can be evaluated by substituting  $\epsilon_k = \hbar \vec{k}^2 / (2m)$ . This leads to

$$\sigma_N^2 = \frac{2\pi V}{h^3} (2m)^{3/2} \int \epsilon^{1/2} d\epsilon n_k(1 - n_k) \quad (2.15)$$

with particle mass  $m$  and Planck's constant  $h$ .

To obtain the same result one can alternatively start from equation (2.6) and straightforwardly calculate  $\partial N / \partial \mu$  in the grand-canonical ensemble.  $N$  as a function of temperature, volume and fugacity  $z = e^{\beta\mu}$  is readily given by

$$N = \sum_k \langle n_k \rangle \approx \frac{2\pi V}{h^3} (2m)^{3/2} \int_0^\infty d\epsilon \frac{\epsilon^{1/2}}{z^{-1} e^{\beta\epsilon} + 1} \quad (2.16)$$

and to streamline subsequent calculations it is useful to rewrite the last equation as

$$N = V/\lambda^3 f_{3/2}(z) \quad (2.17)$$

with the thermal wavelength  $\lambda = h/\sqrt{2\pi m k_B T}$  and the integral expression

$$f_n(z) = -\text{Li}_n(-z) = \frac{1}{\Gamma(n)} \int_0^\infty dx \frac{x^{n-1}}{z^{-1} e^x + 1}, \quad (2.18)$$

where  $\text{Li}_n$  stands for the polylogarithm and  $\Gamma$  denotes the gamma function<sup>3</sup>. From a series expansion of  $f_n(z)$  one can verify the recursion relation  $\partial f_n(z) / \partial z = f_{n-1}(z) / z$  and therefore equation (2.6) evaluates to

---

<sup>3</sup>The polylogarithm is implemented in *Mathematica* as  $\text{Li}_n(t) = \text{PolyLog}[n, t]$  and the gamma function as  $\Gamma(t) = \text{Gamma}[t]$ .

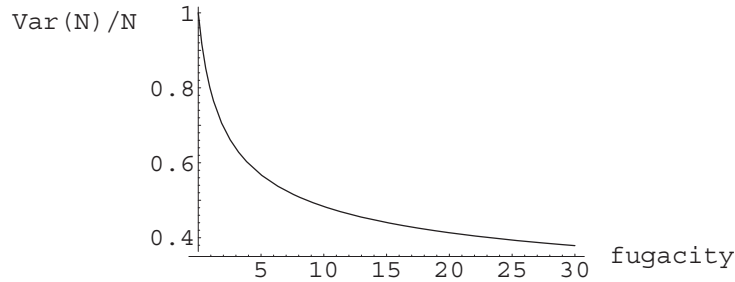


Figure 2-1: Suppression of density fluctuations in a quantum degenerate ideal Fermi gas. The relative fluctuations  $(\Delta N)^2/N = f_{1/2}(z)/f_{3/2}(z)$  are shown as a function of the fugacity  $z = e^{\beta\mu}$ . For non-degenerate temperatures with  $z \rightarrow 0$  one retrieves classical Poissonian statistics  $(\Delta N)^2 = N$ .

$$\sigma_N^2 = \frac{1}{\beta} \beta z \frac{\partial N}{\partial z} = V/\lambda^3 f_{1/2}(z). \quad (2.19)$$

Fig. 2-1 illustrates this result by plotting the ratio  $\sigma_N^2/N$  versus the fugacity  $z$ .

Following equation (2.7) the calculated density fluctuations of the ideal Fermi gas correspond to an isothermal compressibility  $\kappa_T = (nk_B T)^{-1} f_{1/2}(z)/f_{3/2}(z)$ . At temperatures low compared to the Fermi temperature  $T_F = \epsilon_F/k_B$  this compressibility becomes  $\kappa = 3/(2n\epsilon_F)$  to first order in  $T/T_F$ . Vice versa the relative fluctuations then scale linearly like

$$\frac{\sigma_N^2}{N} = \frac{3}{2} \frac{k_B T}{\epsilon_F} \quad \text{for } T \rightarrow 0. \quad (2.20)$$

In contrast, the classical ideal gas with its compressibility  $\kappa_T = 1/(nk_B T)$  as obtained from equation (2.8) always maintains  $\sigma_N^2/N = 1$ .

### 2.3.2 Small probe volume limit

In the foregoing discussion it was assumed that the volume  $V = 4/3 \pi R^3$  was sufficiently large such that probe volume surface effects would be negligible and  $\sigma_N^2 \propto R^3$ . However, for  $\delta k R \ll 1$  (with  $\delta k$  as defined in the previous section) zero tempera-

ture quantum fluctuations following the law  $\sigma_N^2 \propto R^2 \ln R$  for  $R \rightarrow \infty$  become the dominant noise source.

To calculate  $\sigma_N^2$  in analogy to (2.8) for a polarized zero temperature non-interacting Fermi gas one has to evaluate the density-density static correlation function

$$C(\mathbf{r}) = \langle \rho(\mathbf{r}_1) \rho(\mathbf{r}_2) \rangle_C \quad \text{with} \quad \mathbf{r} = \mathbf{r}_1 - \mathbf{r}_2. \quad (2.21)$$

The calculation is simplified by first considering the problem in momentum space. The corresponding quantity  $S_{\mathbf{q}} = \int d^3\mathbf{r} e^{-i\mathbf{q}\cdot\mathbf{r}} C(\mathbf{r})$  is known in scattering theory as static structure factor [26, 31] and quantifies the scattering rate of a probe particle as a function of the momentum transfer  $\mathbf{q}$ . For a Fermi sea one can directly write

$$S_{\mathbf{q}} = \frac{1}{V} \sum_{\mathbf{k}} n_{\mathbf{k}} (1 - n_{\mathbf{k}+\mathbf{q}}), \quad (2.22)$$

i.e. the probability to scatter a Fermion from momentum state  $\mathbf{k}$  into momentum state  $\mathbf{k} + \mathbf{q}$  is proportional to the product of the occupation number  $n_{\mathbf{k}}$  of the initial state and the probability  $1 - n_{\mathbf{k}+\mathbf{q}}$ , that the final momentum state  $\mathbf{k} + \mathbf{q}$  is empty.

With the explicit knowledge of  $S_{\mathbf{q}}$ , the correlation function is now obtained by Fourier transforming (2.22) back to coordinate space which gives

$$C(\mathbf{r}) = \int \frac{d^3\mathbf{q}}{(2\pi)^3} S_{\mathbf{q}} e^{i\mathbf{q}\cdot\mathbf{r}} = n \delta(\mathbf{r}) - \left| \frac{1}{V} \sum_{\mathbf{k}} n_{\mathbf{k}} e^{i\mathbf{k}\cdot\mathbf{r}} \right|^2. \quad (2.23)$$

The summation over all momentum states can be rewritten as a known integral and eventually one finds for  $T \rightarrow 0$

$$C(\mathbf{r}) = n \delta(\mathbf{r}) - \frac{9n^2}{(k_F r)^4} \left( \frac{\sin k_F r}{k_F r} - \cos k_F r \right)^2 \quad (2.24)$$

with the Fermi wave vector  $k_F = (6\pi^2 n)^{1/3}$ . It is worth noting that this correlation

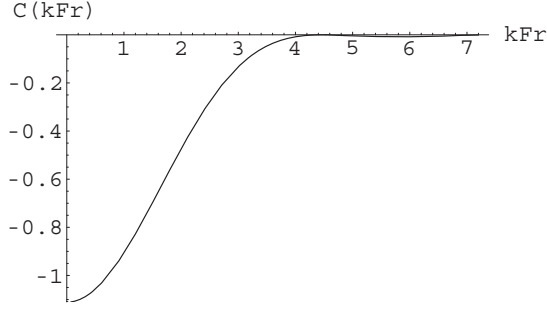


Figure 2-2: Density-density correlation function for a zero temperature non-interacting Fermi gas.  $C(\mathbf{r})$  is measured in arbitrary units and plotted as a function of  $k_F r$ . Due to Pauli exclusion one finds a correlation hole of approximate width  $k_F^{-1}$  near the origin.

function - depicted in Fig. 2-2 - follows a power-law decay, i.e. as expected for a gapless system there is no characteristic correlation length.

From (2.24) the zero temperature number fluctuations inside a spherical probe volume of radius  $R$  are obtained as  $(\Delta N)^2 = \int_V \int_V d^3\mathbf{r}_1 d^3\mathbf{r}_2 C(|\mathbf{r}_1 - \mathbf{r}_2|)$  and since  $C$  depends only on  $r = |\mathbf{r}_1 - \mathbf{r}_2|$ , the double integration can be replaced with a one-dimensional integral leading to

$$(\Delta N)^2 = \int_V \int_V \int_V d^3\mathbf{r}_1 d^3\mathbf{r}_2 \delta(\mathbf{r}_1 - \mathbf{r}_2 - \mathbf{r}) C(r) d\mathbf{r} = \int_0^{2R} dr 4\pi r^2 \Omega(r) C(r) \quad (2.25)$$

with the geometrical overlap function  $\Omega(r) = \pi/12 (4R+r)(2R-r)^2$ . The integration can be performed exactly in terms of complex integral functions [32, 31] and for  $k_F R > 1$  one asymptotically finds

$$(\Delta N)^2 = \frac{(k_F R)^2}{2\pi^2} \ln(A k_F R) - \frac{1}{24\pi^2} \ln(B k_F R) + \mathcal{O}\left(\frac{1}{k_F R}\right) \quad (2.26)$$

with the constants  $A = 4e^{\gamma-1/2}$  and  $B = 4e^{\gamma-5/12}$  and  $\gamma = 0.577\dots$  being Euler's constant. This confirms that zero temperature quantum fluctuations in an ideal

Fermi gas scale with  $N^{2/3} \ln(\text{const} \cdot N^{1/3})$ ; they can be interpreted as a surface term  $\propto R^2$  representing particle projection noise on the probe volume surface and their contribution compared to Pauli suppressed thermal fluctuations proportional to  $N$  becomes particularly relevant for small probe volumes.

## 2.4 Fluctuations in an interacting Fermi gas

The discussion so far focused on density fluctuations in a cold spin-polarized ideal Fermi gas. A two-component system of interacting Fermions gives rise to new phenomena and exhibits qualitatively different noise properties. By measuring fluctuations in linear combinations of the two pseudospin component densities  $n_1$  and  $n_2$  one can access quantities like  $\Delta(n_1 + n_2)$  or  $\Delta(n_1 - n_2)$  that are directly linked to the compressibility or spin susceptibility of the gas.

First consider the case of weak interactions with  $|k_F a| < 1$ . The parameter  $k_F a$ , where  $a$  denotes the s-wave scattering length, characterizes the ultra-low energy atom-atom interaction between the two spin states. In the 1950s L. D. Landau developed a theoretical approach that connects the ideal Fermi gas via the concept of *quasi-particles* to an interacting Fermi liquid. Landau's Fermi liquid theory [33] makes it possible to derive perturbative expressions that relate the isothermal compressibility  $\kappa$  and spin susceptibility  $\chi$  of a weakly interacting Fermi gas to those of an ideal zero temperature Fermi gas, i.e.  $\kappa_0 = 3/2n\epsilon_F$  and  $\chi_0 = 3n/2\epsilon_F$ . At this point no derivation is presented but for later reference the results are provided. Following [33, 34, 35] one finds

$$\kappa_0/\kappa = (1 + F_0^s)m/m^* \quad \text{and} \quad \chi_0/\chi = (1 + F_0^a)m/m^* \quad (2.27)$$

with the effective mass  $m^* = m(1 + F_1^s/3)$  and the  $l$ th angular momentum symmetric and antisymmetric Landau parameters (to second order in  $k_F a$ )

$$F_0^s = \frac{2}{\pi}k_F a + \frac{8}{3\pi^2}(2 + \ln 2)(k_F a)^2 \quad \text{and} \quad F_1^s = \frac{8}{5\pi^2}(7 \ln 2 - 1)(k_F a)^2 \quad (2.28)$$

and

$$F_0^a = -\frac{2}{\pi}k_F a - \frac{8}{3\pi^2}(1 - \ln 2)(k_F a)^2 \quad \text{and} \quad F_1^a = -\frac{8}{5\pi^2}(2 + \ln 2)(k_F a)^2. \quad (2.29)$$

Employing the Landau parameters one can in analogy find an extended version of equation (2.26) describing how quantum fluctuations are affected by interactions between the two spin components of the gas [35].

Explicitly calculating the previous expressions for  $\kappa$  and  $\chi$  confirms the intuitive expectation that the compressibility increases for attractive interactions and decreases for repulsive interactions, whereas the spin susceptibility becomes smaller with attractive interactions and increases for repulsive interactions.

In addition to the effects of weak interactions discussed so far, an ultracold interacting Fermi gas will demonstrate BEC-BCS crossover physics [36] when tuning the interactions (via a Feshbach resonance) through the strongly interacting region with  $|k_F a| > 1$ . This implies a very different behavior of the gas on the BCS and on the BEC side. While the many-body BCS state is characterized by pair associations in momentum space, the BEC side corresponds to the Bose-Einstein condensation of bound dimers. Being composed of two atoms of opposite spins, these dimers (molecules) strongly affect the noise properties of the gas and lead, for instance, to a suppression of  $\Delta(n_1 - n_2)$  fluctuations on length scales larger than the molecule size.

## 2.5 Density fluctuations and light scattering

To measure number fluctuations all experiments presented in this thesis employ light scattering for the localization and counting of atoms within a certain probe volume. Therefore it is appropriate to further emphasize some of the underlying physical principles that describe the probing of a cloud of atoms with a coherent light field.

Consider first the very general scenario of a scattering experiment, where a collimated beam of probe particles (e.g. electrons, neutrons, photons...) is directed onto a target system (e.g. a crystal, a cloud of atoms...) and the interaction-induced deflection of the probe particles is measured. In such a case the interaction potential can be written as<sup>4</sup>

$$V_{\text{int}} = \sum_i V(\mathbf{r}_i - \mathbf{R}), \quad (2.30)$$

where  $\mathbf{R}$  denotes the position of the probe particle and the  $\mathbf{r}_i$  are the positions of the target system particles. By Fourier transforming this potential one obtains

$$V_{\text{int}} = \sum_i \sum_{\mathbf{q}} V_{\mathbf{q}} e^{i\mathbf{q}\cdot(\mathbf{r}_i - \mathbf{R})} = \sum_{\mathbf{q}} V_{\mathbf{q}} \rho_{\mathbf{q}}^* e^{-i\mathbf{q}\cdot\mathbf{R}} \quad (2.31)$$

with  $\rho_{\mathbf{q}} = \sum_i \int d^3r \delta(\mathbf{r} - \mathbf{r}_i) e^{-i\mathbf{q}\cdot\mathbf{r}}$  being the Fourier transform of the particle density. Assuming weak coupling the probe beam is described as a plane wave with initial wave vector  $\mathbf{P}$  and final wave vector  $\mathbf{P} - \mathbf{q}$ , the target system is initially in its ground state  $|i\rangle$  and after the scattering event in the excited state  $|f\rangle$  with momentum  $\mathbf{q}$ . Therefore the transition matrix element becomes

$$\langle f, \mathbf{P} - \mathbf{q} | V_{\text{int}} | i, \mathbf{P} \rangle = V_{\mathbf{q}} \langle f | \rho_{\mathbf{q}}^* | i \rangle, \quad (2.32)$$

---

<sup>4</sup>The interaction potential is assumed to not depend on the relative velocity of the particles. For a more detailed discussion see [34].

i.e. a scattering act with momentum transfer  $\mathbf{q}$  requires a density modulation at that wave vector.

This connection, which is just rephrasing the basic concept of Fourier optics, can be illustrated by a simple example: Consider a confined gas of  $N$  atoms irradiated by a coherent light source. Each atom will act as an externally driven oscillator and contribute to the far field distribution at a given observation point  $\mathbf{R}_0$ . One can now divide the atoms into two groups, those that contribute a field of positive phase factor and those that contribute a field of negative phase factor. With  $N_{\text{pos}}$  atoms in the first group and  $N_{\text{neg}} = N - N_{\text{pos}}$  belonging to the second group, the scattered intensity into the direction of  $\mathbf{R}_0$  becomes  $I = I_0 (N_{\text{pos}} - N_{\text{neg}})^2$  with  $I_0$  being the scattered intensity for a single atom. Assuming a random distribution of the atoms among the two groups (binomial with equal probability) one expects  $(\Delta N_{\text{pos}})^2 = N/4$  and therefore

$$\langle I \rangle = I_0 \langle (N_{\text{pos}} - N_{\text{neg}})^2 \rangle = I_0 \langle (2N_{\text{pos}} - N)^2 \rangle = I_0 N, \quad (2.33)$$

i.e. the scattering intensity is simply proportional to  $N$ . Furthermore, equation (2.33) confirms that no scattering can occur for a uniform distribution of atoms: Destructive interference cancels the scattered field everywhere except in the forward direction.

Overall this discussion of light scattering completes the main purpose of this theory overview, the presentation of the triad of scattering properties, fluctuations and linear response of a thermodynamic system. The results obtained for the case of a degenerate Fermi gas are the foundation for the analysis of the experimental findings described in the following chapters.

## Chapter 3

# Measuring fluctuations in an ideal Fermi gas

*This chapter focuses on the experiment reported in the following publication: C. Sanner, E. J. Su, A. Keshet, R. Gommers, Y. Shin, W. Huang, and W. Ketterle, “Suppression of Density Fluctuations in a Quantum Degenerate Fermi Gas”. Included in Appendix A.*

Precisely measuring fluctuations in the density distribution of a cloud of ultracold atoms poses several experimental challenges. When introducing a new measurement method it is therefore advisable to first demonstrate it with a well-understood physical system. The experiment described in this chapter follows this strategy by repeatedly producing expanded clouds of a non-interacting Fermi gas and then counting the number of atoms in a small probe volume within the extended cloud. Subsequent statistical analysis of the counting results is expected to reveal Pauli suppression of fluctuations.

### 3.1 Measurements in trap and after ballistic expansion

With the theoretical infrastructure developed in the previous chapter it is straightforward to adapt the results obtained for homogeneous systems to the case of harmonically confined<sup>1</sup> gas clouds by employing the local density approximation (LDA) [32]. For sufficiently smooth confinement potentials  $U(\mathbf{r})$  that vary only weakly over the correlation length of the homogeneous gas, the gas cloud is decomposed into smaller subpieces with the same properties as the homogeneous gas of identical temperature and with local chemical potential  $\mu_{\text{local}} = \mu - U(\mathbf{r})$ .

In the case of ballistic expansion, the adaption is not as readily obtained. Consider for instance an ideal Fermi gas confined by a box potential to a cube of volume  $L^3$ . Upon release from this trap the gas will expand isotropically (reflecting the isotropic momentum distribution of the Fermi gas even if the trapping potential is deformed) and after long<sup>2</sup> times of flight  $t$  the density distribution represents the initial momentum distribution. More quantitatively, the via LDA obtained semiclassical [37] Fermi distribution function

$$f_0(\mathbf{r}, \mathbf{p}) = \frac{1}{e^{\beta(p^2/2m + U(\mathbf{r}) - \mu)} + 1} \quad (3.1)$$

is mapped to the expanded cloud following the ballistic law

$$f(\mathbf{r}, \mathbf{p}, t) = f_0(\mathbf{r} - \mathbf{p}t/m, \mathbf{p}). \quad (3.2)$$

For the homogeneous Fermi gas expanding out of the box potential this corresponds to an effective truncation of the original momentum distribution when observing the gas (for simplicity) around the former center of the trap at  $\mathbf{r} = 0$ ; the atom noise is mostly

---

<sup>1</sup>To a good approximation, an optical dipole trap provides harmonic confinement around its trap center.

<sup>2</sup>such that the size of the expanded cloud is large compared to  $L$

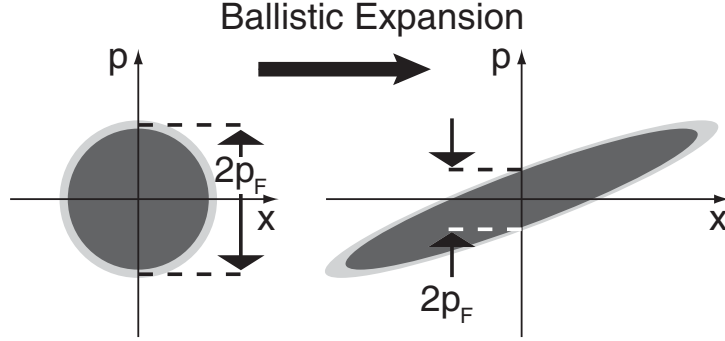


Figure 3-1: One-dimensional phase space diagram of ballistic expansion of a harmonically trapped ideal Fermi gas. Ballistic expansion shears the initially occupied spherical area into an ellipse. In the center of the cloud, the local Fermi momentum and the sharpness of the Fermi distribution are scaled by the same factor, keeping the ratio of local temperature to Fermi energy constant. The same is true for all points in the expanded cloud relative to their corresponding unscaled in-trap points.

”localized” at the higher momentum states close to the Fermi surface and during time of flight the corresponding particles will fly further apart. In other words, while no information is lost when globally analyzing the gas, the expansion will generally alter the local noise properties leading to noise distributions that cannot simply be mapped point to point between the initial and expanded gas cloud.

However, for the special case of an harmonic confinement with  $U(x) = \frac{m}{2} \omega^2 x^2$  and equivalent momentum and coordinate space wave functions, a simple mapping is possible. Figure 3-1 tries to illustrate this by comparing schematic 1D plots of the distribution function  $f(\mathbf{r}, \mathbf{p}, t)$  for times before and after some expansion. Still considering the distributions at  $\mathbf{r} = 0$  equations (3.1) and (3.2) show that the expansion converts

$$f(0, p, 0) = \frac{1}{e^{\frac{1}{k_B T} (\frac{p^2}{2m} - \mu)} + 1} \quad \text{into} \quad f(0, p, t) = \frac{1}{e^{\frac{1}{k_B \gamma T} (\frac{p^2}{2m} - \gamma \mu)} + 1} \quad (3.3)$$

with rescaling<sup>3</sup> factor  $\gamma = (1 + \omega^2 t^2)^{-1}$  and trap frequency  $\omega$ . Apparently, expansion out of an harmonic confinement is equivalent to a local rescaling of temperature  $T$  and

<sup>3</sup>Reference [38] provides a more rigorous treatment of the scaling formalism.

chemical potential  $\mu$  such that the fugacity  $z = e^{\mu/(k_B T)}$  stays constant. Therefore, it follows via equations (2.17) and (2.19) that in this case the relative noise properties of the gas are preserved.

## 3.2 The experimental procedure

To realize the laid out experimental agenda of repeatedly producing cold non-interacting Fermi gas clouds and then letting them expand to perform spatially resolved atom counting, it is necessary to employ a reliable Fermi gas apparatus and develop an appropriate sample preparation scheme. For details about the experimental infrastructure confer [39, 40]. Here the basic setup is only quickly sketched, detailed explanations and extensive discussions can be found in the aforementioned references and references therein.

### 3.2.1 Fermi gas apparatus

All experiments described in this thesis were carried out on MIT's second generation *BEC2* cold neutral atom machine. The apparatus was originally devised to produce degenerate bosonic gases of  $^{23}\text{Na}$  but was later upgraded to a double-species machine also producing fermionic  $^6\text{Li}$  samples. Being designed around a Ioffe-Pritchard type magnetic trap with slightly modified coil geometry to facilitate improved optical access, the system is comprised of a hot atoms source (vapor pressure oven with separate alkali reservoirs), a Zeeman slower and a central UHV glass cell. Laser setups for the sodium (1178 nm Yb fiber laser with Raman amplifier and frequency doubler) and lithium (671 nm diode laser) wavelengths generate the light necessary to magneto-optically trap (MOT) and cool the atoms. An additional 1064 nm 20 W fiber laser makes it possible to create far-off-resonance optical dipole traps (ODTs) to further manipulate the atom samples. All laser light is delivered to the main optical table via single-mode fiber cables. The various components of the apparatus are controlled and synchronized by a computer system with intuitive software user interface. A typical experimental run cycle from starting the MOT loading to releasing a quantum

degenerate Fermi gas out of the ODT takes between 30 to 40 seconds.

### 3.2.2 Sample preparation

In the following a short overview in table form of the Fermi gas sample preparation steps is provided. References [41, 40] contain further details.

1. Double-species effusive ovens create a hot collimated atomic beam.
2. A Zeeman slower decelerates the atoms.
3. Overlapping MOTs for Na and Li are being loaded from the slowed atomic beam.
4. The MOTs are switched off and the Na and Li atoms are optically pumped into the magnetically trappable stretched states  $|F = 2, m_F = 2\rangle$ , and  $|3/2, 3/2\rangle$  respectively.
5. The atoms are loaded into a magnetic trap with high bias field such that the different states can be resolved in microwave spectroscopy.
6. Appropriate microwave sweeps are applied to recycle and clean up sodium atoms in the wrong states.
7. Sodium is evaporatively cooled employing the  $|2, 2\rangle \rightarrow |1, 1\rangle$  microwave transition near 1.77 GHz.
8. Towards the end of the evaporation the magnetic trap is adiabatically decompressed to lower the sodium density and avoid three-body losses.
9. After the sodium is completely evaporated, the sympathetically cooled lithium is transferred into a tightly focused ODT.
10. A RF Landau-Zener sweep around 228 MHz transfers the lithium atoms to the lowest lying  $|1/2, 1/2\rangle$  state.

11. The sample is exposed to a high magnetic field of about 300 G where the different  $m_i$  states within the  $m_j = -1/2$  triplet develop an almost  $B$  field independent split of  $\approx 100$  MHz.
12. Repeated RF sweeps are applied to create an equal spin mixture of the two lowest ground states  $|1\rangle = |m_j = -1/2, m_i = 1\rangle$  and  $|2\rangle = |m_j = -1/2, m_i = 0\rangle$ , corresponding to the low field states  $|F = 1/2, m_F = 1/2\rangle$  and  $|F = 1/2, m_F = -1/2\rangle$ .
13. The atoms are adiabatically transferred from the tight single ODT into a crossed dipole trap created by two orthogonally overlapped single ODTs.
14. Forced evaporation induced by lowering the ODT trap depth cools the sample further down. Subsequently the gas cloud is recompressed.
15. The magnetic bias field is adjusted to around 527 G, where a magnetically tunable Feshbach resonance causes a zero crossing of the scattering length, creating a two-component ideal Fermi gas.
16. Finally the ODTs are extinguished and after 7 ms of ballistic expansion an absorption image resonant with state  $|2\rangle$  is acquired.

By changing the evaporation trap depth this procedure is adjusted to produce cold  ${}^6\text{Li}$  gas clouds containing  $N = 2.5 \times 10^6$  atoms per spin state with  $T = 0.2 T_F$ . The final round crossed dipole trap has radial and axial trap frequencies of  $\omega_r = 2\pi \times 160 \text{ s}^{-1}$  and  $\omega_z = 2\pi \times 230 \text{ s}^{-1}$  corresponding to an in-trap Fermi energy of  $E_F = (6N)^{1/3} \hbar\omega_{\text{ho}} = k_B \times 2.15 \mu\text{K}$ , with  $\omega_{\text{ho}} = (\omega_r^2\omega_z)^{1/3}$  being the geometrical average of the three trapping frequencies.

### 3.3 How to count atoms in a box - Experimental challenges and constraints

The above experimental procedure facilitates the reliable production of non-interacting Fermi gas clouds that can now become subject to a spatially resolved atom counting. Taking a quantitative photographic image of the cloud is the standard way to realize this goal.

#### 3.3.1 Different imaging methods

Various imaging methods have been adapted to the case of cold atoms. They can typically be divided into three classes, i.e. absorption imaging, fluorescence imaging and dispersive<sup>4</sup> imaging, and they all rely on the interaction of the atoms with resonant or near-resonant light. While absorption and dispersive imaging detect the light transmitted through the sample (small angle scattering assuming that the atoms are illuminated with a collimated laser beam), fluorescence imaging collects the light scattered off axis, often observing orthogonally to the probe laser beam. The underlying atom - light interaction process is quantum mechanically well understood [42] and the selection of a particular method for a certain experimental scenario is based on achieving an optimum signal-to-noise ratio. For expanded quantum gas clouds resonant absorption imaging is normally the method of choice. This is due to its technical simplicity and the fact that appropriate densities can be conveniently adjusted by changing the time of flight.

In a semiclassical picture [43] the atoms exposed to near-resonant light are described as charged oscillators under the influence of an incident electric drive field. The corresponding equation of motion relates the induced polarization  $\mathbf{P} = \epsilon_0(\epsilon - 1)\mathbf{E}$  to the external drive field  $\mathbf{E}$  so that one finds for the relative<sup>5</sup> dielectric constant

---

<sup>4</sup>Dispersive imaging measures the phase shift light is experiencing when passing through an optically thicker or thinner medium. The imaging system is set up so that the phase shift is converted into an intensity variation. Confer chapter 4 for a detailed analysis of dispersive imaging.

<sup>5</sup>relative to the vacuum permittivity  $\epsilon_0 = 8.85 \times 10^{-12} \text{ Fm}^{-1}$

$$\epsilon = n_{\text{ref}}^2 \quad \text{with} \quad n_{\text{ref}} = 1 + \frac{\sigma_0 n \lambda}{4\pi} \left( \frac{i}{1 + \delta^2} - \frac{\delta}{1 + \delta^2} \right) \quad (3.4)$$

being the complex index of refraction.  $\sigma_0 = 3\lambda^2/(2\pi)$  denotes the resonant light scattering cross section [42],  $\lambda$  the wavelength,  $n$  the atom density and  $\delta = \frac{\omega - \omega_0}{\Gamma/2}$  is the detuning in half linewidths. When traveling through the atom sample the probe light wave vector  $k_0$  is accordingly modified to  $k = k_0 n_{\text{ref}}$ , which means for a plane wave  $E_0^{i(k_0 z - \omega t)}$  an intensity attenuation (imaginary part of  $n_{\text{ref}}$ ) by a factor

$$T = \exp\left(-\sigma_0 n_{2\text{D}} \frac{1}{1 + \delta^2}\right) \quad (3.5)$$

and a phase shift (real part of  $n_{\text{ref}}$ ) of

$$\Delta\phi = -\frac{\sigma_0 n_{2\text{D}}}{2} \frac{\delta}{1 + \delta^2}, \quad (3.6)$$

where  $n_{2\text{D}} = \int n dz$  denotes the density integrated along the propagation direction (column density). It is important to note that the last equations rely on several assumptions (two-level system, intensities well below the saturation intensity, thin lens approximation etc.) implying various constraints that will be discussed later on.

All the above mentioned imaging methods try to reconstruct  $n_{2\text{D}}$  from direct or indirect measurements of transmission  $T$  or phase shift  $\Delta\phi$ . Absorption imaging straightforwardly measures  $T$  (therefore it is also called transmission imaging) by comparing on a linear CCD detector the probe light intensity distribution with and without atoms present. The quantity observed in fluorescence imaging can be mapped to  $1 - T$  since the "missing" light that was removed from the probe beam is now detected and dispersive imaging obtains a signal that relates to  $\Delta\phi$ .

The typical column density of an expanded gas cloud prepared according to the aforementioned procedure is  $n_{2\text{D}} \approx 5 \times 10^{12} \text{ m}^{-2}$  leading to an on-resonance ( $\delta = 0$ ) optical density of  $OD_e = -\ln T \approx 1$ . This amount of transmission is ideally suited

for direct CCD camera measurements since it delivers a large signal without exceeding the dynamic range of the measurement, i.e. each atom contributes with its full scattering cross section and the images are not blacked out. In principle one can more systematically calculate and compare the obtainable  $S/N$  values for the various imaging configurations but particularly in the context of atom noise measurements such an approach can potentially be misleading given that imperfections and a multitude of other noise sources and systematic nonlinear effects dominate when defining the useful parameter space for a certain imaging method.

### 3.3.2 Atom noise and other noise sources

Every measurement process is accompanied by noise. When a certain type of noise itself is in the focus of the measurement, one has to distinguish between wanted and unwanted noise. Clearly, in the case of atom noise detection via resonant absorption imaging, photon shot noise can be a significant noise competitor.

#### Image acquisition with a CCD camera

Consider the typical experimental scenario of a CCD detector that measures via a two-dimensional array of small<sup>6</sup> light sensitive pixels the spatial intensity distribution of an incoming light beam. An optical imaging system between the illuminated atoms and the detector maps the intensity distribution directly behind the atoms to an often magnified image on the CCD. The digital image signal read out from the camera after the exposure is the basis for a subsequent noise analysis. Each pixel of a  $n$ -bit camera produces an integer output reading  $S$  between 0 and  $2^n - 1$  ADU (analog-digital units), linearly scaling with the amount of accumulated electrons<sup>7</sup> in that pixel. Depending on the internal conversion gain  $c$  of the detector,  $x$  accumulated electrons lead to an output signal  $S = cx$ . Scientific CCD camera systems offer adjustable readout gains with high gain settings up to one ADU per electron.

---

<sup>6</sup>The typical square pixel size of modern CCD cameras ranges between 5 and 20  $\mu\text{m}$ .

<sup>7</sup>A photon hitting a CCD pixel causes on average the release of  $\eta$  electrons.  $\eta$  is the quantum efficiency of the detector.

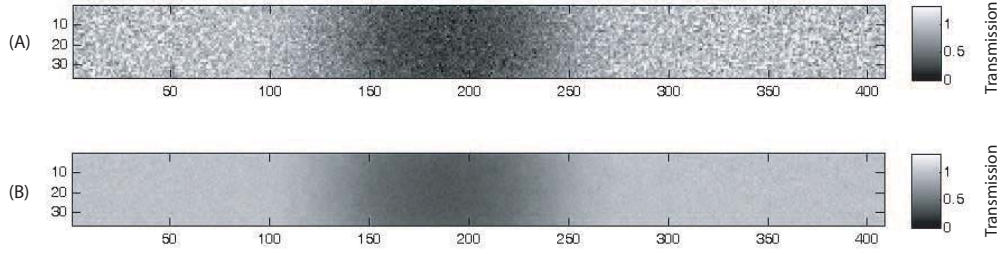


Figure 3-2: Transmission images of an expanded Fermi gas cloud. Image (A) was acquired employing a low intensity probe beam, while image (B) was obtained using a probe beam of higher intensity. Both images contain the same (vertically truncated) envelop density profile information, but the low intensity image (A) is visibly more noisy in the regions away from the atom cloud due to increased relative photon shot noise. The numbers on the horizontal and vertical axes are pixel counting coordinates.

### Photon shot noise

If a photon counting detector is exposed to a classical light source like coherent laser light and receives on average  $\langle P \rangle$  photons (e.g. for a certain exposure time at constant intensity), the probability  $p(P)$  to detect  $P$  photons in another run of the same experiment has to follow a Poisson distribution [43]

$$p(P) = \frac{\langle P \rangle^P e^{-\langle P \rangle}}{P!}. \quad (3.7)$$

This distribution with its standard deviation  $\Delta P = \sqrt{\langle P \rangle}$  leads to considerable amounts of relative noise  $\Delta P / \langle P \rangle = 1 / \sqrt{\langle P \rangle}$  for small  $\langle P \rangle$ . Figure 3-2 illustrates this by comparing two transmission images of a similar atom cloud, one obtained with low intensity probe light and the other one obtained with higher intensity illumination. Noise measurements are normally performed in a "vertical" fashion, i.e. by analyzing the fluctuations of the same pixel along many repeated images, but for the purpose of demonstrating the role of photon shot noise it is equivalent to do a "horizontal" analysis within one image and obtain a visual impression by comparing many neighboring pixels. It is important to realize that photon shot noise is observed in the spatial domain and in the time domain.

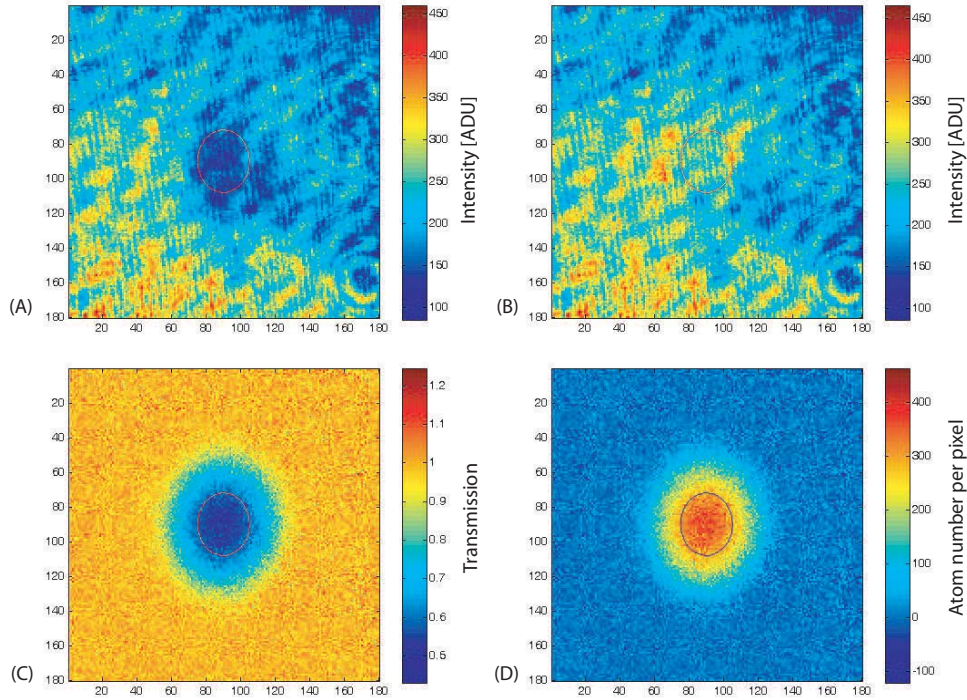


Figure 3-3: A transmission image of an expanded  ${}^6\text{Li}$  Fermi gas cloud is obtained by normalizing the intensity distribution of an offset-corrected  $PWA - DF$  image (A) with respect to an  $PWOA - DF$  image (B). Even though the illumination is very non-uniform and full of fringes, the resulting transmission image (C) is clean and does not exhibit any visible fringe structure. To ensure a linear response, the atoms were exposed to low-intensity (low compared to the saturation intensity) probe light for a very short interval, so that on average every atom scattered only one photon. From the transmission, the corresponding atom number per pixel column is derived via equation (3.5) and displayed in image (D). Elliptical contour lines help to localize corresponding points in the images. The field of view is  $2\text{ mm} \times 2\text{ mm}$ .

### The transmission image

As discussed earlier in this chapter a transmission image is generated by acquiring several raw images, i.e. 2D integer arrays, from the camera. The first image, the picture with atoms ( $PWA$ ), is taken by exposing the atoms to a short (few microseconds to tens of microseconds exposure time) well defined resonant probe light pulse and looking with the camera on-axis through an appropriate imaging system onto the atom sample. The image records the probe light intensity distribution as locally

modified by absorbing atoms. A second image, the picture without atoms (*PWOA*), is taken for normalization purposes under identical conditions but without atoms. Ideally the wait time between the two exposures is rather short so that unavoidable drifts in the experimental setup are common-mode to these two images. Finally a third image, the dark frame (*DF*), is obtained by triggering an exposure sequence without probe light present. This makes it possible to correct the other two images for shot-to-shot reproducible background offsets. Overall the transmission image (*TI*) is now derived as  $TI = (PWA - DF)/(PWOA - DF)$ . It is the natural starting point for all further image analysis; interpreting the transmission image is significantly easier compared to directly observing the *PWA* image because all residual structures and imperfections in the coherent illumination beam (as long as they are unchanged between *PWA* and *PWOA* like fringes from back reflections, dust particles etc.) are canceled out by the normalization process. Figure 3-3 demonstrates this impressively.

### Photon shot noise propagation

For a proper noise analysis it is necessary to decompose the noise observed in the processed images back into the basic noise components found in the raw images. The offset-corrected average signal read from a single pixel can be written as  $\langle S \rangle = \eta \langle P \rangle c$  with the already introduced average photon number  $\langle P \rangle$ , the detection quantum efficiency  $\eta$  and the conversion gain  $c$ . Applying Poisson statistics for a classical light source one therefore expects  $\Delta S = c \sqrt{\eta \langle P \rangle}$  with the deterministic scaling gain  $c$  before the square root and the stochastic attenuation factor  $\eta$  under the square root. This leads to

$$\Delta S = \sqrt{\langle S \rangle} c \quad (3.8)$$

and makes it possible to calculate via error propagation the photon shot noise observed in a transmission image. Starting from an offset-corrected image pair  $S_1 = PWA - DF$  and  $S_2 = PWOA - DF$  with transmission image  $TI = S_1/S_2$  in a region with

average transmission  $t = \langle S_1 \rangle / \langle S_2 \rangle$  yields for the variance

$$(\Delta_{\text{ph}} TI)^2 = \left(\frac{1}{\langle S_2 \rangle} \Delta S_1\right)^2 + \left(-\frac{\langle S_1 \rangle}{\langle S_2 \rangle^2} \Delta S_2\right)^2 \quad (3.9)$$

$$= \left(\frac{1}{\langle S_2 \rangle} \sqrt{t} \Delta S_2\right)^2 + \left(\frac{t}{\langle S_2 \rangle} \Delta S_2\right)^2 \quad (3.10)$$

$$= \frac{t c}{\langle S_2 \rangle} + \frac{t^2 c}{\langle S_2 \rangle}. \quad (3.11)$$

For  $t = 1$  (i.e. no absorption) the last result simplifies to  $\Delta_{\text{ph}} TI = \sqrt{2c/\langle S_2 \rangle}$ , which quantitatively confirms the observations from Figure 3-2.

While the transmission image is the first step in the image processing chain, it has the shortcoming of providing a multiplicative signal that is not proportionally scaling with the atom count in the corresponding pixel column. This is easily fixed by taking the logarithm (Lambert-Beer law) and obtaining the additive optical density image  $OD = -\ln(TI)$ . For resonant absorption imaging, the optical density equals the product of resonant scattering cross section  $\sigma_0$  and column density  $n_{2D}$ , in accordance with equation (3.5). Analogously to (3.9) one finds for the photon shot noise variance in  $OD = -\ln(S_1/S_2)$  images

$$(\Delta_{\text{ph}} OD)^2 = \left(-\frac{1}{\langle S_1 \rangle} \Delta S_1\right)^2 + \left(\frac{1}{\langle S_2 \rangle} \Delta S_2\right)^2 \quad (3.12)$$

$$= \left(\frac{1}{\langle S_2 \rangle e^{-d}} \{\Delta S_2 \sqrt{e^{-d}}\}\right)^2 + \left(\frac{1}{\langle S_2 \rangle} \{\Delta S_2\}\right)^2 \quad (3.13)$$

$$= \frac{c}{\langle S_2 \rangle} (1 + e^d) \quad (3.14)$$

in regions with average<sup>8</sup> optical density  $d = -\ln t$ .

The calculations following equations (3.9) and (3.12) indirectly assumed that the

---

<sup>8</sup>Note that  $-\ln(\langle S_1 \rangle / \langle S_2 \rangle) \neq \langle -\ln(S_1/S_2) \rangle$  even for  $\langle S_1 \rangle / \langle S_2 \rangle = 1$ . The exponential scaling skews the probability distribution.

*PWA* image and the *PWOA* image were acquired with the same exposure parameters (probe light intensity and duration), but it is worth noting that noise-wise this is not necessarily the optimum configuration. Obviously, increasing  $S_1$  and  $S_2$  reduces the photon shot noise induced uncertainty  $\Delta_{\text{ph}}OD$ , however, the discussion later on will show that to maintain a linear atomic response there are stringent limits for the maximum intensity and photon number interacting with the atoms. In order to reduce  $\Delta_{\text{ph}}OD$  it is therefore experimentally not viable to simply increase the *PWA* and *PWOA* probe signals in parallel. Nevertheless, while keeping a sufficiently low light level for *PWA* one can still increase the *PWOA* normalization probe and obtain a scaled image  $S_{02}$  with very low relative photon shot noise  $\Delta S_{02}/S_{02}$ . Mathematically rescaling  $S_{02}$  back to an  $S_1$ -equivalent  $S_2 = S_{02}/q$  results in an appropriate normalization image  $S_2$  with the low noise properties  $\Delta S_2/S_2 = (\Delta S_{02}/q) / (S_{02}/q)$  of the  $S_{02}$  image<sup>9</sup>. Effectively this pre-scaling procedure eliminates the second term in equation (3.12) and can therefore significantly improve the signal-to-noise ratio in standard absorption imaging. In practice however, the scaling factor  $q$  is not arbitrarily large but rather limited by detection linearity requirements and sometimes even a small  $q$  can introduce systematic artifacts, e.g. from enhanced indirect diffuse light leakage into the detector.

### Atom shot noise

The atom cloud does not only homogeneously attenuate the resonant probe light as assumed in the previous section; in addition the localization of atoms into the different pixel columns of geometrical cross section  $A$  reveals the actual quantity of interest, the atom shot noise. Considering a classical ideal gas one expects Poissonian atom number fluctuations, i.e. a pixel column with average optical density  $d$  and containing on average  $N = dA/\sigma_0$  atoms will exhibit fluctuations  $\Delta N = \sqrt{N}$ , corresponding to additional optical density noise

---

<sup>9</sup>In short, "mathematical" attenuation is noise-wise superior to physically adjusting the photon flux.

$$(\Delta_{\text{atom}}OD)^2 = d \frac{\sigma_0}{A}. \quad (3.15)$$

For the experimental detection of atom noise it is beneficial to optimize the ratio  $(\Delta_{\text{atom}}OD)^2 / (\Delta_{\text{ph}}OD)^2$  of wanted to unwanted noise. The relevant expression  $d/(1+e^d)$  has a maximum around  $d = 1.3$ , suggesting to preferably perform noise analysis with absorption images in regions with an average optical density of 1.3, corresponding to a transmission of about 30 percent.

### Technical noise

In addition to the noise sources discussed so far the image acquisition process is accompanied by technical noise generated in the CCD detector. Of the two major contributions, dark current noise<sup>10</sup> and readout noise, only the readout noise is relevant in the context of this thesis. Reading out the charge from the individual pixels of the CCD is a multi-step process. By applying appropriate gate voltages the charges are sequentially transported over the whole pixel array and arrive eventually at the readout register and amplifier. Every electronic amplification process is noisy and depending on input impedance and bandwidth (reciprocally scaling with the readout time) of the amplifier one expects a certain noise floor. The readout noise  $r$  in high quality CCD detectors is typically on the order of 5 electrons rms at low readout speeds and therefore rather small compared to the expected photon and atom shot noises.

The effects of the readout noise on the overall noise budget are readily modeled by adding (in quadrature) an uncorrelated offset noise per image to the photon shot noise expression as obtained in equation (3.12) et seq., which means that the terms in the curly brackets are augmented by  $\Delta_{\text{read}} = rc\sqrt{2}$ , so that  $\{\dots\}$  is replaced by  $\sqrt{\{\dots\}^2 + 2r^2c^2}$ . The factor 2 comes from the fact that the contributing images  $S_1$  and

---

<sup>10</sup>Even in complete darkness, a CCD detector slowly accumulates thermally generated electrons in its pixels. Cooling the CCD chip in modern camera systems reduces the dark current down to less than 0.02 electrons per pixel per second, causing negligible offsets and noise for short exposure times.

$S_2$  were obtained by subtracting a dark frame from the *PWA* and *PWOA* images. The *DF* image contributes an equal amount of readout noise.

### 3.3.3 Nonlinear effects and other limitations

So far the atom - light interaction was assumed to be a linear process. The measurement and noise analysis procedures discussed in the previous section heavily rely on this assumption. On the other hand, the obtained equations like (3.9) and (3.12) motivate higher light levels for better atom-noise to photon-noise ratios, potentially rendering linear approximations invalid.

#### Saturation of the atomic transition

Reconsidering the elementary light scattering process [44] where an atom absorbs a photon and re-emits it after an excited state lifetime  $\tau$ , corresponding to a natural spectral linewidth  $\Gamma = \tau^{-1}$  of the transition, it is clear that the scattering rate  $\gamma$  is linearly scaling with the incoming photon flux only if  $\gamma \ll 1/\tau$ . In terms of light intensity  $I$  one therefore finds the requirement  $I \ll I_s$  with the saturation intensity  $I_s = \hbar\omega\Gamma/(2\sigma_0)$  and beyond this the scattering rate is given by

$$\gamma = \frac{(I/I_s)(\Gamma/2)}{1 + I/I_s + \delta^2} \quad (3.16)$$

with frequency  $\omega$  and detuning  $\delta$  as defined at the beginning of this chapter. Typical values for the saturation intensity of alkali atoms are on the order of few mW/cm<sup>2</sup>, e.g.  $I_s = 2.5$  mW/cm<sup>2</sup> for <sup>6</sup>Li atoms on the D<sub>2</sub> line. The full equation (3.16) must lead to an intensity dependent index of refraction; only in the limit  $I \ll I_s$  the denominator in the scattering rate expression approximately equals 1 so that the differential intensity decrement  $dI$  of a weak probe beam traveling through the atom gas becomes simply proportional to  $I$ . In this case one recovers equations (3.5) and (3.6) such that the atomic column density can be obtained without knowledge of the absolute illumination intensity.

With nonlinear behavior due to saturation effects it becomes more troublesome to quantitatively interpret a transmission or optical density image. In principle it is straightforward to apply a saturation correction based on the intensity distribution as measured in the *PWOA* image, but unavoidable errors (e.g. from additional intensity variations and interference patterns caused by optical components after the atom cloud) can easily falsify the results. For a non-uniform probe beam this would lead to an effective "imprint" of probe beam intensity inhomogeneities into the atom distribution. Given that a free-space coherent laser beam passing through various optical elements will almost always accumulate fringes and other intensity textures on all length scales (see Figure 3-3 (A) and (B)), this imprint mechanism could severely affect the outcome of noise measurements, leading to an overestimation of atom noise. Furthermore, bleaching (i.e. oversaturating) the atomic transition is effectively equivalent to reducing the scattering cross section, which counterproductively reduces  $\Delta_{\text{atom}}OD$  as seen in equation (3.15).

### **Displacement blurring and recoil induced detuning**

From the discussion in the previous paragraph it might appear tempting to increase the detected photon number (and therefore reduce the photon shot noise) by increasing the duration instead of the intensity of the probe light pulse. However, this approach comes with two negative side effects.

First, every photon that is scattered by an atom transfers recoil momentum to it. Along the direction of the probe beam, an atom of mass  $m$  acquires a velocity  $v_{\text{fwd}} = v_{\text{rec}}N$  after having scattered  $N$  photons with wave vector  $k$ , each adding a recoil velocity of  $v_{\text{rec}} = \hbar k/m$  in the forward direction. The isotropic reemission of the photons causes another random walk velocity  $v_{\text{rnd}} = v_{\text{rec}}\sqrt{N}$  that leads to a transversal displacement of the atoms. For light  ${}^6\text{Li}$  atoms that scatter a few photons with  $v_{\text{rec}} = 0.1 \text{ m/s}$  one finds negligible displacements for short exposure times of a few microseconds, but many photons scattered over a longer time interval will eventually cause significant displacements affecting the noise analysis.

The second effect imposing a (more severe) limit onto the total number of scattered

photons is the recoil induced Doppler detuning. For resonant absorption imaging the probe light frequency is adjusted to be on resonance with atoms at rest. Being accelerated away from the light source, the light frequency  $\nu$  appears red-shifted by  $\Delta\nu$  in the atom's reference frame. Each on-axis recoil causes an additional Doppler shift  $\Delta\nu/\nu = v_{\text{rec}}/c$ , where  $c$  stands for the speed of light. For each scattered photon a  ${}^6\text{Li}$  atom accumulates a detuning of  $\Delta\nu = 150\text{ kHz}$ , i.e. after scattering only ten photons per atom, a  ${}^6\text{Li}$  ( $\Gamma_{6\text{Li}} = 2\pi \times 5.9\text{ MHz}$ ) sample's apparent optical density will be reduced to 80 percent of its on-resonance value. The implications for noise measurements are similar to those described in the paragraph about approaching the saturation intensity (e.g. imprinting of intensity irregularities), but for the detuning effect only the total number of scattered photons counts, regardless of the intensity.

One possible remedy for this effect is to intentionally blue-shift the imaging light frequency so that the effective detuning is symmetrically scanned over the resonance and not just sampling one wing of the Lorentzian resonance profile; similar to a synchronized frequency sweep during the imaging pulse one can thereby achieve a smaller pulse-averaged detuning. Practically one finds that while these methods do reduce the detuning-induced bleaching, they introduce additional experimental complications; overall it turns out that in the interest of a straight-forward image analysis and reproducible conditions it is more beneficial to employ low to moderate intensities and reduced photon numbers than to obtain better photon noise statistics at the price of nonlinear complications.

### **Optical pumping into dark states**

Another important aspect leading to nonlinear behavior is the multilevel structure of real atoms. Even when performing imaging via a nominal cycling transition (a resonance that is in terms of selection rules the only transition drivable by the applied light) there is a small probability to depump atoms into a dark state. Subsequently these atoms cannot scatter additional photons causing falsified transmission measurements at higher imaging intensities or longer exposure times (i.e. when each atom is expected to scatter on average several photons). To quantify this effect it is necessary

to carefully consider all external admixtures to the "ideal" two-level states. For example, in the case of the  ${}^6\text{Li}$  atom one can analytically derive [45] the composition of the six hyperfine ground states (see Figure 3-8) of the internal Hamiltonian in terms of the appropriate  $|m_s m_i\rangle$  basis with the projection of the electron and nuclear spin, e.g.

$$|1\rangle = \sin \theta_+ |1/2, 0\rangle - \cos \theta_+ |-1/2, 1\rangle, \quad (3.17)$$

where  $\theta_+$  is a magnetic field dependent parameter causing a cycling probability  $\cos^2 \theta_+ \approx 0.995$  for typical imaging fields around 500 G. While such theoretical estimates can provide initial insight, one typically finds that other experimental uncertainties (light polarization deviations etc.) do significantly affect the anticipated numerical values.

Eventually the optimum imaging pulse parameters were experimentally determined by preparing similar Fermi gas clouds and systematically varying intensities and exposure durations. Given that in the subsequent noise measurements pixel bin sizes down to a few microns were employed, the exposure time was conservatively set to 4  $\mu\text{s}$  in order to avoid any displacement blurring issues. Scanning the intensity while keeping this exposure duration revealed a dependence as depicted in Figure 3-4. Picking an intensity of about 10 percent of the saturation intensity turned out to be a good compromise between the onset of nonlinear effects and increasing levels of photon shot noise. The section on image data analysis will provide more details about the management of residual nonlinear effects.

### **Image normalization imperfections**

As previously discussed in the context of Figure 3-3, normalizing the  $S_1 = PWA - DF$  image by a  $S_2 = PWOA - DF$  image, i.e. pixel-wise dividing  $S_1$  by  $S_2$ , ensures the cancelation of illumination non-uniformities as long as detector response and atomic response are linear and as long as the non-uniform structures are static, i.e. unchanged

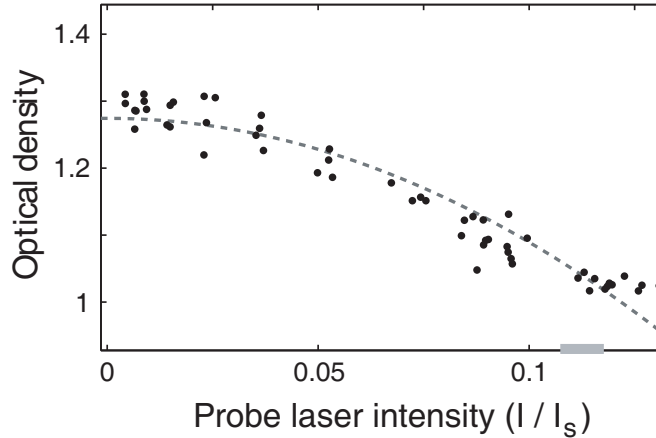


Figure 3-4: Apparent optical density of an expanded Fermi gas cloud as a function of probe light intensity for a fixed exposure time of  $4 \mu\text{s}$ . The observed optical density decreases with increasing probe light intensity. The line is a quadratic fit to the data. The reduction of the effective scattering cross section is mainly due to the Doppler effect caused by acceleration of the atoms by radiation pressure; a smaller reduction results from the partial saturation of the optical transition. At the probe light intensity chosen in this study (shaded bar), the number of photons absorbed per atoms is about 6. The decrease of the cross section is slightly larger than that predicted by simple models.

between the acquisition of  $S_1$  and  $S_2$ . The last requirement is not necessarily easy to meet; fringes and other structures responsible for the illumination inhomogeneities are typically the result of residual interferences and therefore extremely sensitive to vibrations and other disturbances in the imaging setup. Various strategies can help to minimize normalization imperfections - among them are passive means of stabilizing the imaging system, post-selection of images, dynamically smoothing the illumination profile and minimizing the time interval between the *PWA* and *PWOA* images. All of these methods will be discussed below in more detail.

### 3.4 The imaging system for noise measurements

With all the specific requirements for quantitative atom noise measurements the careful design of the imaging system is of particular importance. Relevant design aspects

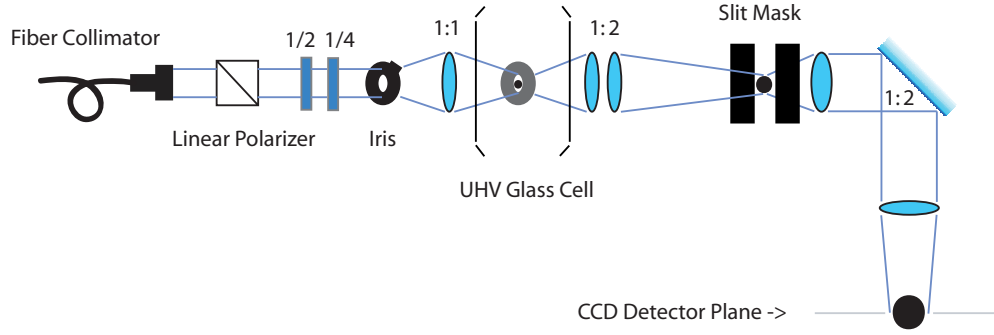


Figure 3-5: Imaging setup for noise measurements in expanded gas clouds. The atom cloud (black dot in the vacuum glass cell) is illuminated by appropriately polarized (circular polarization obtained with the 1/2 and 1/4 waveplates for magnetic bias fields along the propagation axis) imaging light projected through a narrow iris diaphragm. An intermediate image of the atoms is formed on an adjustable slit mask and via a second 1:2 magnification stage the final image of the atom cloud is focused onto the CCD camera.

and various improvement attempts to achieve appropriate performance are described in this section.

### 3.4.1 Overview of the imaging system

Optical imaging is a very universal scientific tool, widely used in many fields, and with advanced lens designs engineers have been able to fulfill the most demanding requirements. In many aspects, the criteria for an optimized noise measurement imaging system are different from standard optical performance benchmarks. Therefore, instead of providing an introduction to imaging theory<sup>11</sup>, the following discussion will mostly focus on noise-specific considerations.

Figure 3-5 provides a schematic of the imaging setup employed for noise measurements in expanded Fermi gases. The imaging light originates from an external cavity diode laser system that is frequency locked to an atomic reference. Before being sent via a polarization maintaining optical fiber to the main optical table, the light is

<sup>11</sup>For textbooks on optical imaging theory, see [46, 47] and references therein.

passed through an acousto-optic modulator and a mechanical shutter enabling fast intensity control and high extinction-ratio switching. On the other end of the optical fiber the light is recollimated to a beam with about 5 mm  $1/e^2$ -diameter by means of an integrated fiber collimation package. Next, the polarization is cleaned up with a polarizing beam splitter cube and subsequently adjusted to any desired state via a quarter- and a half-waveplate. By illuminating a small 2 mm aperture iris with this beam and imaging it 1:1 via a cemented achromat onto the atom cloud it is possible to obtain a relatively flat and sharply confined illumination background for the atoms. Spatially reducing the illumination to the actual region of interest helps minimizing potential back reflections and interference fringes. For the same reason it is also advisable to use as few as possible optics components, all with high quality narrow antireflection coatings.

In the next step a real 1:2 magnified image of the atom cloud is formed through a two-component lens telescope, comprised of a  $f = 150$  mm front achromat and a  $f = 300$  mm lens in the back. Positioned in the image plane is an adjustable slit aperture, such that the relay image with vertical black borders can eventually be re-imaged (again with 1:2 magnification) onto the camera, producing a final image on the CCD sensor, format-wise similar to those shown in Figure 3-2. The slit aperture in the intermediate image plane makes it possible to operate the CCD detector in "Fast Kinetics" mode, a special high-speed acquisition mode where only a small vertical subregion of the CCD chip can be exposed to light. The CCD's square pixels are 13  $\mu\text{m}$  wide and the chip surface is antireflection (AR) coated.

The last 1:2 imaging step is performed with a commercial Mitutoyo infinite conjugate microscope objective plus corresponding tube lens. While the microscope objective is built from several individual lenses, the elements are AR coated and the assembled package is sealed from contamination and dust. The optical performance (in terms of flatness, field of view, aberrations etc.) is far superior to simple two-lens setups.

In total the optical system achieves a fourfold magnification and with its numerical

aperture of  $NA = 0.14$  provides a theoretical resolving power<sup>12</sup> of about 2.5 microns. Design priority is given to the suppression of fringes and other interference effects; elements with plane surfaces (e.g. waveplates) are therefore slightly tilted away from normal incidence to further reduce back reflections.

### **One-way imaging - suppression of back reflections**

Interference fringes are particularly prone to jitter and other non-stationary behavior when the contributing reflections travel over long distances. This is for instance the case for parasitic reflections bouncing between the (uncoated) glass cell surface and the (broadband AR coated) CCD chip window. Given that high contrast interference fringes form already with relatively weak stray beams (the intensity scales quadratically with the electric field superposition, i.e. two overlapped beams with an intensity ratio of 100:1 can generate a fringe pattern with 20 percent contrast), AR coatings cannot completely eliminate the fringe issues.

Another way of suppressing back reflections is the implementation of an "optical diode" within the imaging setup; being placed in front of the CCD camera it could extinguish back reflected light from the CCD, preventing the above mentioned long-distance fringes. In the case of incoming light with linear polarization this imaging diode is easily set up by combining an appropriately aligned linear polarizer and quarter waveplate: in the forward direction the incoming linearly polarized light is transmitted through the polarizer and becomes circularly polarized after the waveplate. Once reflected from the CCD chip surface, the handedness of the circularly polarized beam is changed, so that in the reverse direction the waveplate turns the inverted circular polarization into orthogonal linear polarization that is then blocked by the polarizer. Achievement of optical isolation using this scheme requires that the reflection be specular and that no other polarization modifications occur - requirements mostly fulfilled by the CCD surface. Furthermore, given that orthogonally polarized beams cannot interfere, employing a polarizer is not mandatory; simply

---

<sup>12</sup>The actual resolving power of a diffraction limited imaging system depends on details of the illumination but is roughly given by  $\lambda/(2NA)$  with  $\lambda = 0.671$  nm being the illumination light wavelength.

adding a quarter waveplate in front of the camera can already significantly reduce interference fringes. It should be emphasized that unlike the atomic response the CCD camera output does not depend on the polarization state of the detected light.

In practice the effectiveness of this interference reduction scheme varies from setup to setup, depending on the origin of the fringes. Adding more optical elements can always introduce new interferences and particularly a polarizer will always cause unwanted attenuation.

### **3.4.2 Detector optimization for noise measurements**

Choosing an appropriate camera system and operating it with optimized settings plays a key role for obtaining high quality noise measurements. From the earlier discussion of the various noise contributions and constraints it is clear that the system has to comply with the following criteria:

- Reliable mechanical construction with rigid mounting options
- Quiet fan or water cooling to minimize intrinsic vibrations
- Complete shielding from stray light (recessed position of the sensor, easy interfacing with lens tubing, built-in mechanical shutter etc.)
- Adjustable conversion gain with low read noise
- Clean dark frames free from technical artifacts
- Good linearity over a wide dynamic range
- High quantum efficiency in the red / near-IR region
- Minimum number of optical surfaces between entrance window and sensor (all surfaces AR coated)
- Hardware pixel binning (the charge from neighboring pixels can be combined and read out as a superpixel)

- Precise external cleaning, trigger, exposure and readout control
- Ability to take two or more images in very fast succession (acquisition intervals of a few hundred microseconds or less)

While many of these requirements are met by most of the commercially available scientific camera systems, it is important to realize that most systems are not specifically designed for applications with coherent illumination. Very often cameras are equipped with pre-assembled sensor packages where the actual sensor chip is protected with an additional cover glass window causing unwanted reflections. Ideally a single wedged window (AR coated on both sides) is the only element between the chip surface and the camera aperture. The sensor itself is preferably an AR coated back-illuminated CCD<sup>13</sup> offering a quantum efficiency exceeding 90 percent in the red wavelength region. Unlike a normal front-illuminated device where the electrode wiring partially obscures the photocathodes, the back-illuminated sensor is manufactured such that the light-sensitive photocathode layer is directly facing the incoming light through a thinned substrate layer.

### **Fast Kinetics acquisition**

Regarding the fast acquisition criterion in the above list, several technologies have been developed to accomplish exposure repetition rates of 10 kHz and faster. With back-illuminated CCD sensors the method of choice is to operate the device in a special readout mode often called "Fast Kinetics Acquisition". In Fast Kinetics (FK) operation mode only a small fraction of the pixel array is exposed to light and the dark region acts as a temporary storage area into which the FK-subimages are shifted row by row. Depending on the number of subimages and the total vertical height of the particular CCD chip, each subimage can only have a proportionally reduced pixel height compared to a normally acquired image. The row-wise vertical charge transfer across the pixel array is very fast with shift times of a few  $\mu\text{s}$  per row. For an array

---

<sup>13</sup>Recently scientific CMOS sensors have been introduced. Their different parallel-readout sensor architecture makes it possible to achieve high-speed operation with very low read noise.

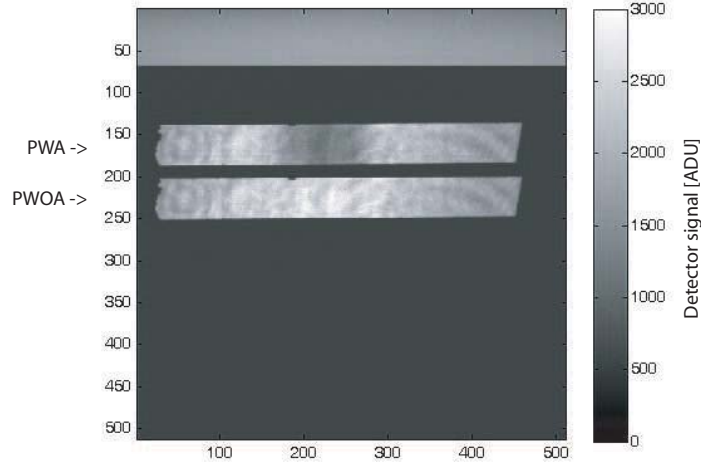


Figure 3-6: Unprocessed Fast Kinetics frame containing the image of an expanded atom gas cloud. The frame is vertically divided into eight subsections with the *PWA* image in subframe 3 and the *PWOA* image in subframe 4. Due to technical constraints subframe 1 is contaminated with parasitic charges and needs to be discarded. An electronic readout offset of about 500 ADU ensures positive integer output values for all pixels including those not exposed to light. By subtracting an analogous dark frame (*DF*) this offset is later removed. The time interval between the *PWA* and *PWOA* images amounts to  $450 \mu\text{s}$ .

with a total of 1024 rows one could therefore obtain 8 subimages each 128 pixels high with a wait time between the individual exposures of about  $400 \mu\text{s}$ . Figure 3-6 shows an example FK frame acquired with these parameters and read out using a  $2 \times 2$  hardware binning so that all pixel dimensions are scaled by a factor of two. While the row-wise vertical charge transport in FK mode is particularly fast, the completely filled CCD is eventually read out in the same fashion as a normally operated CCD device, i.e. via a slow ( $10 \mu\text{s}$  per pixel for low read noise) pixel by pixel readout process. CCD readout between the closely spaced subimages is therefore not a feasible experimental option.

Unless the image sensor is a specialized frame-transfer CCD with built-in opaque mask to cover the dark storage region it is important to ensure sufficient shielding of the storage pixels from any (stray)light, e.g. by attaching an external mask to the CCD chip and by employing relay imaging as shown in Figure 3-5 to generate sharp

black borders around the exposure region.

Several manufacturers offer suitable camera systems meeting the discussed criteria. The experiments reported in this thesis were performed with Princeton Instruments' PIXIS: 1024BR back-illuminated CCD camera. At 671 nm this thermoelectrically cooled detector provides about 90 percent quantum efficiency, its  $1024 \times 1024$  pixels measure  $13 \times 13 \mu\text{m}$ , the fastest vertical shift time is  $3.2 \mu\text{s}$  per row and the read noise is specified to be 3.6 electrons rms at 100 kHz readout speed / 16-bit ADU resolution with a conversion gain of one ADU per electron.

### Detector noise calibration

For quantitative atom noise measurements it is very important to independently verify the relevant detector parameters, in particular the values for the conversion gain  $c$  and the readout noise  $r$ . This is accomplished by acquiring a series of images under typical atom noise measurement timing conditions but without atoms present, i.e. the  $S_1 = PWA - DF$  and  $S_2 = PWOA - DF$  images will look alike. Subsequently a difference image  $S_{\text{diff}} = S_1 - S_2$  is generated<sup>14</sup> and within a central subregion of pixels with mean signal  $\bar{S} = \bar{S}_1 = \bar{S}_2$  the statistical variance  $\text{Var}(S_{\text{diff}})$  is measured. From the previous discussion of the various noise components and by the law of total variance one expects

$$\text{Var}(S_{\text{diff}}) = 2\bar{S}c + 4(rc)^2, \quad (3.18)$$

which suggests that  $c$  and  $r$  can be determined from a linear fit to a plot of  $\text{Var}(S_{\text{diff}})$  vs.  $\bar{S}$  that samples different mean signal levels  $\bar{S}$ . Figure 3-7 presents such a plot derived from 274 atom-free image pairs yielding values of  $c = 1.07 \pm 0.005 \text{ ADU}/e^-$  and  $r = 3.45 \pm 0.3 e^-$  in good agreement with the quoted data sheet specifications.

Note that the above camera noise calibration is carried out in a "horizontal" fashion, i.e. the variance is determined from many pixels within one difference image

---

<sup>14</sup>Typically a slight scaling correction is applied to  $S_2$  in order to compensate for residual intensity fluctuations between the two exposures.

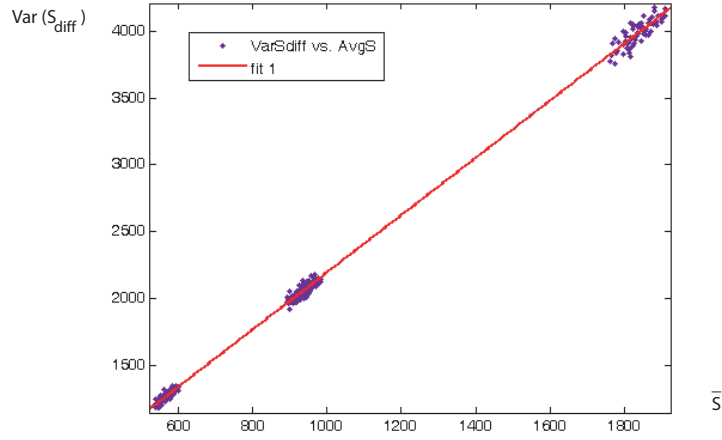


Figure 3-7: Detector noise calibration fit. The measured dependence of detector difference-signal variance on average signal level makes it possible to determine via equation (3.18) the camera conversion gain  $c$  and the read noise  $r$ . Each difference image  $S_{\text{diff}}$  delivers one variance data point and the 274 contributing images were either obtained with low, medium or high illumination intensity.

and not "vertically" for one pixel across many images. Subtracting instead of dividing  $S_1$  and  $S_2$  ensures correct statistics even if the pixels in the analysis subregion are not uniformly illuminated.

### Fast atom depumping

With the very short time span between the exposures for the *PWA* and *PWOA* images (to minimize normalization imperfections) the removal of atoms from the detector field of view after the first exposure becomes a nontrivial problem. In standard imaging setups hundreds of milliseconds between the two exposures mean that with traps being switched off the atoms can simply disappear by falling down in gravity. Oppositely, within the short FK interval of just  $450 \mu\text{s}$  any "mechanical" displacement will not suffice to timely remove the atoms.

There are various other possibilities to clear the field of view - all of them rely on the concept of making the atoms invisible by shifting the atom - light interaction far away from resonance. This can for instance be achieved by quickly adjusting

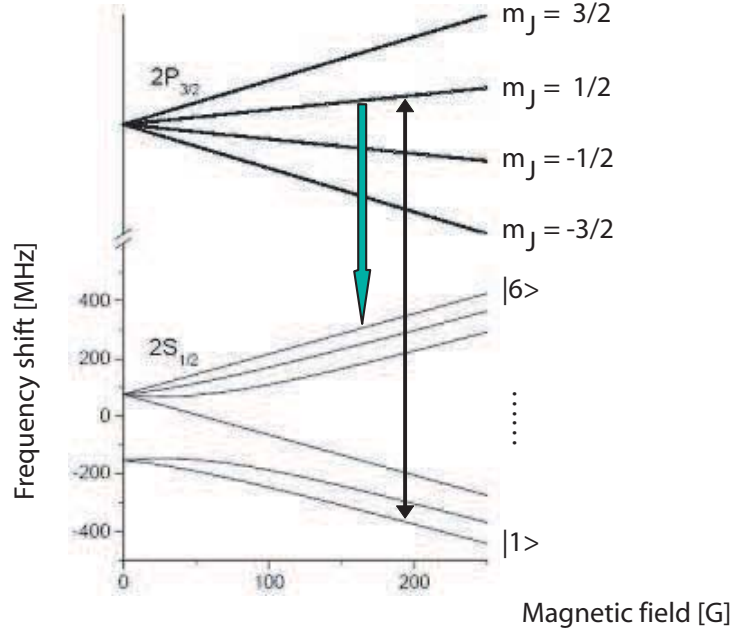


Figure 3-8: Zeeman splitting diagram of the  ${}^6\text{Li}$   $D_2$  line illustrating the optical depumping scheme employed in combination with FK imaging. The spin mixture of state  $|1\rangle$  and  $|2\rangle$  atoms is optically pumped (thin arrow) into the excited state  $m_J = 1/2$  manifold. From there the atoms can decay (thick arrow) down to states  $|6\rangle$  and  $|5\rangle$ . To achieve a symmetric pumping of the spin mixture components the pumping light frequency is tuned halfway between states  $|1\rangle$  and  $|2\rangle$ . A higher pump beam intensity compensates for the reduction in scattering rate. For typical experimental parameters all atoms are depumped within  $100 \mu\text{s}$ .

the imaging light frequency after the first exposure so that the *PWOA* image is obtained with light tuned hundreds of megahertz away from the atomic transition. At this detuning the absorption by the expanded gas cloud is negligible and the acquired image appears atom-free. Practically this approach finds its limit in the fact that parasitic interference fringes themselves are by their very nature sensitive to frequency changes; depending on the effective "interferometer length" even very small detunings of tens of megahertz cause sufficient fringe shifts rendering the resulting *PWOA* image useless for normalization purposes. Other methods like a sudden change of the magnetic bias field (to induce Zeeman shifts of the involved atomic energy levels) or switching the handedness of the circularly polarized imaging light (with the opposite  $\sigma$ -transition being far away) do avoid the laser light detuning

complications but suffer from other shortcomings, e.g. mechanical vibrations induced by sudden current changes in the bias field coils or residual polarization asymmetries in the imaging setup leading to normalization imperfections.

Instead of modifying various imaging parameters between the *PWA* and *PWOA* acquisitions it is more advantageous to manipulate the atoms themselves by changing their internal state via optical pumping. Figure 3-8 illustrates a possible depumping scenario. At magnetic fields of a few hundred Gauss the excited  $2P_{3/2}$  state in  ${}^6\text{Li}$  is split into four  $m_J$  manifolds, each containing three spectroscopically not resolved  $m_I$  states<sup>15</sup>. The standard cycling imaging transition at these fields along the magnetic field lines connects the  $|1\rangle$  and  $|2\rangle$  ground states to the  $m_J = -3/2$  excited state manifold. Alternatively one could also drive transitions to the  $m_J = -1/2$  and  $m_J = 1/2$  manifolds but these transitions are not closed and will eventually pump all atoms into the  $m_J = 1/2$  ground state manifold, i.e. to states  $|6\rangle$  and  $|5\rangle$  as depicted in Figure 3-8 for the  $m_J = 1/2$  excited state case. By driving these pumping transitions via an off-axis beam directly after the acquisition of the *PWA* image one can therefore shuffle the state  $|1\rangle$  and  $|2\rangle$  atoms completely into states  $|6\rangle$  and  $|5\rangle$  where they are invisible (at 527G detuned by almost 2 GHz) with the original imaging light. The subsequently under identical imaging conditions obtained *PWOA* image will be atom-free but illuminated exactly like the *PWA* image guaranteeing a perfect background normalization.

### 3.4.3 Further improvement strategies - Coherent vs. incoherent illumination

While the above described Fast Kinetics acquisition in combination with the optical depumping scheme is able to reliably deliver clean photon shot noise limited density images, various other measurement approaches and improvement strategies are worth considering. Among them are the application of a counter propagating slowing beam overlapped with the normal imaging beam to address the recoil induced Doppler

---

<sup>15</sup>At high magnetic fields the  $I = 1$  nuclear spin of the  ${}^6\text{Li}$  atom is decoupled from the electron and cannot be flipped in an electric dipole transition.

detuning or attempts to actively flatten the imaging beam profile by scrambling the spatial coherence of the illumination light.

Experimentally implemented the concept of a recoil balancing counter propagating imaging beam proved successful when trying to partially recover lost optical density (cf. Figure 3-4), but corresponding improvements regarding the nonlinear fringe imprint were eventually outweighed by stray light and back reflection issues that are hardly avoidable when operating a counter propagating beam. Despite eventually also not being implemented the coherence scrambling approach is worthy of discussion because it is conceptually insightful and touches on the topic of laser speckle which is of particular relevance for the next chapter.

### **Scrambling the spatial coherence of laser light with rotating diffusers**

All the previously analyzed fringe issues would be absent if incoherent illumination were used. Narrow-linewidth lasers achieve coherence lengths<sup>16</sup> easily exceeding hundreds of meters making it difficult to spatially decohere the light, but it is nevertheless possible to generate pseudo-incoherent illumination with a narrow-linewidth laser source by rapidly time-averaging over many random interference patterns during a single exposure. A laser speckle pattern<sup>17</sup>, being the prototype of a random fragmented interference pattern, is the ideal starting point for such a procedure. In a coherent imaging system full contrast laser speckle is encountered every time when large scale phase ripples<sup>18</sup> on a length scale smaller than the spatial resolution of the system get imprinted on the imaging light wavefront [48]. Accordingly, in the context of the imaging setup depicted in Figure 3-5 a speckle field illuminating the atom cloud can be created by placing a ground glass diffuser or another phase scrambling element at the position of the iris diaphragm. Typical diffusers exhibit submicron phase graininess well below the resolving power of the projection and imaging lenses leading to a speckle pattern in the illumination light with a distribution of scale sizes

---

<sup>16</sup>Depending on the particular definition of spectral width, coherence length  $L_c$  and laser linewidth  $\Delta\lambda$  are in vacuum related via  $L_c = (2 \ln 2/\pi) (\lambda^2/\Delta\lambda)$  for a Gaussian frequency spectrum with  $\Delta\lambda$  measured as FWHM width.

<sup>17</sup>Chapter 4 will discuss laser speckle in more detail.

<sup>18</sup>phase excursions by more than  $2\pi$

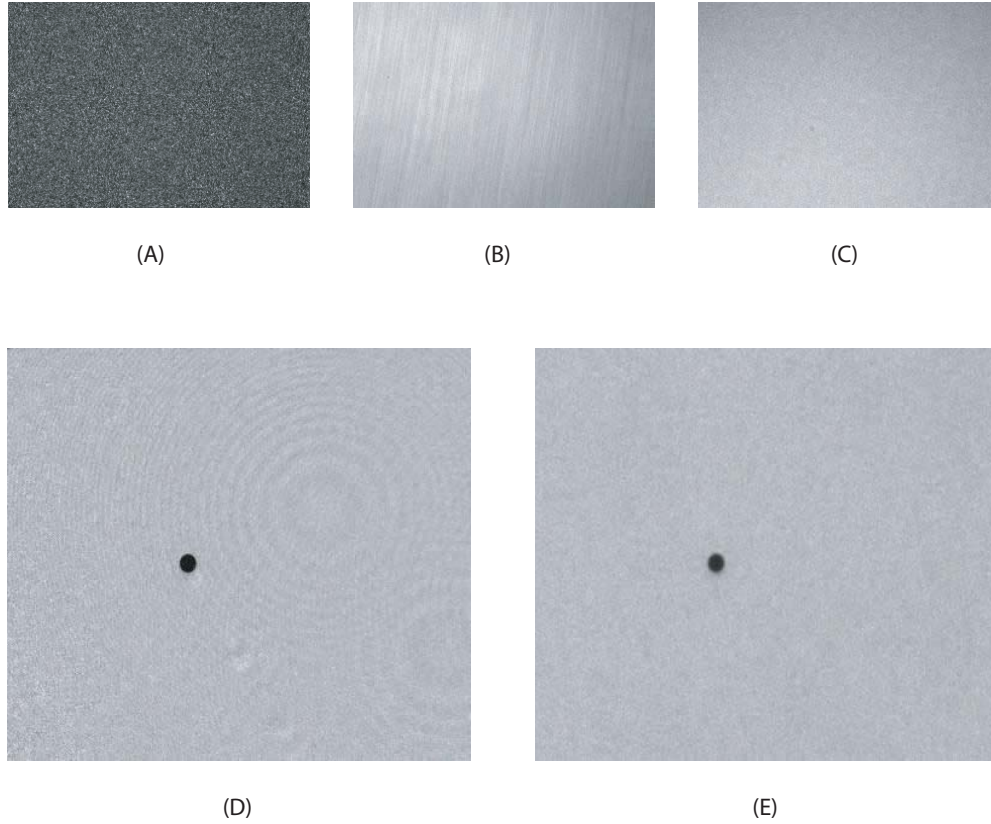


Figure 3-9: Atom cloud imaging with incoherent illumination. Placing a static ground glass diffuser into the coherent illumination beam generates a speckle pattern in the observation plane (A). Setting the diffuser disk into motion causes the speckle pattern to move during the exposure interval and the camera records a time-averaged image (B). Further flattening is achieved by employing a two-diffuser configuration with one static and one rotating diffuser (C). Example absorption images of a trapped cloud of sodium atoms illustrate the differences between coherent (D) and incoherent (E) illumination.

ranging from large-scale-size fluctuations down to a small-size cutoff given by the resolving power of the projection/imaging system. Figure 3-9 shows with picture (A) a raw *PWOA* image acquired with such a diffuser in place. The irradiance of different pixels covers the full range from maximum intensity down to zero and is expected to obey negative exponential statistics [48].

In order to randomize and flatten this illumination field one can now dynamically change the imprinted phase ripple (and with it the resulting intensity speckle pattern)

by constantly rotating the diffuser disk during the exposure interval. This procedure delivers raw images similar to picture (B). While the full scale contrast of picture (A) is greatly reduced through the averaging process, the image is still not photon shot noise limited and shows residual streak patterns from the diffuser rotation. More quantitatively, the attainable speckle contrast reduction ratio [49] for a single rotating diffuser is given by  $\Delta J/\langle J \rangle = \sqrt{L_0/X}$ , where  $\langle J \rangle$  denotes the mean of the observed illuminance and  $X$  is the total displacement of the diffuser during the exposure interval.  $L_0$  quantifies the image speckle autocorrelation radius, i.e. the typical size of a speckle grain in the image plane, which approximately equals the resolving power of the imaging system, so that  $L_0 = \lambda/(2NA)$  with illumination light wavelength  $\lambda$  and imaging setup numerical aperture  $NA$ . In short, the ratio  $N = X/L_0$  measures the number of independent speckle patterns contributing to the averaging within a single exposure and consequently one finds  $\Delta J/\langle J \rangle = 1/\sqrt{N}$ .

To further improve the illuminance flatness one could increase  $N$  by simply rotating the diffuser at a higher speed, but more efficiently  $N$  is increased by adding a second stationary diffuser directly before the moving diffuser. In this configuration the diffuser displacement necessary to regenerate an independent speckle pattern is not anymore set by  $L_0$  but rather given by the diffuser's phase graininess correlation length<sup>19</sup>  $L$  which is for ground glass typically on the order of a few hundred nm and therefore by about an order of magnitude smaller than  $L_0$ . Furthermore, for the two diffuser configuration  $\Delta J/\langle J \rangle = \sqrt{L/X}$  does not anymore depend on optical parameters of the imaging system, but only on the diffuser's microscopic properties. Raw image (C) in Figure 3-9 illustrates the significant improvement in illuminance flatness compared to image (B); the diffuser rotation speed and exposure time was unchanged between both images, only a second stationary diffuser was added. Picture (E) of the same figure shows an absorption image of a trapped sodium gas cloud obtained with the two-diffuser setup; the comparison with a standard absorption image (D) of a similar cloud reveals the fringe suppression qualities of incoherent illumi-

---

<sup>19</sup>This is a sensible result: The compound diffuser establishes a new random phase pattern once the individual diffusers are displaced by more than  $L$  relative to each other.

nation. Additionally there are other more subtle differences between coherent and (pseudo)incoherent illumination (regarding theoretical resolving power, phase object response, spectral broadening etc.) that are discussed in detail in reference [48]. Some of these side effects, the reliability and cleanliness of the Fast Kinetics acquisition, mechanical complications accompanying high-speed diffuser rotation and the enormous intensity loss due to two diffusers led eventually to the continued use of coherent illumination for the experiments discussed in this thesis.

### 3.4.4 Depth of field considerations

Microscopic imaging is usually idealized as a 2D to 2D mapping process with an object plane and a correspondingly chosen in-focus image plane. Typically the assumption of a flat thin object is experimentally not met and the axial (along the optical axis) resolving power, i.e. the depth of field (*DOF*) of the imaging system becomes a concern. Analogously to the lateral resolution the axial resolution is determined by the numerical aperture (*NA*) of the imaging objective lens. This is most easily seen by revisiting the concepts of Gaussian beam optics<sup>20</sup>. Starting from a beam with a waist radius  $W_0$  equivalent to the intended lateral in-focus resolution one finds [47] for the axial range over which the beam does not diverge by more than a factor of  $\sqrt{2}$  the expression

$$2z_0 = \frac{2\pi W_0^2}{\lambda}, \quad (3.19)$$

where  $z_0$  is the so-called Rayleigh range of the Gaussian beam and  $\lambda$  denotes the illumination light wavelength. To resolve a beam waist  $W_0$  it is necessary to employ a focusing lens with a numerical aperture satisfying  $W_0 \approx \lambda/(\pi NA)$  and therefore a laterally fully utilized numerical aperture is associated with a maximum depth of field (ignoring prefactors of order 1) of

---

<sup>20</sup>For a detailed understanding of the 3D resolving power one could alternatively analyze the out-of-focus size of an Airy diffraction disk but for the purpose of obtaining insightful scaling relations it is sufficient to refer to the properties of Gaussian beams.

$$DOF \approx 2z_0 \approx \frac{\lambda}{NA^2}. \quad (3.20)$$

In contrast the aforementioned lateral resolution for the given  $NA$  scales like

$$2W_0 \approx \frac{\lambda}{NA}. \quad (3.21)$$

Since the diffraction-limited depth of field shrinks inversely with the square of the numerical aperture it is obvious that the lateral noise analysis resolution (i.e. the lateral column bin size) must be chosen carefully such that the corresponding depth of field is compatible with the axial atom sample thickness; otherwise one atom would signal-wise contribute to several neighboring bins falsifying the counting statistics. For instance, from the above relations a 1 mm thick sample roughly requires a lateral resolution of not better than 25  $\mu\text{m}$  to avoid significant counting bin crosstalk. A systematic experimental study reported in the following sections confirmed these estimates.

It is worth noting that an in-depth three-dimensional diffraction analysis [46] of the imaging system would reveal that lateral resolution and depth of field are also affected by the numerical aperture of the illumination and the degree of coherence. These more subtle effects cause typically small corrections up to a factor of 2 and are therefore not considered in detail.

### 3.5 Data acquisition and analysis

Under ideal conditions it is possible to distinguish by eye an image with increased atom noise from an image containing very little noise, but normally the noise extraction from a series of images is a rather involved process that is carried out via computer following a specifically programmed procedure. The next paragraphs will discuss this procedure and related aspects.

### 3.5.1 Horizontal statistics vs. vertical stack analysis

Having iteratively acquired many images of Fermi gas clouds prepared under identical conditions there are naturally two options to perform a noise analysis. As mentioned before one can either compare pixels of the same average optical density within a single image (horizontal analysis) or do counting statistics along different images for the same pixel or super-pixel bin (vertical analysis). While both approaches have specific advantages and disadvantages, it turns out that the vertical stack procedure is more versatile and delivers more consistent results.

The most severe shortcoming of the horizontal approach is the mixed analysis of spatially separated pixel regions. Even with a careful grouping of equivalent OD pixels it is notoriously difficult to minimize systematic OD variations that lead to a broadening in the OD distributions. Furthermore, the number of contributing pixels for each OD group is very limited (depending on total cloud size and pixel binning) and one loses the ability to directly generate a full 2D noise profile of the atom cloud. Nevertheless, this comparison leads to a more general interpretation of the noise extraction process along the lines of a spatial frequency Fourier image analysis.

#### Fourier noise analysis

Any two-dimensional number array can be Fourier decomposed into contributions from periodic functions of various spatial frequencies. Given the standard expression for the Fourier transform  $F$  of the input function  $f$

$$F(\nu_x, \nu_y) = \int \int f(x, y) \exp[2\pi i (\nu_x x + \nu_y y)] dx dy, \quad (3.22)$$

the Fourier decomposition reads

$$f(x, y) = \int \int F(\nu_x, \nu_y) \exp[-2\pi i (\nu_x x + \nu_y y)] d\nu_x d\nu_y \quad (3.23)$$

and can be adapted to a discrete array by replacing the integrals with appropriate

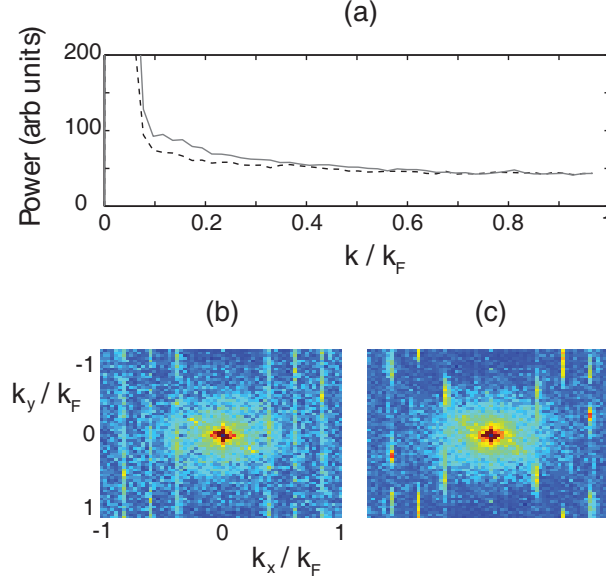


Figure 3-10: Radially averaged power spectra of optical density images for hot (solid line) and cold (dashed line) samples (a). Power spectrum of cold sample (b). Power spectrum of hot sample (c). A constant offset is added to the power spectrum for the hot sample to equalize the levels of photon shot noise. Each spectrum is obtained by averaging over 50 raw images.

sums. Special algorithms of the FFT (Fast Fourier Transform) type make it possible to efficiently compute the discrete Fourier transform. The so obtained power spectrum  $|F(\nu_x, \nu_y)|^2$  contains all relevant atom noise information - to some extent it is the physically most insightful representation of the atom noise because the spatial frequency can be plotted in units of the Fermi wave vector<sup>21</sup>.

In practice however, the raw spectrum of a single absorption image is not very clean due to a limited signal-to-noise ratio and low frequency contributions from the gas cloud envelope profile. Averaging the noise spectra of many individual images and high-passing can alleviate these effects. Figure 3-10 shows typical results of such a procedure for cold ( $T = 0.2 T_F$ ) and hot ( $T = 0.6 T_F$ ) Fermi gas clouds.

<sup>21</sup>For spatial frequencies well above the Fermi wave vector  $k_F$  one would not expect to observe noise suppression due to Fermi statistics since the corresponding resolution element becomes smaller than the Fermi wavelength. In other words a momentum transfer above  $2\hbar k_F$  to any particle will not be Pauli suppressed by occupation of the final state. For this limit one would expect to measure the full Poissonian localization noise.

Because the Fourier transform of uncorrelated fluctuations is flat, the deviation from flatness of the density noise corresponds to blurring induced by the imaging system, barring the central peak corresponding to the shape of the cloud. For wave vectors  $k$  much larger than the resolution limit of the detection scheme, the atom number fluctuations are no longer imaged, and the power spectrum is the photon shot noise. For this experiment this happens for  $k < k_F$ . Comparison of the power spectra for the cold and the hot cloud shows, at small values of  $k$ , a 50 percent suppression, consistent with the later results obtained using spatial bins in vertical stacks. If the imaging system still had contrast at  $k > 2k_F$ , one would expect the ratio of the power spectra to approach unity, since momentum transfer  $\hbar k > 2\hbar k_F$  to a Fermi cloud has negligible Pauli suppression.

In the language of this frequency-resolved horizontal analysis, the vertical stack approach appears as a localized band-passed version of the full noise spectroscopy with the high frequency cutoff set by the axial bin size and the low frequency roll-off defined by the cloud envelope profile subtraction process. The next paragraph will provide a systematic outline of the vertical noise extraction procedure.

### 3.5.2 The vertical noise measurement procedure

The noise extraction process is comprised of several steps:

1. Acquisition of 50 - 100 high-quality resonant optical density ( $OD$ ) images of expanded Fermi gas clouds under identical conditions.
2. Automatic and manual preselection of images to eliminate outliers regarding imaging light intensity, total atom number and background flatness.
3. Optional software binning to create super-pixels (2x2, 3x3 etc.) from the hardware-wise defined elementary pixels.
4. Generation of an average  $\langle S_2 \rangle = \langle PWOA - DF \rangle$  image and an average  $\langle OD \rangle$  image for photon shot noise subtraction purposes.
5. Fitting a two-dimensional Gaussian envelope to each atom cloud image.

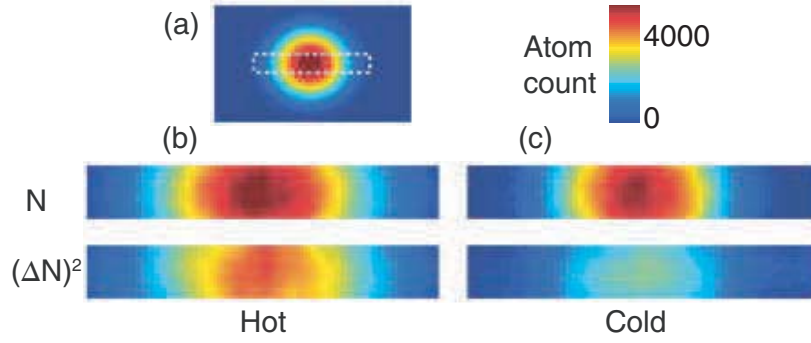


Figure 3-11: Comparison of density images to variance images. For Poissonian fluctuations, the two images at a given temperature should be identical. The variance images were obtained by determining the local density fluctuations from a set of 85 images taken under identical conditions. (a) Two dimensional image of the optical density of an ideal Fermi gas after 7 ms of ballistic expansion. The noise data were taken by limiting the field of view to the dashed region of interest, allowing for faster image acquisition. (b) For the heated sample with  $T = 0.6 T_F$ , variance and density pictures are almost identical, implying only modest deviation from Poissonian statistics. (c) Fermi suppression of density fluctuations deep in the quantum degenerate regime at  $T = 0.2 T_F$  manifests itself through the difference between density and variance picture. Especially in the center of the cloud, there is a large suppression of density fluctuations. The variance images were smoothed over  $6 \times 6$  bins. The width of images (b) and (c) is 2 mm.

6. Further high-pass filtering of the fit residual by applying a square matrix averaging filter. The matrix size is appropriately chosen so that only long-range low-frequency features are removed; the pixel-to-pixel fluctuations are preserved.
7. Computing the vertical variance  $(\Delta OD)^2$  for each (super-)pixel along all preselected images.
8. Via the knowledge of  $\langle S_2 \rangle$  and  $\langle OD \rangle$  computation (cf. equation (3.12)) of the expected amount of optical density photon shot noise  $(\Delta_{\text{ph}} OD)^2$  that is contained in the measured  $(\Delta OD)^2$  matrix.
9. Subtraction of the detector readout noise augmented  $(\Delta_{\text{ph}} OD)^2$  from  $(\Delta OD)^2$  to obtain the final atom noise variance image  $(\Delta_{\text{atom}} OD)^2$ .

As already mentioned due to its local character this scheme turned out to deliver the most reliable and consistent measurements. Results obtained for a cold vs. hot Fermi gas cloud are displayed in Figure 3-11. Cold and hot samples were prepared with similar cloud sizes and central optical densities to ensure that they were imaged with the same effective absorption cross section and resolution. The cold cloud shows a distinct suppression of the atom number variance, especially in the center of the cloud where the local  $T/T_F$  is smallest. In the given example the individual probe volumes (super-pixel columns), in which the numbers of atoms are counted, are chosen to be  $26 \mu\text{m}$  in the transverse directions, and extend through the entire cloud in the direction of the line of sight (cf. above depth of field discussion).

### 3.5.3 Scattering cross section calibration

While Figure 3-11 seamlessly seemed to make the transition from optical densities to actual atom numbers per counting bin, this conversion is a crucial step towards obtaining quantitative results. From the context of equations (3.5) and (3.15) it is clear that for an absorption cross section  $\sigma_0$  the atom content of a pixel column of transverse area  $A$  and optical density  $OD$  is given by

$$N = \frac{A}{\sigma_0} OD \quad \text{with fluctuations} \quad \Delta N = \frac{A}{\sigma_0} \Delta OD. \quad (3.24)$$

For the employed cycling transition at imaging wavelength  $\lambda$  the theoretical low-intensity resonant absorption cross section [42] is

$$\sigma_0 = \frac{3}{2\pi} \lambda^2, \quad (3.25)$$

but even when taking higher-intensity nonlinear corrections into account this value is experimentally rarely achieved. From the measurements reported in Figure 3-4 one can empirically infer at the chosen probe light intensity a 20 % reduction of the cross section compared to its low-probe-intensity limit. For  $\lambda = 671 \text{ nm}$  this leads to a

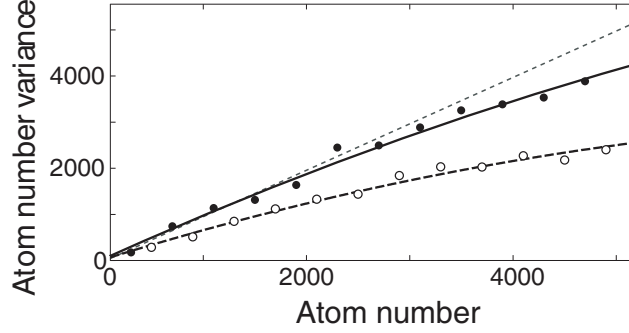


Figure 3-12: Atom number variance vs. average atom number. For each spatial position, the average atom number per bin and its variance were determined using 85 images. The filled and open circles in the figure are averages of different spatial bin positions with similar average atom number. For a hot cloud at  $T/T_F = 0.6$  (filled circles), the atom number variance is equal to the average atom number (dotted line, full Poissonian noise) in the spatial wings where the atom number is low. The deviation from the linear slope for a cold cloud at  $T/T_F = 0.21$  (open circles) is due to Pauli suppression of density fluctuations. There is also some suppression at the center of the hot cloud, where the atom number is high. The solid and dashed lines are quadratic fits for the hot and cold clouds to guide the eye.

value of  $\sigma_0 = 1.71 \times 10^{-13} \text{ m}^2$ . This is an upper limit to the cross section due to imperfections in polarization and residual line broadening.

An independent estimate of the effective cross section of  $1.48 \times 10^{-13} \text{ m}^2$  was obtained by comparing the over the whole cloud integrated optical density to the number of fermions necessary to fill up the trap to the chemical potential. With known trap parameters the value of the chemical potential was obtained from fits to the ballistic expansion pictures that allowed independent determination of the absolute temperature and the fugacity of the gas [50]. The effects of a not fully characterized weak residual magnetic field curvature on trapping and on the ballistic expansion made it difficult to precisely assess the accuracy of this value of the cross section.

The most accurate value for the effective cross section was determined from the observed atom shot noise itself. Instead of displaying the noise measurement results in a spatially resolved fashion one can alternatively re-sort data points such that the number variance of each vertical bin stack is plotted against its mean atom number.

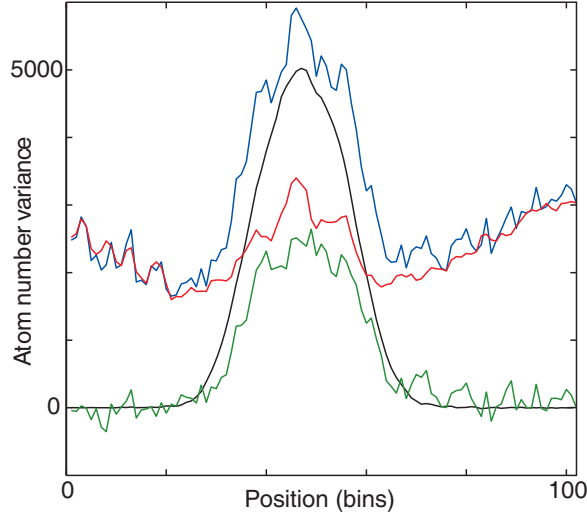


Figure 3-13: Determination of profiles of the atom number variance for a cold Fermi gas cloud. For each bin, the total photon count is determined, and its contribution (red) to the total variance of the optical density (blue) is subtracted. The obtained atom number variance (green) is compared to the average atom number (black). The displayed trace reveals 50 % noise suppression in the center of the cloud. The apparently high suppression of atom variation in the wings is a statistical fluctuation. Figure 3-12 shows that the suppression is monotonic in atomic density.

Figure 3-12 shows the processed outcome of such a strategy. The atom shot noise in the wings of the hottest cloud must be Poissonian, i.e.  $(\Delta N)^2 = N$ , and this condition together with equation (3.24) determines the absorption cross section. Requiring that the slope of variance of the atom number  $(\Delta N)^2$  vs. atom number  $N$  is unity results in a value of  $(1.50 \pm 0.12) \times 10^{-13} \text{ m}^2$  for the effective cross section in good agreement with the two above estimates.

## 3.6 Measurement results and interpretation

### 3.6.1 Comparison of theory and experiment

Given the theoretical insight developed in chapter 2 one can compare the experimental findings with the theoretical predictions for a noninteracting Fermi gas. The com-

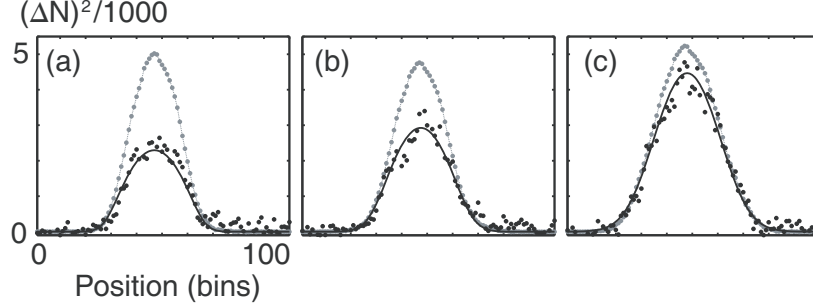


Figure 3-14: Comparison of observed variances (black dots) with a theoretical model (black line) and the observed atom number (gray), at three different temperatures (a, b, and c), showing 50, 40, and 15 % suppression. Noise thermometry is implemented by fitting the observed fluctuations, resulting in temperatures  $T/T_F$  of  $0.23 \pm 0.01$ ,  $0.33 \pm 0.02$ , and  $0.60 \pm 0.02$ . This is in good agreement with temperatures  $0.21 \pm 0.01$ ,  $0.31 \pm 0.01$ , and  $0.6 \pm 0.1$  obtained by fitting the shape of the expanded cloud [50]. The quoted uncertainties correspond to one standard deviation and are purely statistical.

parison is simplified by first averaging the measured two-dimensional noise profiles (see Figure 3-11) along the short axis of the images. Using one-dimensional profiles obtained by such averaging Figure 3-13 further illustrates the previously delineated noise extraction process by explicitly showing the contributions of photon and atom number variance to the overall noise in optical density.

### Noise thermometry

With known trap parameters and employing the results from chapter 2, in particular equation (2.19) together with the local density approximation, it is straightforward to numerically generate theoretical 1D profiles of the noise variance for a gas cloud of known temperature. Figure 3-14 presents the comparison of theory and experiment for three different temperatures. Given that the observation of density fluctuations determines the product of temperature and compressibility (see equation (2.7)), it provides an absolute thermometer as demonstrated in Figure 3-14, if the compressibility is known or is experimentally otherwise determined. Because variance is proportional to temperature for  $T \ll T_F$  as seen in equation (2.20), noise thermometry maintains its sensitivity at very low temperature, in contrast to the standard technique of fit-

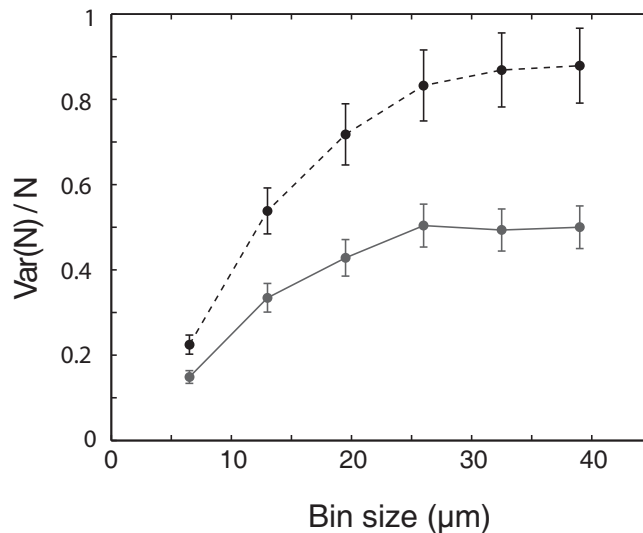


Figure 3-15: Observed atom number variance versus bin size for heated (dashed line) and cold (solid line) Fermi gas samples, normalized to 1 for Poissonian statistics. A plateau is reached when the blurring of the bins due to finite optical resolution is negligible.

ting spatial profiles. The good agreement between theory and experiment as found in Figure 3-14 underlines the practical relevance of this thermometry method.

### 3.6.2 Atom counting contrast saturation

One very essential aspect of the imaging system that has already been touched upon in the context of depth of field considerations (cf. equation (3.20)) is to choose appropriate lateral and axial resolutions. Without matching these to the sample size, the blurring of adjacent pixel columns (probe bins) due to finite optical resolution could effectively decrease the measured atom number variance. This effect is avoided by binning the noise data using a sufficiently large bin size. Experimentally this minimum size is determined by varying the probe bin size (software binning) and verifying that the measured relative atom noise becomes independent from the probe bin dimensions, i.e. saturates from a certain bin size on. Figure 3-15 presents the

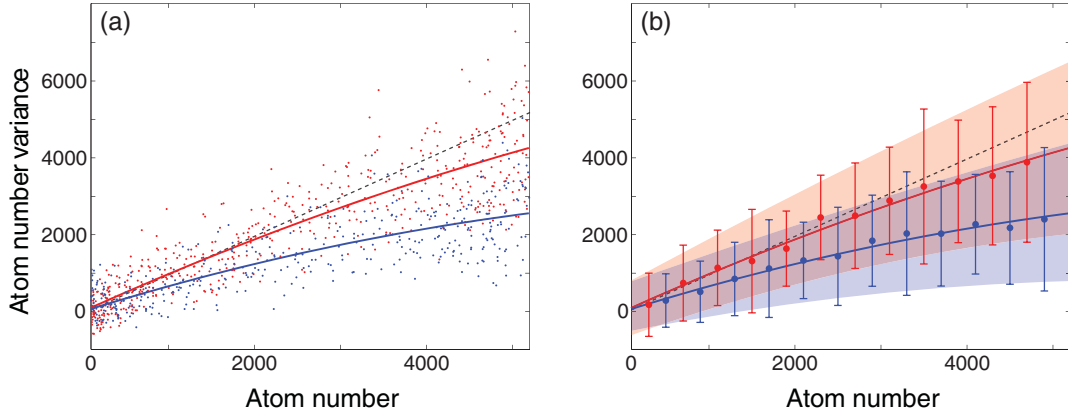


Figure 3-16: Atom number variance vs. atom number. (a) Data for all of the resolution elements is plotted. Red points are from the hot cloud at  $T/T_F = 0.6$ , blue points from the cold cloud at  $T/T_F = 0.21$ . There is significant scatter in the variance data, and there are many "cold" pixels which actually have higher variance than their corresponding "hot" pixel. (b) The red and blue shaded regions indicate the expected  $2\sigma$  scatter in sample variance that is expected due to atom and photon counting statistics. The large circles are variance data averaged over pixels with similar atom number for the hot (red) and cold (blue) cloud. The bars show the measured  $2\sigma$  scatter of the data points. The measured scatter agrees very well with the expected scatter, indicating that the scatter of the data is fully accounted for by counting statistics. Negative values of the observed atom number variance result from the subtraction of photon shot noise.

outcome of such a measurement and confirms that the saturation plateau is roughly reached for probe bins larger than  $25 \mu\text{m}$ .

### 3.6.3 Noise in the noise

Noise measurements are subject to error bars. Besides the discussed systematic effects like nonlinear bleaching these errors are associated with finite statistical sampling of the quantity of interest, i.e. determining the variance of a variable via a finite number of data points leads to a statistical measurement uncertainty for the variance itself. Figure 3-16 is the raw version of Figure 3-12 and further illustrates the scatter of the measured atom number variance. This scatter is not primarily due to technical noise, but instead a statistical property of the sampling distribution of the variance. The shaded areas are derived from theoretical values for the variance of the sample

variance. This is given by

$$\text{Var}(\text{Var}(N)) = \frac{(m-1)^2}{m^3} \mu_4 - \frac{(m-1)(m-3)}{m^3} \mu_2^2, \quad (3.26)$$

where  $m$  is the number of observations in each sample [51]. The moments  $\mu_2$  and  $\mu_4$  are the central moments of the population distribution. For a Poisson distribution,  $\mu_2 = \langle N \rangle$  and  $\mu_4 = \langle N \rangle(1 + 3\langle N \rangle)$ , and for  $m, \langle N \rangle \gg 1$ , this expression reduces to  $2\langle N \rangle^2/m$ . Figure 3-16 (b) shows the comparison between the expected and measured variance in the sample variance. While other minor effects might contribute to the error budget it is clear from these results that counting statistics is mostly responsible for the scatter of the variance data points.

In conclusion, this chapter reported on the successful observation of suppressed density fluctuations in a quantum degenerate Fermi gas. A sensitive technique for determining atomic shot noise has been established. Parallel research performed by the ETH group in Zurich led to similar results as presented in [52, 53].

The next chapter describes further progress towards the adaption of the noise measurement technique to the in situ study of strongly interacting Fermi gases along the BEC-BCS crossover.

# Chapter 4

## Measuring fluctuations in a strongly interacting Fermi gas

*This chapter focuses on the experiment reported in the following publication: C. Sanner, E. J. Su, A. Keshet, W. Huang, J. Gillen, R. Gommers, and W. Ketterle, “Speckle Imaging of Spin Fluctuations in a Strongly Interacting Fermi Gas”. Included in Appendix B.*

Given the previous chapter’s results on quantitative noise measurements in noninteracting Fermi gases it is promising to generalize this approach and apply it to a broader range of quantum gases. This chapter introduces the technique of speckle imaging as a simple and highly sensitive *in situ* method to characterize fluctuations. Using speckle imaging the susceptibility and compressibility of a two-component Fermi gas are studied across the BEC-BCS crossover. Fluctuations in the magnetization, i.e., the difference of the densities in the two different spin components, are directly measured, bypassing the need to measure the individual densities separately.

## 4.1 Properties of an interacting two component Fermi gas

With the onset of interactions a rich set of new phenomena can be observed in an ultracold Fermi gas. The underlying physics of Feshbach resonances and the BEC-BCS crossover have been discussed extensively in numerous publications [36, 54]. Therefore, instead of detailing the relevant derivations, only the main conceptual steps that lead to a theoretical understanding of the interacting gas are sketched in table form and then an oversimplified but very intuitive physical picture of a Fermi gas in the unitary limit [55] is presented.

### 4.1.1 From elastic collisions to Feshbach resonances

The natural starting point to understand the interacting gas is the corresponding two-body problem:

- 1) At large enough distances the interaction between the two particles of mass  $m$  is approximately described by a position-dependent van der Waals potential  $V(r) \approx -C_6/r^6$ . The quantum mechanical range  $b$  of this potential is defined with the corresponding wave vector via  $\hbar^2/(mb^2) = C_6/b^6$ . Only low-energy scattering with relative momentum  $k \ll b^{-1}$  is considered.
- 2) The scattering amplitude  $f_k$  for elastic collisions in the center-of-mass frame of the two atoms is obtained by solving the Schrödinger equation

$$E\phi = [-\hbar^2/m \Delta_{\mathbf{r}} + V(\mathbf{r})] \phi. \quad (4.1)$$

Scattering eigenstates with positive energies  $E = \hbar^2 k_0^2/m$  are written as  $\phi = \phi_0 + \phi_s$  with the incoming plane wave  $\phi_0 = \exp(i\mathbf{k}_0 \cdot \mathbf{r})$  and the outgoing spherical wave  $\phi_s \approx f_{\mathbf{k}_0}(\mathbf{r}/r) \exp(ik_0 r)/r$ . Assuming that the potential scatters only in the s-wave the scattering amplitude is isotropic, i.e.  $f_{\mathbf{k}_0}(\mathbf{r}/r) = f_{k_0}$ .

3) With the optical theorem [56] it follows that  $|f_{k_0}|^2 = k_0^{-1} \text{Im} f_{k_0}$  and therefore<sup>1</sup>

$$f_{k_0} = -\frac{1}{s(k_0) + \imath k_0} \quad (4.2)$$

with  $s(k_0)$  being a real and even function of  $k_0$ .

4) Via the low- $k$  expansion

$$f_{k_0} = -\frac{1}{a^{-1} + \imath k_0 - k_0^2 r_e/2 + \dots} \quad (4.3)$$

the scattering amplitude is parametrized by the scattering length  $a$  and the effective range  $r_e$ . In the zero-range limit, i.e. for  $k^2|r_e| \ll |a^{-1} + \imath k|$  the scattering amplitude is solely characterized by the scattering length<sup>2</sup>. Furthermore, for  $r_e \ll 1/k$  and  $k|a| \gg 1$  the gas enters the *unitary* limit with  $f_{k_0} = \imath/k$ .

5) To further explain Feshbach-type resonance effects the atom-atom interaction is more specifically modeled as an interaction via two potential curves, a so-called open channel potential  $V_{\text{open}}(r)$  and a closed channel potential  $V_{\text{closed}}(r)$ . For alkali atoms with one valence electron,  $V_{\text{open}}(r)$  corresponds to the electronic triplet configuration and  $V_{\text{closed}}(r)$  to the spin singlet. A weak coupling between the two channels makes it possible that "incoming" atoms in the open channel are resonantly affected by closed channel bound states if the energy difference is sufficiently small. Due to the different magnetic moments of singlet and triplet states this energy difference can be tuned over a wide range, i.e. the scattering length can simply be adjusted by an external magnetic bias field.

### 4.1.2 A Fermi gas in the unitary limit

With the continuous tunability of the scattering length via a Feshbach resonance it is straightforward to prepare a Fermi gas in the unitary limit and study its behavior

---

<sup>1</sup>Note that  $-\text{Im}(z)/|z|^2 = \text{Im}(1/z)$  for any complex number  $z$ .

<sup>2</sup>Typical experiments with cold atoms in the vicinity of broad Feshbach resonances fulfill  $r_e \approx b$  and are therefore in the zero-range limit.

on both sides of the resonance. Despite all difficulties arising from the lack of an appropriate small parameter for  $k_F|a| \rightarrow \infty$  many theoretical studies<sup>3</sup> have developed a detailed quantitative understanding of the relevant many-body physics, but in this context it is more insightful to follow a qualitative model as described by Pricoupenko and Castin in [55].

Consider a homogeneous ultracold gas of  $N$  fermions of mass  $m$ , half of them in the spin-up  $\uparrow$  state, the other half in spin-down  $\downarrow$  configuration. Heuristically this many-body system is modeled by constructing a pseudo-equivalent two-body problem for each  $\uparrow$  atom such that the nearest  $\downarrow$  neighbor interaction is described via the standard<sup>4</sup> Fermi  $\delta$  pseudopotential

$$V(\mathbf{r}) = \frac{4\pi\hbar^2 a}{m} \delta(\mathbf{r}) \partial_r(r\cdot). \quad (4.4)$$

In a center-of-mass frame this scenario translates into a fictitious  $\uparrow$  particle of reduced mass  $m/2$  interacting with a fixed  $\delta$  scatterer at the origin. To mimic the Fermi statistical effect of the other  $\uparrow$  atoms a boundary condition is imposed so that the wave function  $\phi(\mathbf{r})$  of the fictitious particle vanishes on the surface of a sphere of radius  $R$ . The appropriate value for  $R$  can be obtained by comparing the total energy of the noninteracting gas  $E = (3/5) N\epsilon_F$  to the zero point energy  $\epsilon_0 = (\hbar^2\pi^2)/(mR^2)$  of the  $\uparrow$  atoms confined in spheres of radius  $R$ , i.e.  $E = \epsilon_0 N/2$ . This leads to

$$k_F R = \pi \sqrt{5/3}, \quad (4.5)$$

which is a sensible calibration for  $R$  given that  $k_F R$  should be of order 1 if  $R$  is the characteristic extent of a single atom volume.

---

<sup>3</sup>see [54] and references therein

<sup>4</sup>As discussed in the previous paragraph, the scattering problem is within certain limits sufficiently described by a scattering amplitude of form (4.3), i.e. any interaction potential leading to this scattering amplitude can be deployed to characterize the atom-atom scattering. The particular form of the regularized delta pseudopotential ensures mathematical ease. References [57, 58, 59] provide an in-depth discussion of various analogous model potentials.

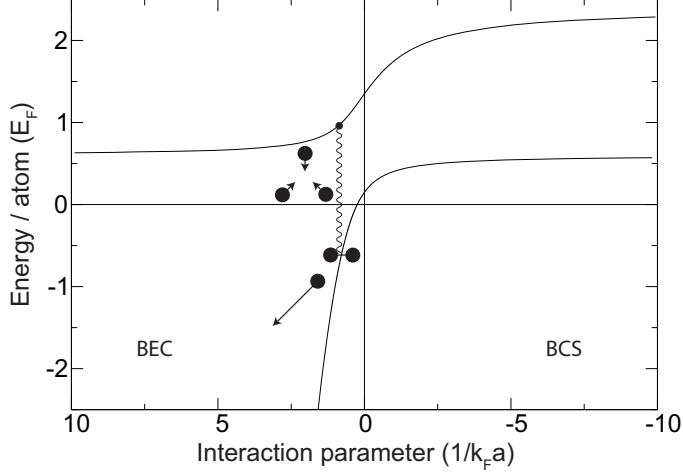


Figure 4-1: Energy spectrum of an interacting Fermi gas as derived from a simple two-body model. Only the two lowest-lying branches are shown. Three-body collisions depopulate the upper branch and lead to the formation of bound atom pairs. Adapted from [55].

To solve the so defined simple Fermi gas model it is advantageous to not directly insert the potential (4.4) into the Schrödinger equation. Instead, as shown in [59, 60] one can equivalently introduce the contact condition

$$\lim_{r \rightarrow 0} \frac{\partial_r(r\phi)}{r\phi} = -1/a \quad (4.6)$$

and start from the s-wave restricted free Schrödinger equation which is solved by the first spherical Bessel function so that its positive energy  $\epsilon = \hbar^2 k^2/m$  solutions scale like  $r\phi(r) \propto \sin k(r - R)$  and its negative energy  $\epsilon = -\hbar^2 \kappa^2/m$  solutions follow  $r\phi(r) \propto \sinh \kappa(r - R)$ . Imposing condition (4.6) on these solutions leads to

$$\tan kR = ka \quad \text{and} \quad \tanh \kappa R = \kappa a, \quad (4.7)$$

respectively. Together with equation (4.5) this determines the energy spectrum of the gas as depicted in Figure 4-1 for the two lowest-energy branches. In the limit

of weak interactions, i.e. for  $|1/(k_F a)| \gg 1$ , the total energy approaches the value  $E/N = (3/5) \epsilon_F$  as expected for the noninteracting gas. Concentrating on the ground state branch the model predicts two different regimes: Below the Feshbach resonance (for  $a > 0$ ) a two-body bound state emerges with binding energy  $-\hbar^2/(ma^2)$ . The atom pair extent is typically on the order of the scattering length  $a$ , and at low enough temperatures these bosonic dimers can form a Bose-Einstein condensate (BEC). In the opposite regime for  $a < 0$  the system becomes an attractive Fermi gas and a more detailed analysis expects for sufficiently low temperatures the transition to a superfluid BCS state [36, 61].

Right on the Feshbach resonance, i.e. for  $1/(k_F a) = 0$ , the model predicts no dramatic changes - a smooth transition connects the BCS side to the BEC limit and on resonance the total energy of the gas is smaller than for the noninteracting system indicating an effective attraction due to the atomic interactions. In the unitary limit of diverging scattering length and saturated scattering amplitude all relevant scales are set by the Fermi energy and derived quantities.

The second lowest branch in the energy spectrum plotted in Figure 4-1 corresponds for  $1/(k_F a) \rightarrow \infty$  to a weakly interacting repulsive Fermi gas. Not being in the ground-state the gas can decay via a three-body collision to the lowest branch by forming a dimer and ejecting a third atom carrying away the binding energy. This dimer production by decay from the metastable upper branch, the condensation of atom pairs to a Bose-Einstein condensate, the superfluidity of the unitary gas and the smooth crossover from a BCS state to the BEC limit have all been observed experimentally [62, 63, 64] and confirm the qualitative insight obtained from the simple toy model.

## 4.2 In-situ noise measurements - Advantages and challenges

Noise measurements in interacting quantum gases are complicated by the non-ballistic expansion of the gas when released from trap. Depending on the specific sample properties it is still possible to reconstruct insightful information from such measurements, but in general it is desirable to adapt the previous chapter's method to in-trap measurement scenarios. While an in-trap measurement has the obvious advantage of not requiring any further potentially destructive manipulation of the atom sample, it is accompanied by impractically high optical densities and various other resolution and depth of field constraints.

To address the problem of saturated high  $OD$  "blacked out" absorption images one can detune the imaging light frequency away from the atomic resonance so that the effective scattering cross section is reduced according to equation (3.5). However, such a detuning does not only reduce the optical attenuation, it gives simultaneously rise to dispersive effects as described by equation (3.6), i.e. the trapped atom cloud starts to act like an optical lens bending light rays away from the direction of incidence. For clouds significantly thinner than the imaging system's depth of field this effect can be tolerated, but if the cloud thickness becomes comparable to the axial resolution the additional "residual lens" in the imaging system will noticeably degrade the background normalization.

Instead of treating the dispersive response of the atoms as an unwanted side effect one can set up the imaging system such that dispersive phase shifts are turned into intensity contrast signals on the detector. Popular methods to achieve this contrast conversion are polarization contrast and phase contrast imaging as described below in more detail.

### 4.2.1 A short review of Fourier optics

To further understand the various contrast enhancement methods and related aspects of image formation it is instructive to review the basic concepts of Fourier optics.

Fourier optics is a continuation of the standard scalar wave theory of light<sup>5</sup>. In a given "input" plane  $z = z_0$  on the optical axis the complex amplitude  $U(x, y, z_0)$  of the light field of wavelength  $\lambda$  is Fourier decomposed into its plane wave superposition components

$$U(x, y, z_0) = \int \int F(\nu_x, \nu_y) \exp[-2\pi i(\nu_x x + \nu_y y)] \exp[-i k_z z_0] d\nu_x d\nu_y, \quad (4.8)$$

where  $k_z = \sqrt{k^2 - k_x^2 - k_y^2} = 2\pi\sqrt{\lambda^{-2} - \nu_x^2 - \nu_y^2}$  is the  $z$ -component of the wavevector  $\mathbf{k}$  with the corresponding spatial frequencies  $\nu_x$  and  $\nu_y$ . The key concept of Fourier optics is now to predict the complex amplitude at a later "output" plane  $z = z_1$  by individually propagating the plane waves through the optical system and then superposing them to the new complex amplitude field  $U(x, y, z_1)$ . Because wave equations are linear and the optical system is shift-invariant<sup>6</sup> one can apply all principles known from the general theory of linear systems. In particular it is advantageous to characterize the system by its transfer function  $\mathcal{H}(\nu_x, \nu_y)$ ; since an harmonic input function  $f_\nu(x, y)$  is expected to lead to an harmonic output function  $g_\nu(x, y) = \mathcal{H}(\nu_x, \nu_y) f_\nu(x, y)$  only modified by a frequency-dependent complex prefactor, the system is fully described by the explicit knowledge of  $\mathcal{H}(\nu_x, \nu_y)$ .

For instance, for the case of free space propagation from  $z = 0$  to  $z = d$  and assuming an harmonic input function  $f(x, y) = \exp[-i2\pi(\nu_x x + \nu_y y)] = \exp[-i(k_x x + k_y y + k_z 0)]$  one finds with  $k_z$  from above  $g(x, y) = \exp[-i(k_x x + k_y y + k_z d)]$  for the output function. Therefore the transfer function for free space propagation over a

---

<sup>5</sup>Many optical phenomena do not require the full vector formulation of the electromagnetic theory of light. It is often sufficient to introduce a complex scalar wavefunction whose modulus is proportional to the optical power density .

<sup>6</sup>Free space is invariant to displacement of the coordinate system.

distance  $d$  becomes

$$\mathcal{H}(\nu_x, \nu_y) = g/f = \exp[-i2\pi d(1/\lambda^2 - \nu_x^2 - \nu_y^2)^{1/2}]. \quad (4.9)$$

From this expression it is clear that for spatial frequencies fulfilling  $\nu_x^2 + \nu_y^2 \leq 1/\lambda^2$  the incoming plane wave continues along its travel direction simply accumulating the corresponding phase shift. However, for  $\nu_x^2 + \nu_y^2 > 1/\lambda^2$  the exponent in equation (4.9) is real<sup>7</sup> so that the traveling wave is attenuated during free space propagation thus becoming an evanescent wave. This quantitatively confirms the well-known conclusion that structure information finer than the wavelength  $\lambda$  cannot be transmitted beyond the near field.

Following the above example all components in an optical system can be assigned to a specific transfer function making it possible to propagate an incoming beam step by step through the system, not only providing a convenient procedure to analyze wave optics problems, but often delivering additional physical insight from aspects clearer seen in the frequency domain. An analysis of dispersive phase contrast imaging - to some extent a precursor of the later relevant speckle imaging - illustrates these benefits very well.

## 4.2.2 Dispersive imaging

For simplicity first consider a two-dimensional phase object<sup>8</sup> in the input plane of a  $4-f$  imaging system as depicted in Figure 4-2. The system forms a real inverted 1:1 image of the object in the output plane, however, a typical detector like a CCD camera or the naked eye will only be sensitive to intensity variations so that a pure phase object will stay invisible.

---

<sup>7</sup>In this context the negative square root  $(-|x|)^{1/2} = -i\sqrt{|x|}$  is chosen.

<sup>8</sup>An ideal phase object does not absorb any light, i.e. the imaginary part of its complex index of refraction is zero, it only disperses and refracts the light as discussed in the context of equation (3.4).

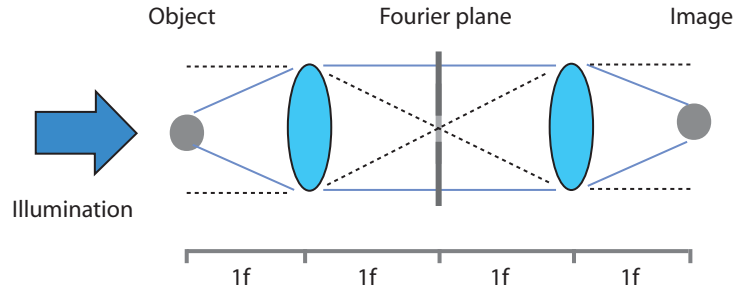


Figure 4-2: Layout of a  $4-f$  imaging system. Two imaging lenses of focal length  $f$  in infinite conjugate configuration spaced two focal lengths apart generate a 1:1 image of the input object in the output plane. Dotted lines represent rays of unscattered light modeling object illumination by a large diameter collimated beam. The solid blue lines trace rays of light scattered by the object. To obtain phase contrast images a  $\lambda/4$  phase plate is positioned in the Fourier plane so that shifted and not shifted light components interfere in the image plane with a relative phase shift of  $\pi/2$ .

### Phase contrast imaging

One possibility to enable intensity contrast for a phase object in the above imaging system is the introduction of a selective  $\lambda/4$  phase shift for the DC component in the spatial frequency spectrum of the light after passing through the atom sample. Experimentally this can be achieved with a so-called phase plate placed in the Fourier plane of the system. In a  $4-f$  imaging configuration the Fourier plane ( $2f$  away from the input plane) represents the optical Fourier transform<sup>9</sup> of the input plane's complex amplitude distribution. The phase plate behaves essentially like a flat piece of optical glass, only that a small round region of typically a few hundred microns diameter in its center is slightly modified so that the optical path length there is reduced or advanced by  $\lambda/4$ . Downstream in the image plane this leads to a situation where recombined rays of phase shifted and unshifted light interfere with a corresponding

<sup>9</sup>This can be seen by systematically propagating the incoming light through free space and the first lens, but it is also made clear by considering how ray angles (i.e. wave vectors) are mapped to points on the Fourier plane by the first lens.

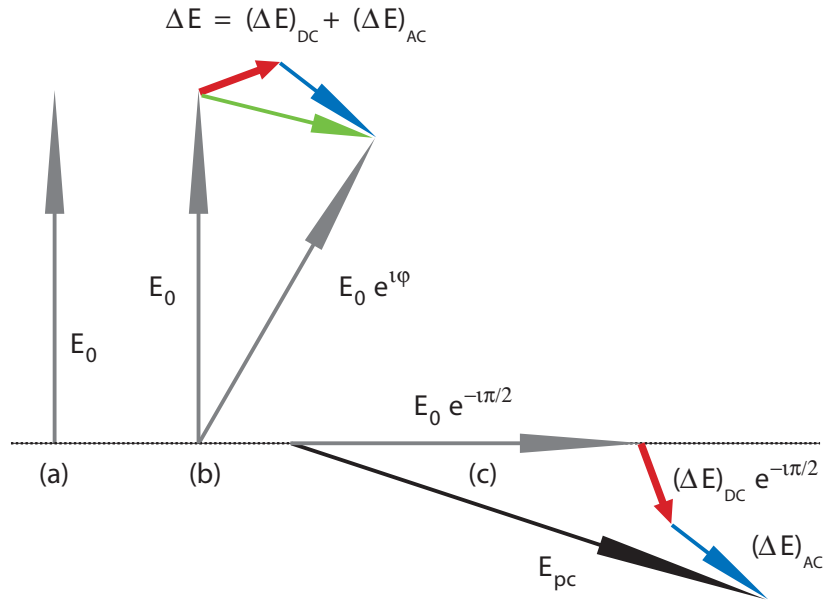


Figure 4-3: Complex amplitude phasor diagram for phase contrast imaging. (a) The illuminating light field is represented by an upright phasor  $\mathbf{E}_0$  in the output plane. (b) A pure phase object rotates the complex amplitude by an angle  $\varphi$ . (c) Insertion of a  $\lambda/4$  phase plate in the Fourier plane causes a selective  $\pi/2$  phase shift for the spatial DC components of the light. This effectively changes the length of the resulting output phasor  $\mathbf{E}_{pc}$ , turning the phase modulation in the object plane into an intensity modulation in the image plane. Since phase contrast imaging is achieved via a selective manipulation in the Fourier spectrum it critically relies on the separation of spatial frequency scales for illumination and object structure. Different colors group arrows of the same lengths.

phase difference of  $\pi/2$ . Figure 4-3 further illustrates this with a phasor diagram showing the complex amplitude (mappable to electric field components) on the optical axis in the image plane for three different configurations. In case (a) the input plane is empty and no phase plate is in the system so that the upright input phasor  $\mathbf{E}_0$  is simply reproduced at the output plane<sup>10</sup>.

Adding a pure phase object (i.e. no intensity attenuation) in the input plane causes a relative rotation of the output phasor by an angle  $\varphi$  as depicted in (b). To later anticipate the effect of a phase plate it is helpful to decompose the rotated phasor into

<sup>10</sup>This corresponds to the very definition of an imaging system: Rays from a point source in the input plane are overlapped on a corresponding point in the output plane all having traveled the same optical path length.

an unaltered  $\mathbf{E}_0$  and an additional  $\Delta\mathbf{E}$  component (green arrow in Figure 4-3).  $\Delta\mathbf{E}$  is then further decomposed into a DC / low spatial frequency component  $(\Delta\mathbf{E})_{\text{DC}}$  and a high frequency component  $(\Delta\mathbf{E})_{\text{AC}}$ . This distinction is important because the phase plate in the Fourier plane will affect these two components differently. Accordingly a critical spatial frequency  $\nu_{\text{DCAC}}$  exists that marks the transition between the two intervals. Higher spatial frequencies are in the Fourier plane located further away from the optical axis (on which the phase spot is centered) and therefore the size of the phase spot determines  $\nu_{\text{DCAC}}$  for a given lens system.

In practice the phase spot size is chosen such that it fully covers the (in the Fourier plane refocused) unscattered illumination light, which means that upon insertion of the phase plate the  $\mathbf{E}_0$  and  $(\Delta\mathbf{E})_{\text{DC}}$  phasor components are being rotated by  $\pi/2$ , whereas  $(\Delta\mathbf{E})_{\text{AC}}$  stays unaffected, as shown in Figure 4-3 (c). Overall the total phase contrast complex amplitude in the output plane is then given by the phasor sum

$$\mathbf{E}_{\text{pc}} = \mathbf{E}_0 e^{-i\pi/2} + (\Delta\mathbf{E})_{\text{DC}} e^{-i\pi/2} + (\Delta\mathbf{E})_{\text{AC}}, \quad (4.10)$$

i.e. the "invisible" phase shift  $\varphi$  has been turned into a phasor length change meaning an intensity signal in the image plane.

By introducing an appropriate absorption prefactor the discussion so far can easily be extended to include objects with a mixed dispersive and absorptive response. This applies in particular to the case of two-level atom gas clouds as described in the context of equation (3.4).

### 4.2.3 Initial experimental strategy

Given the above considerations it appeared promising to realize noise measurements for trapped quantum gases via the experimental implementation of phase contrast imaging. The state  $|1\rangle$  &  $|2\rangle$  balanced spin mixture of  ${}^6\text{Li}$  is for this method especially well suited because the optical absorption resonance for the two states is

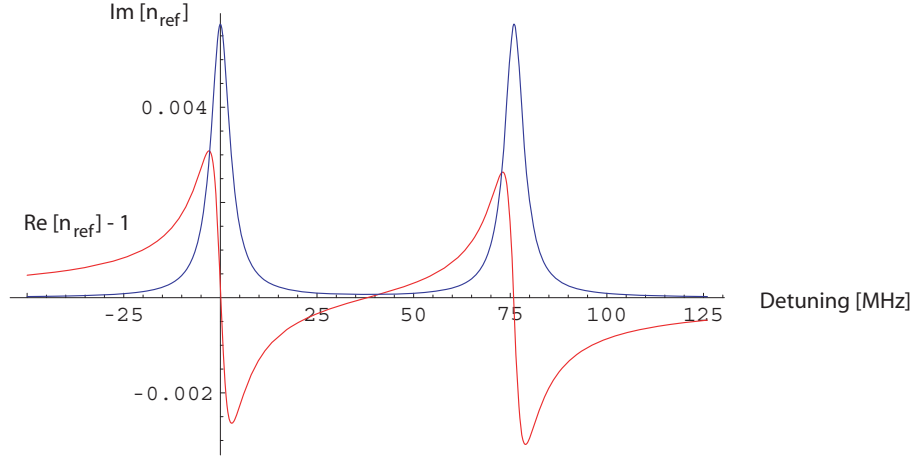


Figure 4-4: Real (red curve) and imaginary part (blue curve) of the index of refraction  $n_{\text{ref}}$  of a noninteracting balanced  ${}^6\text{Li}$  state  $|1\rangle$  &  $|2\rangle$  Fermi gas mixture as a function of the probe laser detuning (with respect to the state  $|2\rangle$  cycling resonance). Linewidths and relative detuning of the two transitions match favorably so that laser light centered between the resonances experiences no mean dispersion but becomes sensitive to the relative number deviation of the two spin states. The plotted curves are derived from equation (3.4) and assume typical shallow trap spin state densities of  $n = 5 \times 10^{17} \text{ m}^{-3}$  corresponding to a Fermi energy  $E_F = h \times 8.2 \text{ kHz}$ .

roughly separated by 76 MHz at higher magnetic fields so that laser light<sup>11</sup> parked at the center frequency between the two resonances will not experience a mean dispersion (red and blue phase shift effects from the two states cancel each other) and only weak absorption (equal amounts from both states) as illustrated in Figure 4-4. Neutral average dispersion is a significant advantage in several regards: First, offset-free measurements are typically cleaner and more precise compared to fluctuation measurements on top of large mean values. Second, since state  $|1\rangle$  and  $|2\rangle$  atoms cause opposite phase shifts not only the mean phase shift is zero, but the phase contrast signal will also be differential, i.e. directly access  $\Delta(n_1 - n_2)$  with  $n_1$  and  $n_2$  being the implicit individual spin component densities. Third, even a thicker (i.e. partially out of focus) gas cloud will not introduce the earlier mentioned "residual lens" effect, which could otherwise cause severe background normalization issues. Furthermore, all types of dispersive imaging have the detuning-dependent advantage that they allow

<sup>11</sup>The D2 transition of  ${}^6\text{Li}$  has a width of  $\Gamma = 2\pi \times 5.9 \text{ MHz}$ , i.e. the symmetric 38 MHz intervals correspond to a detuning of about 6 natural linewidths. Also see Figure 3-8.

for higher illumination intensities (at constant Rayleigh scattering rates, cf. equation (3.16)) compared to resonant absorption imaging.

However, experimental testing of the above considerations led to rather surprising results with the main finding that symmetrically detuned noise measurements on trapped balanced noninteracting Fermi gas mixtures resulted in very similar noise values, whether performed as simple off-resonant absorption measurements (without a phase plate) or as phase contrast measurements (with a phase plate). Following the previous chapter's procedure it turned out that the measured amount of noise exceeded the expectation for absorption images (even when assuming full Poisson noise) by more than a factor of ten. On the other hand the measured noise values roughly corresponded to the anticipated phase contrast signal and hence it seemed as if there was a hidden contrast enhancement mechanism contributing to the nominally pure absorption signal. Further investigation eventually revealed that a phenomenon conceptually similar to laser speckle plays a key role when trying to understand the experimental observations. The next paragraph will therefore provide a short review of speckle phenomena in optics before explaining concrete details of "speckle imaging".

## **4.3 From laser speckle to speckle imaging**

### **4.3.1 Laser speckle**

With the advent of coherent laser light speckle phenomena became ubiquitous side effects in optical experiments. As such, speckle is often considered a hindrance and not a feature. The well-known prototype laser speckle manifestation, the granular appearance of a laser beam when observed on an index card (see Figure 3-9 (A)), illustrates the most important properties of laser speckle very well. First of all, speckle formation appears to require the illumination of a microscopically chaotic and unordered optically rough object (paper, ground glass etc. are rough on the scale of an optical wavelength) with a highly coherent light source. Accordingly, a statistical description is necessary in order to properly model and explain speckle

patterns.

Assuming an imaging geometry as depicted in Figure 4-2 (without phase plate), consider a coherently illuminated optically rough object in the input plane. One can qualitatively understand speckle formation in the image plane as a result of the random superposition of many individual point spread functions (PSFs) with different phases [48, 65]. More precisely, the light irradiance at a given point  $P'$  in the image plane is geometrically mapped to the appropriate point  $P$  in the object plane, but due to the finite aperture and resolution of the imaging system (with a correspondingly sized PSF), light of different phases from points close to  $P$  will partially also contribute to the irradiance at  $P'$ . This overlap of randomly phased PSFs around  $P'$  gives rise to irregular interference patterns also known as speckle patterns.

From this explanation it is clear that for the case of a focused imaging geometry the object needs to exhibit phase ripples (with phase excursions exceeding  $2\pi$  for full contrast) on length scales well beyond the resolution limit in order to cause speckled intensity fluctuations in the image plane - larger size phase fluctuations do not lead to intensity contrast because they do not generate overlapping PSFs of different phases. Furthermore this also implies that the scale size of the granularity in the speckle pattern is cut off at a length scale corresponding to the numerical aperture of the imaging system.

### 4.3.2 Out-of-focus speckle

Instead of relying on the overlap of out-of-phase PSFs by means of their finite widths as explained in the previous paragraph it is alternatively possible to achieve an analogous overlap by intentionally defocusing the imaging system as illustrated in the cartoon drawing in Figure 4-5. Assuming a thin homogeneously illuminated pure phase object with low-frequency phase fluctuations (i.e. only on resolved length scales) one expects that an in-focus imaging setup will produce a flat output image without visible intensity ripple (upper illustration in Figure 4-5). However, once the system is defocused the imaging condition is not fulfilled anymore, i.e. light rays of different optical path lengths are combined on the image plane so that the phase fluctuations

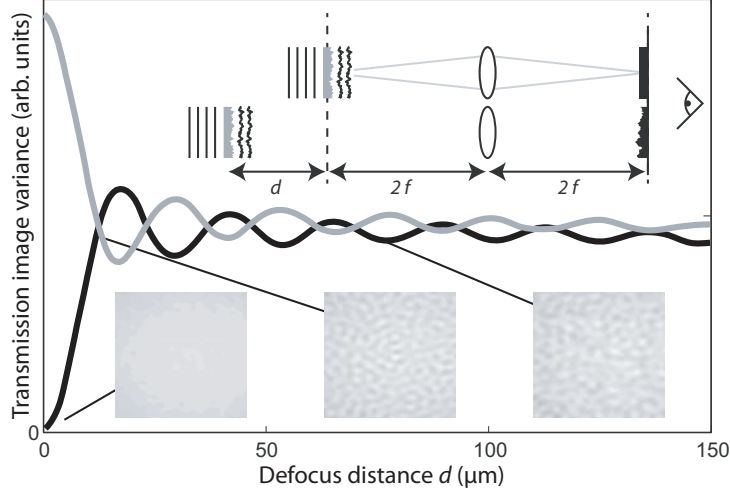


Figure 4-5: Simulation of propagation effects after light has passed through a Poissonian phase noise object. Shown are the variance measured in the amplitude (black line) and the phase (gray line) as a function of defocus distance, for an imaging system with a numerical aperture of 0.14. Within a distance less than 5% of the cloud size, noise becomes equally distributed between the two quantities and the variances in absorption and phase-contrast images become the same. (Top inset) For low-frequency phase fluctuations, an in-focus phase noise object gives no amplitude contrast, but when moved out of focus it does. (Bottom inset) Sample intensity patterns for a defocused phase object.

are turned into intensity fluctuations (lower illustration).

This out-of-focus speckle generation is the key mechanism to understand the above mentioned surprisingly high noise values found for the detuned absorption images. Unlike for the time-of-flight measurements in the noninteracting gas, the depth of field at the necessary lateral resolution does typically not cover the axial extent of the trapped atom cloud. For instance, the measurements reported on later in this chapter were carried out with a depth of field Rayleigh range of  $8 \mu\text{m}$  while the extent of the cloud along the imaging direction was  $135 \mu\text{m}$ . This means that the sample thickness ensured contrast conversion, or in other words, sufficient defocusing acts like a phase plate, mapping phase fluctuations to intensity fluctuations. Quantitatively it turns out that this defocus-induced redistribution of phase and amplitude noise

happens over distances on the order of the imaging depth of field as illustrated by the simulations in Figure 4-5. Reference [66] provides further details about these Fourier optics based computer simulations and reference [48] contains extensive discussions about other aspects of speckle physics.

Among the many relevant features and properties of out-of-focus speckle the following three are most important for a later image analysis:

1. Phase and amplitude noise equilibrate 1:1 after a short propagation distance corresponding to the depth of field of the imaging system.
2. Small phase-excursion speckle  $OD$  noise is additive; assuming a balanced spin mixture and symmetric detuning the speckle  $OD$  variance signal is proportional to  $\Delta(N_1 - N_2)$  in the corresponding pixel column region.
3. Non-symmetric imaging light detunings can be used to probe a correspondingly different linear combination of  $N_1$  and  $N_2$  fluctuations. However, this is typically accompanied by more pronounced background normalization imperfections.

Since the numerically exact relation between imaging signal and atom number fluctuations is for speckle images not as straightforwardly derived as in the previous chapter for standard absorption images, it is helpful to experimentally calibrate the speckle noise data by first performing measurements on a noninteracting gas with known outcome.

## 4.4 Data acquisition and analysis

### 4.4.1 Experimental setup and sample preparation

The above discussion made clear that speckle imaging does not require any specialized optics infrastructure. Hence the employed imaging setup is very similar to the one described in Figure 3-5 with the only difference that the second stage magnification is chosen to be 1:5 instead of 1:2 leading to an overall magnification by a factor 10

which is a necessary adaption to the higher densities and smaller dimensions of the trapped atom samples.

The experiments were performed with typically  $10^6$   ${}^6\text{Li}$  atoms in each of the two lowest hyperfine states  $|1\rangle$  and  $|2\rangle$  confined in an optical dipole trap oriented at 45 degrees to the imaging axis with radial and axial trap frequencies  $\omega_r = 2\pi \times 108.9(6)$   $\text{s}^{-1}$  and  $\omega_z = 2\pi \times 7.75(3)$   $\text{s}^{-1}$ , corresponding to spin state densities of  $n = 5 \times 10^{17}$   $\text{m}^{-3}$  and a Fermi energy  $E_F = h \times 8.2$  kHz. This particular geometry made it possible to easily check and confirm that the speckle noise technique delivers robust results insensitive against variations of the defocus distance: The left and right wings of the elongated cloud are further out of focus but constraining the analysis to these regions delivers similar amounts of noise compared to the central part of the atom cloud.

For the samples imaged at 527 G, the sample preparation was analogous to that described in chapter 3, with a temperature of  $0.14(1) T_F$ . The samples imaged at other magnetic fields were prepared in a similar fashion, except that evaporation was performed at 1000 G (BCS side of the crossover) to a final temperature of  $T = 0.13(1) T_F$  before ramping the magnetic field over 1.5 s to its final value (adiabatically following the lowest branch). The temperature at 1000 G was determined by fitting a noninteracting Thomas-Fermi distribution in time of flight. The temperatures at other points in the crossover were related to that value assuming an isentropic ramp, using thermodynamic calculations presented in [67]. Using this method temperatures were found to be  $0.13(1) T_F$  at 915 G,  $0.19(1) T_F$  at 830 G, and  $0.19(3) T_F$  at 790 G where additional evaporation was performed to achieve a central optical density similar to that at the other magnetic fields. The extent of the cloud along the imaging direction was  $135 \mu\text{m}$ , much larger than the Rayleigh range of  $8 \mu\text{m}$  for the imaging system with a NA of 0.14 and quadratic resolution elements measuring  $2.6 \mu\text{m}$ .

#### 4.4.2 Noise extraction and mapping procedure

The goal of the noise measurements in interacting Fermi gases<sup>12</sup> is to determine at various interaction strengths the normalized susceptibility  $\tilde{\chi} = \chi/\chi_0$  and compress-

---

<sup>12</sup>See chapter 2 for a short theoretical introduction.

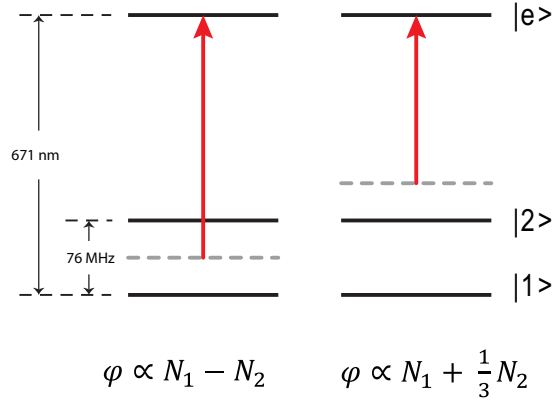


Figure 4-6: Two different imaging light detunings are used to access fluctuations in  $(n_1 - n_2)$  and  $(n_1/3 + n_2)$ . The excited state  $|e\rangle$  corresponds to the  $m_J = -3/2$  manifold as depicted in Figure 3-8.

ibility  $\tilde{\kappa} = \kappa/\kappa_0$ , where  $\chi_0 = 3n/(2E_F)$  and  $\kappa_0 = 3/(2nE_F)$  are the susceptibility and compressibility of a zero-temperature non interacting Fermi gas with the same total density  $n$  and Fermi energy  $E_F$ .

As previously described, for different choices of the probe light frequency, the two atomic spin states will have different real polarizabilities and the local refractive index will be a different linear combination of the (line-of-sight integrated) column densities  $n_1$  and  $n_2$ . To measure the susceptibility a probe light frequency exactly between the resonances for states  $|1\rangle$  and  $|2\rangle$  was chosen, so that the real polarizabilities are opposite and the refractive index is proportional to the magnetization  $(n_1 - n_2)$ . The intensity fluctuations on the detector after propagation are consequently proportional to the fluctuations in magnetization. Since a refractive index proportional to  $(n_1 + n_2)$  occurs only in the limit of infinite detuning, fluctuations in the total density are measured by exploiting the fact that these fluctuations can be inferred from the fluctuations in two different linear combinations of  $n_1$  and  $n_2$ . For convenience, the second linear combination is obtained using a detuning that has the same value, but opposite sign for state  $|2\rangle$ , and therefore three times the value for state  $|1\rangle$  as shown in Figure 4-6. Because the dispersive signal scales inversely proportional to the detuning, images of the fluctuations in  $(n_1/3 + n_2)$  are recorded with this imaging frequency.

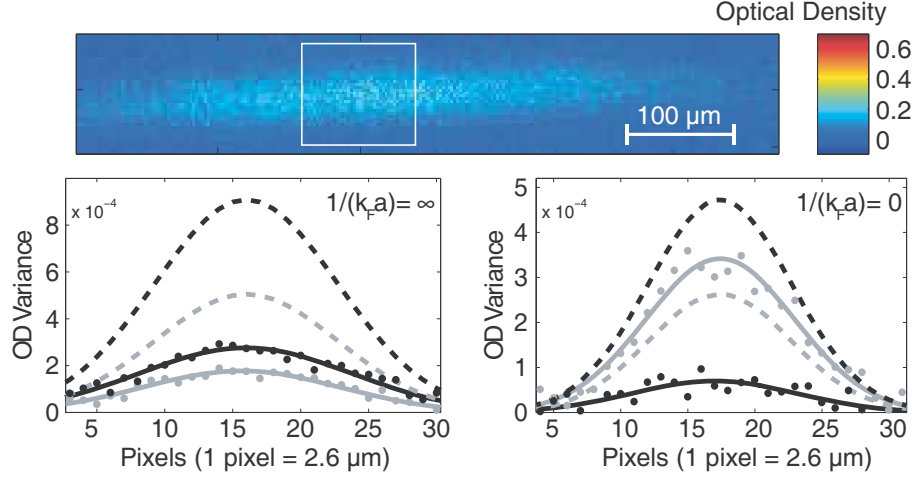


Figure 4-7: (Top) Example speckle noise image, with white box indicating analysis region. (Bottom) Noise data for noninteracting (left) and resonantly interacting (right) cold clouds, showing  $\Delta_-^2$  (black dots) and  $\Delta_+^2$  (gray dots). Solid lines are Gaussian fits to the data, and dotted lines illustrate the expected full Poissonian noise for the corresponding quantities based on density determined from off-resonant absorption.

The noise analysis procedure was nearly identical to that performed for the expanded gas (see chapter 3). A high-pass filter with a cutoff wavelength of  $13 \mu\text{m}$  was applied to each image of the cloud to minimize the effect of fluctuations in total atom number. Then, for each pixel position, the variance of the optical densities at that position in the different images was computed. After the subtraction of the contribution of photon shot noise, the resulting variance image reflects the noise contribution from the atoms.

To calibrate the speckle method, fluctuation measurements were performed in a noninteracting mixture, realized at a magnetic field of 527 G where the scattering length between the two states vanishes. Figure 4-7 shows raw profiles of the  $OD$  variances  $\Delta_-^2$  and  $\Delta_+^2$  measured at the two detunings. These fluctuations in the speckle pattern are proportional to number fluctuations in the probe volume  $V$ :

$$\Delta_-^2 = (c \Delta(N_1 - N_2))^2 \quad \text{and} \quad \Delta_+^2 = (c' \Delta(N_1/3 + N_2))^2. \quad (4.11)$$

In these relations  $c$  and  $c'$  are the factors which have to be calibrated. Without interactions,  $N_1$  and  $N_2$  are uncorrelated, and one predicts

$$\frac{(\Delta(N_1 - N_2))^2}{(\Delta(N_1/3 + N_2))^2} = 1.8 \quad (4.12)$$

The observed ratio of  $\Delta_-^2/\Delta_+^2 = 1.56(14)$  reflects excess noise contributing to  $\Delta_+^2$  due to residual systematic dispersive effects and is accounted for by setting  $c'/c = \sqrt{1.8/1.56}$ . For high temperatures, the atomic noise of the non-interacting gas approaches shot noise, for lower temperatures a reduction in noise due to Pauli blocking in analogy to the findings of chapter 3 is observed.

The fluctuation-response theorem connects the two variances  $(\Delta(N_1 - N_2))^2$  and  $(\Delta(N_1 + N_2))^2$  to the normalized susceptibility  $\tilde{\chi}$  and compressibility  $\tilde{\kappa}$  via

$$(\Delta(N_1 - N_2))^2 = \frac{3N}{2} (T/T_F) \tilde{\chi} \quad \text{and} \quad (\Delta(N_1 + N_2))^2 = \frac{3N}{2} (T/T_F) \tilde{\kappa} \quad (4.13)$$

with  $N = N_1 + N_2$ . Recomposing the variances from the two experimentally accessible linear combinations these relations become

$$\frac{\Delta_-^2}{Nc^2} = 3/2 (T/T_F) \tilde{\chi} \quad \text{and} \quad 9/4 \frac{\Delta_+^2}{Nc'^2} - 1/4 \frac{\Delta_-^2}{Nc^2} = 3/2 (T/T_F) \tilde{\kappa}. \quad (4.14)$$

The constants  $c$  and  $c'$  are determined using the noise measurements at 527 G for a noninteracting Fermi gas for which  $\tilde{\chi} = \tilde{\kappa} = 1 + \mathcal{O}((T/T_F)^2)$ . Line-of-sight integration corrections are ignored in this analysis.

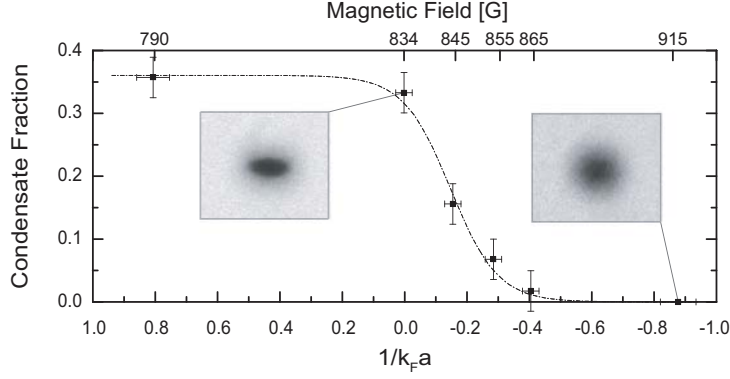


Figure 4-8: Measured condensate fraction as a function of dimensionless interaction strength  $1/(k_F a)$ . Insets show typical images from which the condensate fraction was extracted by fitting a bimodal distribution. The dashed line is a sigmoidal fit to guide the eye.

#### 4.4.3 Determination of the superfluid to normal phase boundary

As discussed earlier a quantum gas in the BEC-BCS crossover is expected to undergo at sufficiently low temperatures a phase transition between a normal and a superfluid state. For the later interpretation of the noise measurement results it is helpful to know where exactly this transition occurs. Therefore the phase boundary was experimentally determined via the standard technique of molecular condensate fraction measurements [63, 68] using magnetic field sweeps. For this, the magnetic field was rapidly switched to 570 G to transfer atom pairs to more deeply bound pairs (molecules) which survive ballistic expansion. For resonant imaging of the molecules, the field was ramped back to 790 G over 10 ms. The condensate fraction was determined by fitting the one-dimensional density profiles with a bimodal distribution yielding the results presented in Figure 4-8. For the given experimental conditions a significant superfluid fraction is found in direct vicinity of the Feshbach resonance and further down on the BEC side as expected for the temperatures reported above [36].

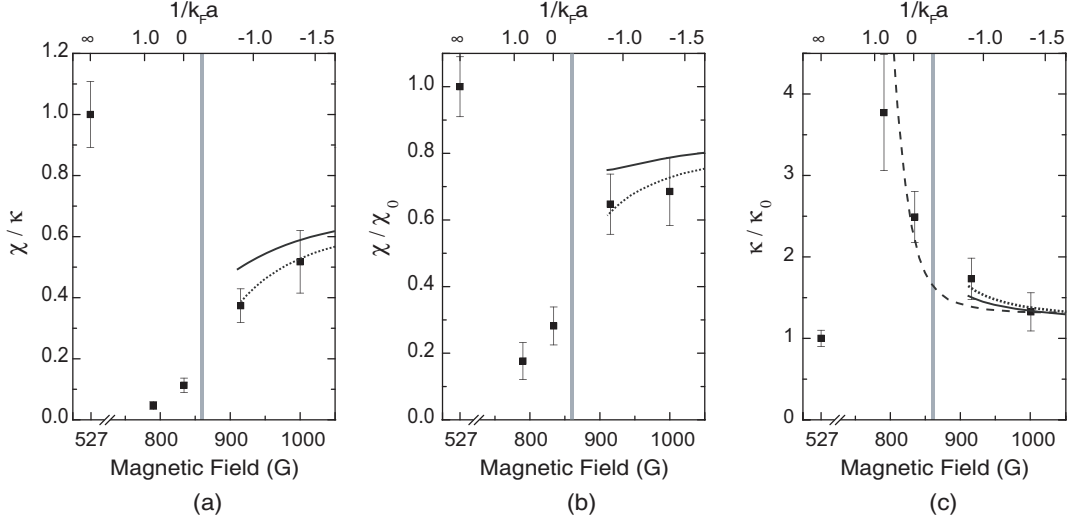


Figure 4-9: (a) The ratio  $\chi/\kappa$ , (b) the normalized susceptibility  $\chi/\chi_0$ , and (c) the normalized compressibility  $\kappa/\kappa_0$  in the BEC-BCS crossover. The variances derived from sequences of images are converted into thermodynamic variables using the measured temperatures and a calibration factor determined from the noninteracting gas. The vertical line indicates the onset region of superfluidity, as determined via condensate fraction measurements. The curves show theoretical zero temperature estimates based on 1st (dotted) and 2nd order (solid) perturbative formulas obtained from Landau’s Fermi-liquid theory integrated along the line of sight, and results from a Monte Carlo calculation (dashed) for the compressibility in a homogeneous system [69].

## 4.5 Results and interpretation

Applying the above noise analysis procedure to the data series taken at various interaction strengths along the BEC-BCS crossover leads to the susceptibility and compressibility results displayed in Figure 4-9. The measurements reproduce the expected qualitative behavior: For the sample at unitarity (834 G), where the transition temperature is sufficiently high that a sizable portion of the sample is superfluid, and for the sample on the BEC side, the spin susceptibility is strongly suppressed relative to the compressibility. This reflects the fact that the atoms form bound molecules or generalized Cooper pairs; the spin susceptibility should be exponentially small in the binding energy, while the enhanced compressibility reflects the bosonic character of the molecular condensate. At 915G and 1000G, where the sample is above the superfluid critical temperature, the susceptibility is larger but still below its value

for the noninteracting gas, reflecting the persistence of pair correlations even in the normal phase of the gas.

Above the Feshbach resonance, for attractive interactions, the results are compared to first and second order perturbation theory in the small parameter  $k_F a$ . This ignores the instability to the superfluid BCS state at exponentially small temperatures. The perturbation theory is formulated for the Landau parameters for a Fermi liquid [35, 33] as theoretically discussed in the context of equation (2.27). Although the experimental data are taken for relatively strong interactions outside the range of validity for a perturbative description, the predictions still capture the trends observed in the normal phase above the Feshbach resonance. This shows that more accurate measurements of the susceptibility, and a careful study of its temperature dependence, are required to reveal the presence of a possible pseudogap phase as proposed in [67].

This analysis neglects the small probe volume quantum fluctuations derived in equation (2.26) which are present even at zero temperature. For fluctuations of the total density, their relative contribution is roughly  $N^{-1/3}/(T/T_F)$ . Attractive interactions and pairing suppress both the thermal and quantum spin fluctuations, but it remains to be further investigated at what temperature quantum fluctuations become essential.

Spin susceptibilities could be alternatively obtained from the equation of state which can be determined by analyzing the average density profiles of imbalanced mixtures [5]. The speckle method has the advantage of being applicable without imbalance, and requires only local thermal equilibrium. Moreover, fluctuations can be compared with susceptibilities determined from the equation of state to perform absolute, model-independent thermometry for strongly interacting systems [70].

In conclusion, this chapter has demonstrated speckle imaging as a new technique to determine spin susceptibilities of ultracold atomic gases. The technique has been validated and calibrated using an ideal Fermi gas and was then applied to a strongly interacting Fermi gas in the BEC-BCS crossover. Being an in-situ method speckle imaging is directly applicable to studying pairing and magnetic ordering of

two-component gases in optical lattices. Even without quantitative refinements it is well suited to diagnose the onset of phase transitions that are accompanied by the development of spatial correlations as demonstrated in the next chapter.

# Chapter 5

## Exploring correlations in a repulsively interacting Fermi gas

*This chapter focuses on the experiment reported in the following publication: C. Sanner, E. J. Su, W. Huang, A. Keshet, J. Gillen, and W. Ketterle, “Correlations and Pair Formation in a Repulsively Interacting Fermi Gas”. Included in Appendix C.*

While the previous two chapters were mainly concerned with the development and proof-of-principle demonstration of new noise measurement techniques, this chapter reports on an application of these techniques to diagnose a ferromagnetic phase transition in a repulsively interacting Fermi gas. Accordingly, special emphasis is given to the relevant features and advantages of noise measurements in this context, whereas theoretical background information and other experimental aspects are just briefly touched upon or referenced to.

### 5.1 Ferromagnetic instability of a repulsive Fermi gas

Consider a repulsively interacting balanced Fermi gas mixture as already introduced in the discussion of Figure 4-1. Neglecting the decay from the repulsive branch to the

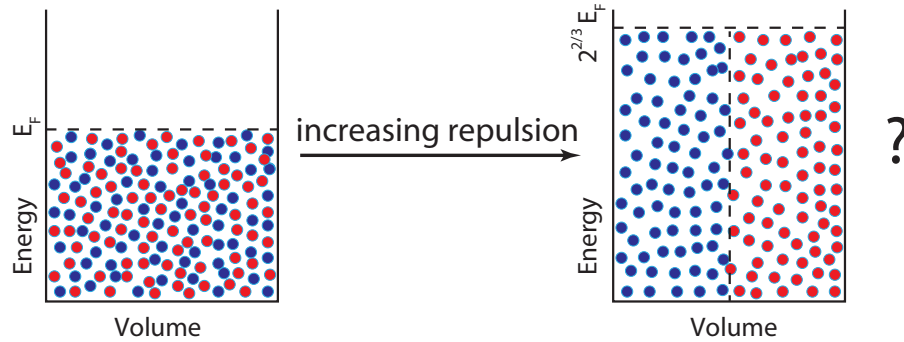


Figure 5-1: Schematic diagram illustrating the hypothetical repulsion-induced ferromagnetic transition from two overlapped noninteracting Fermi seas each with Fermi energy  $E_F$  to two fully developed macroscopic spin domains. For the case of a noninteracting homogeneous gas in a given volume  $V$  the Fermi energy scales as  $E_F \propto (N/V)^{2/3}$  and accordingly the two domains correspond to separate Fermi seas with Fermi energies  $2^{2/3} E_F$ .

lowest-lying energy branch, it is interesting to speculate about the system's behavior under increasing interaction strengths. Two intuitive scenarios seem possible: Due to the increasing repulsion the system builds up strong local anticorrelations between the two spin components but no long range order is established. Or alternatively, spin domains are formed so that the increase in repulsion energy is limited to small regions at the domain boundaries, but at the same time the Fermi pressure within the domains is higher, i.e. the total kinetic energy is increased as sketched in Figure 5-1.

Not surprisingly, this problem or rather an analogous solid state model considering electron bands has been extensively studied in the theoretical literature, where it is known as the Stoner model of ferromagnetism [71]. While the exact application of this model to typical magnetic materials with their complex electronic structure is challenging [72], it turns out that the Stoner Hamiltonian with its assumption of a zero-range repulsion between fermions of opposite spin is very well reproduced in the case of repulsively interacting ultracold neutral fermions. This motivated Jo et al. [25] to experimentally investigate the system and search for a ferromagnetic phase as predicted by the Stoner model. Although they found certain hints and indications supporting the assumption of a ferromagnetic state, it was not possible to obtain direct evidence for ferromagnetic domains. The reported findings of suppressed

inelastic three-body collisions<sup>1</sup> and of a minimum of the kinetic energy immediately followed by a steep rise (above a critical interaction value, cf. Figure 5-1) were rather unspecific signatures - in particular when dealing with metastable and not fully equilibrated samples. Given this situation speckle imaging appeared as the ideal experimental method to reliably identify and quantify spatial domains: As explained below in more detail the formation of spin domains of  $m$  atoms must be accompanied by an increase of the spin density variance by the same factor, which could be easily diagnosed via speckle imaging.

A lot of theoretical effort [73, 74, 75, 76, 77, 78, 79, 80, 81, 82, 83, 84, 85] has been invested to further understand Stoner-type ferromagnetism, and in particular the experimental results from reference [25] triggered many additional studies and numerical Monte Carlo simulations [86, 87].

### 5.1.1 The critical interaction strength

One key question for the experimental observation of the phase transition is the approximate localization of the critical interaction strength  $(k_F a)_c$  for domain formation. Most of the above referenced theoretical approaches find with some scatter a critical interaction parameter around  $(k_F a)_c = 1$  and simple zero temperature mean-field models arrive at similar results. For instance, with the ansatz [25]

$$E = 2VnE_F \frac{3}{10} [(1 + \eta)^{5/3} + (1 - \eta)^{5/3}] + 2VnE_F \frac{2}{3\pi} k_F a (1 + \eta)(1 - \eta) \quad (5.1)$$

for the total energy  $E$  of a two-component Fermi gas of average spin component density  $n$  and magnetization  $\eta = (n_1 - n_2)/(n_1 + n_2)$  it is clear that it becomes at larger scattering lengths  $a$  preferable to avoid interaction energy (second term) at the cost of increased kinetic energy (first term). In other words, the phase transition

---

<sup>1</sup>In order to form molecules, three fermions with opposite pseudospin would need to be close together which is increasingly unlikely when the system is arranged in polarized spin clusters.

should occur when the minimum in total energy is found at nonzero magnetization which happens for this model at  $k_F a > \pi/2$ . Alternatively, the same result is obtained when extending Landau's Fermi liquid theory [33] beyond the perturbative limit by examining the large  $k_F a$  behavior of the from equation (2.27) derived inverse susceptibility

$$\frac{\chi_0}{\chi} = 1 - \frac{2}{\pi} k_F a - \frac{16(2 + \ln 2)}{15\pi^2} (k_F a)^2. \quad (5.2)$$

To first order  $\chi$  diverges at  $(k_F a)_c = \pi/2 = 1.57$  and the second-order expansion suggests  $(k_F a)_c = 1.05$ .

### 5.1.2 Pairing instability vs. ferromagnetic instability

The Stoner model assumes a two-component Fermi gas with a repulsive short-range interaction described by a single parameter, the scattering length. The predicted phase transition to a ferromagnetic state requires large repulsive positive scattering lengths on the order of the interatomic spacing, but strong repulsive short-range interactions cannot be realized by purely *repulsive* forces. For instance, a repulsive square well potential is characterized by a positive scattering length  $a$  smaller than or equal to the barrier radius. Strong interactions with  $k_F a \geq 1$  require this radius to be comparable to the Fermi wavelength  $\lambda_F = 2\pi/k_F$  and are no longer short range<sup>2</sup>. On the other hand arbitrarily large repulsive positive scattering lengths can be realized by short-range *attractive* potentials with a loosely bound state with binding energy  $\hbar^2/(ma^2)$ ,  $m$  being the atomic mass.

However, the repulsive gas is then by necessity only metastable with respect to decay into the bound state, as shown schematically in Figure 4-1. Most theoretical studies of a Fermi gas with strong short-range repulsive interactions assume that the

---

<sup>2</sup>More generally, potentials with a positive scattering length  $a$  are bound state free only if the effective range  $r_e$  is larger than  $a/2$ . Otherwise, the in equation (4.3) introduced s-wave scattering amplitude  $f(k) = -1/(a^{-1} + ik - k^2 r_e/2)$  has a pole on the imaginary axis corresponding to a bound state.

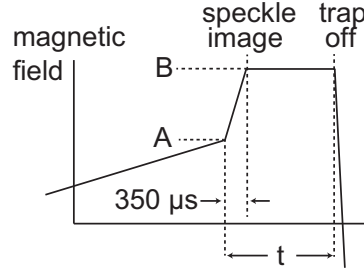


Figure 5-2: Timing diagram of the experiment. A rapid magnetic field change is employed to quickly jump from a weakly interacting Fermi gas (A) to a strongly interacting one (B). The evolution of correlations and domains and the molecule formation (population of the lower branch) are studied as a function of hold time  $t$ .

metastable state is sufficiently long-lived, and in recent Monte-Carlo simulations, the paired state is projected out in the time evolution of the system [86, 87]. In contrast, reference [85] explicitly considered the competition between pairing and ferromagnetic instability and concluded that the pairing instability is typically faster than the ferromagnetic instability. From the above discussion it is clear that experimentally investigating ferromagnetism in a Fermi gas must go hand in hand with a study of the pair formation dynamics [88].

## 5.2 Experimental strategy

### Sample preparation

The experiments were carried out with typically  $4.2 \times 10^5$   ${}^6\text{Li}$  atoms in each of the two lower spin states  $|1\rangle$  and  $|2\rangle$  confined in an optical dipole trap with radial and axial trap frequencies  $\omega_r = 2\pi \times 100(1) \text{ s}^{-1}$  and  $\omega_z = 2\pi \times 9.06(25) \text{ s}^{-1}$ . The sample was evaporatively cooled at a magnetic bias field  $B = 320 \text{ G}$ , identical to the procedure described in chapter 3 (far away from the Feshbach resonance the sample is stable and decay into the bound state is negligible). Then the magnetic field was slowly ramped (adiabatically following the upper branch) to  $730 \text{ G}$  ( $k_F a = 0.35$ ) in  $500 \text{ ms}$  (see Figure 5-2). The fraction of atoms being converted to molecules during the ramp was measured (see below for method) to be below 5 %. The temperature of

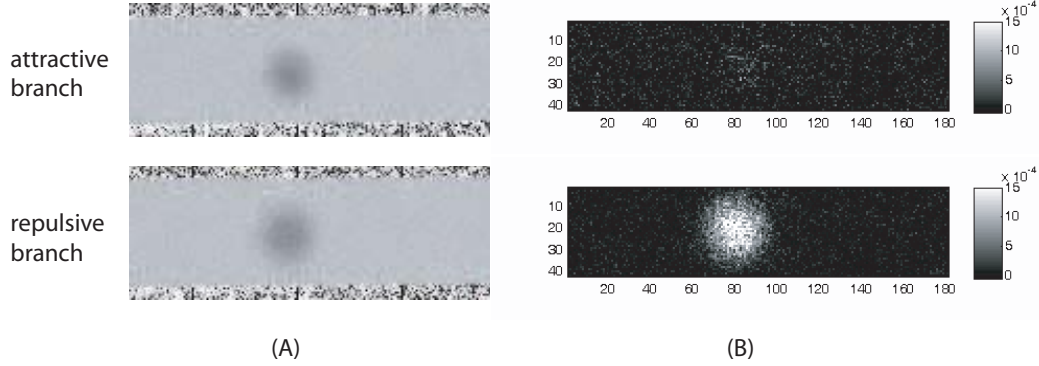


Figure 5-3: (A) Single speckle images and (B) vertically processed  $OD$  noise variance profiles for samples prepared at a magnetic field of 790 G ( $k_F a = 1.1$ ) on the attractive and repulsive interaction branches. While the samples exhibit very similar temperatures and density distributions, the measured amounts of spin noise  $(\Delta(n_1 - n_2))^2$  are dramatically different, reflecting the very different microscopic nature of the two Fermi gases, i.e. Bose-Einstein condensed molecule-like bound atom pairs in one case vs. increasingly anticorrelated fermionic atoms in the other case. A careful inspection reveals that even a single "repulsive" speckle image appears already visibly more granular than its smooth attractive counterpart. The particular trap geometry of a cigar shaped cloud elongated along the imaging axis makes it possible to efficiently measure spin fluctuations accumulated along the long axis. Compared with a non-interacting Fermi gas cloud, the noise variance is suppressed by a factor of 0.2 in the attractive case and enhanced by a factor of 1.4 in the repulsive case. One pixel corresponds to a  $2.6 \mu\text{m}$  square in the object plane.

the cloud was typically  $0.23(3) T_F$  at 527 G with a Fermi energy of  $E_F = k_B T_F = h \times 6.1 \text{ kHz}$ . After rapidly switching the magnetic field from 730 G to the final value in less than  $350 \mu\text{s}$ , spin fluctuations  $\Delta(n_1 - n_2)$  were measured by speckle imaging<sup>3</sup> following the procedures described in chapter 4. Due to the use of 20 cm diameter coils outside the vacuum chamber, the inductance of the magnet coils was  $330 \mu\text{H}$  and the fast switching was accomplished by a servo-controlled rapid discharge of capacitors charged to 500 V [66].

For the experiments reported in chapter 4 samples were prepared on the lower branch of the Feshbach resonance, where positive values of  $k_F a$  correspond to a gas of weakly bound molecules. Accordingly, a suppression of spin fluctuations and an

<sup>3</sup>Optionally an appropriate RF pulse was applied directly before imaging to rotate the spin orientation along the measurement axis, i.e. rotate a possible superposition state  $|1\rangle + |2\rangle$  into  $|1\rangle$  or  $|2\rangle$ .

enhancement of density fluctuations were observed. In this study, on the metastable upper branch of the Feshbach resonance, the situation is reversed, which becomes directly visible when comparing single raw speckle images as shown in Figure 5-3. For unbound atoms, as the interaction strength increases, the two spin components should develop stronger and stronger anticorrelations and enhanced spin fluctuations, eventually reaching a phase transition to a ferromagnetic state where the magnetic susceptibility and therefore the spin fluctuations diverge. Recent Monte Carlo simulations [86] predicted such a divergence around  $k_F a = 0.83$ , not far away from the estimates derived above.

### Domain size and spin fluctuations

When spin domains of  $m$  atoms form, the spin density variance will increase by a factor of  $m$ , which is illustrated by a simplified model assuming Poissonian fluctuations in a given probe volume within the atom sample: With on average  $N$  atoms in this volume one would measure a standard deviation in the atom number of  $\sqrt{N}$ . However, if the atoms formed clusters each made of  $m$  atoms the standard deviation of the number of clusters would be  $\sqrt{N/m}$ , leading to a variance in atom number of  $(m\sqrt{N/m})^2 = mN$ . Consequently, for the above described samples in the critical interaction region a dramatic increase of spin fluctuations by one or several orders of magnitude was expected, depending on the size of the magnetic domains.

## 5.3 Experimental results - Discussion and interpretation

### 5.3.1 Spin fluctuation measurements

Figure 5-4 shows the observed spin fluctuations enhancement compared to the non-interacting cloud at 527 G. The variance enhancement factor reaches its maximum value of 1.6 immediately after the quench, decreasing during the 2 ms afterward. The absence of a dramatic increase shows that no domains form and that the sample

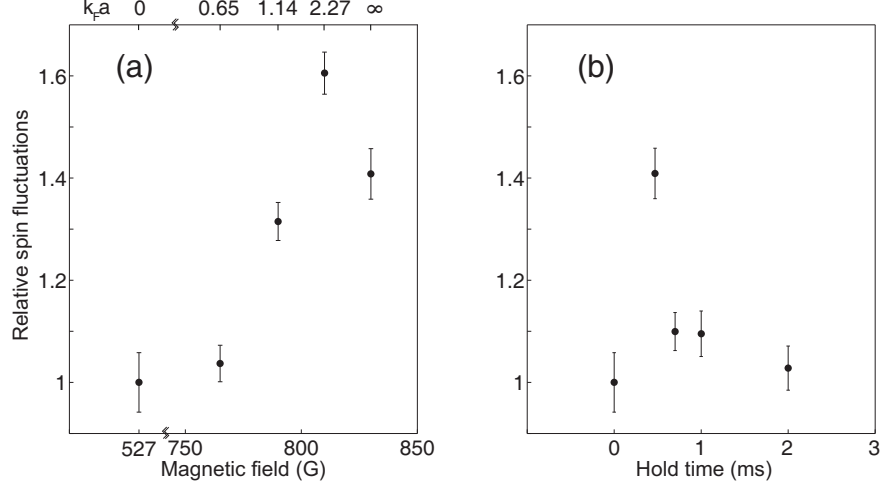


Figure 5-4: Spin fluctuations (a) after  $350 \mu\text{s}$  as a function of magnetic field and (b) on resonance as a function of hold time scaled to the value measured at 527 G. Even at strong repulsive interactions, the measured spin fluctuations are just moderately enhanced, indicating only short-range correlations and no domain formation. The spin fluctuations were determined for square bins of  $2.6 \mu\text{m}$ , each containing on average 1000 atoms per spin state.

remains in the paramagnetic phase throughout. Similar observations were made for a wide range of interaction strengths and wait times. Note that first-order perturbation theory [35] predicts an increase of the susceptibility by a factor of 1.5 at  $k_F a = 0.5$  and by a factor of 2 at  $k_F a = 0.8$  (i.e. no dramatic increase for  $k_F a < 1$ ). Therefore, the measurements show no evidence for the Fermi gas approaching the Stoner instability.

### 5.3.2 Pair formation measurements

To fully interpret the spin fluctuation measurements, one has to take into account the decay of the atomic sample on the upper branch of the Feshbach resonance into bound pairs. The pair formation is characterized by comparing the total number of atoms and molecules  $N_a + 2N_{\text{mol}}$  (determined by taking an absorption image after ballistic expansion at high magnetic field where molecules and atoms have the same absorption resonance) to the number of free atoms (determined by rapidly sweeping the magnetic field to 5G before releasing the atoms and imaging the cloud, converting

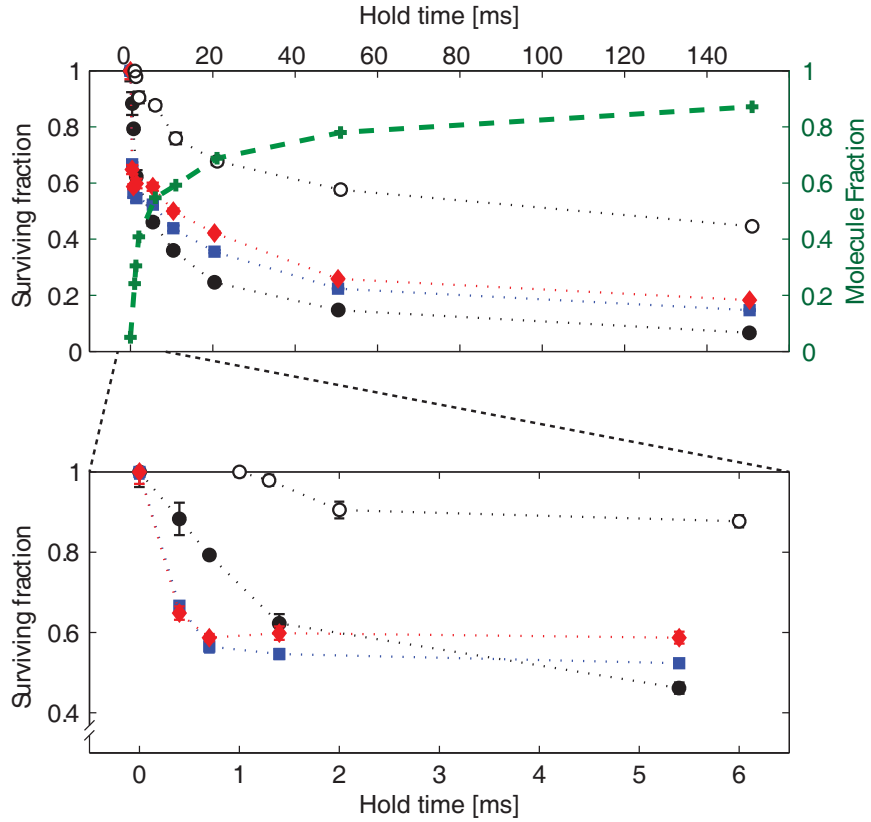


Figure 5-5: Characterization of molecule formation at short and long hold times, and at different values of the interaction strength. The closed symbols, circles (black) at 790G with  $k_F a = 1.14$ , squares (blue) at 810G with  $k_F a = 2.27$  and diamonds (red) at 818G with  $k_F a = 3.5$  represent the normalized number of free atoms, the open symbols the total number of atoms including those bound in Feshbach molecules (open circles at 790G with  $k_F a = 1.14$ ). The crosses (green) show the molecule fraction. The characteristic time scale is set by the Fermi time  $\hbar/E_F = 43\mu\text{s}$ , calculated with a cloud averaged Fermi energy.

pairs into deeply bound molecules that are completely shifted out of resonance) [62].

The time evolution of the molecule production (Figure 5-5) shows two regimes of distinct behavior. Already for times less than 1 ms, a considerable number of atoms is converted into molecules, while the total number  $N_a + 2N_{\text{mol}}$  remains constant. The initial drop in atom number becomes larger as the final magnetic field is increased, and saturates at around 50 % near the Feshbach resonance.

This fast initial decay in atom number can be attributed to recombination [89, 90] into the weakly bound molecular state. One obtains an atom loss rate  $\dot{N}_a/N_a = 250 \text{ s}^{-1}$  at 790 G in the first 1 ms after the magnetic field switch. Assuming a three-body process the rate coefficient  $L_3$  at this field is estimated to be  $3.9 \times 10^{-22} \text{ cm}^6 \text{ s}^{-1}$ , though the interaction is already sufficiently strong for many-body effects to be significant. For stronger interactions, about 30% of atom loss occurs already during the relevant 100  $\mu\text{s}$  of ramping through the strongly interacting region, indicating a lower bound of around  $3 \times 10^3 \text{ s}^{-1}$  for the loss rate which is 13% of the inverse Fermi time  $E_F/\hbar$ , calculated with a cloud averaged Fermi energy.

After the first millisecond, the molecule formation rate slows down, by an order of magnitude at a magnetic field of 790 G (and even more dramatically at higher fields) when it reaches about 50 %. It seems likely that the molecule fraction has reached a quasi-equilibrium value at the local temperature, which is larger than the initial temperature due to local heating accompanying the molecule formation. Reference [91] presents a simple model for the equilibrium between atoms and molecules (ignoring strong interactions). For phase space densities around unity and close to resonance, the predicted molecule fraction is 0.5, in good agreement with the measurements.

For longer time scales (hundred milliseconds) a steady increase of the molecule fraction to 90 % for the longest hold time is observed. This occurs due to continuous evaporation which cools down the system and shifts the atom-molecule equilibrium towards high molecule fractions. During the same time scale, a slow loss in both atom number and total number is observed caused by inelastic collisions (vibrational relaxation of molecules) and evaporation loss.

### 5.3.3 Rate comparison

These results suggest that the conversion into molecules is necessarily comparable to or even faster than the evolution of ferromagnetic domains. First, for strong interactions with  $k_F a$  around 1, one expects both instabilities (pair formation and Stoner instability) to have rates which scale with the Fermi energy  $E_F$  and therefore with  $n^{2/3}$ . Accordingly, one cannot change the competition between the instabilities

by working at higher or lower densities. Following reference [85] the fastest unstable modes for domain formation have a wavevector  $q \approx k_F/2$  and grow at a rate of up to  $E_F/(4\hbar)$  when the cloud is quenched sufficiently far beyond the critical interaction strength. Unstable modes with such wavevectors will develop “domains” of half a wavelength or size  $\xi = \pi/q = 2\pi/k_F$  containing 5 atoms per spin state in a volume  $\xi^3$ . This rate is comparable to the observed conversion rates into pairs of  $0.13 E_F$ . Therefore, at best, “domains” of a few particles could form, but before they can grow further and prevent the formation of pairs (in a fully polarized state), rapid pair formation takes over and populates the lower branch of the Feshbach resonance.

### 5.3.4 Temperature considerations

An important question regarding the phase transition is the existence of a temperature threshold for domain formation. Available theoretical treatments do not predict an exact maximum transition temperature to the ferromagnetic state. Since the only energy scale is the Fermi temperature, it is reasonable to expect a transition temperature which is a fraction of the Fermi temperature [92], higher or around the temperature scale probed in the experiment. However, even above the transition temperature, the susceptibility should not abruptly fall off.

Temperatures are notoriously difficult to measure in a transient way for a dynamic system which may not be in full equilibrium. For example, standard cloud shape thermometry [50] requires full equilibration and lifetimes much longer than the longest trap period. Noise thermometry (see chapter 3) on the other hand does not rely on a global cloud equilibrium and is therefore an ideal tool to estimate temperatures of such samples. Temperatures were measured after the hold time near the Feshbach resonance by quickly switching the magnetic field to weak interactions at 527 G and then performing noise thermometry using speckle imaging as described in chapter 4. The measurements found column-integrated fluctuations that are  $0.61(8)$  of the Poisson value which implies an effective temperature well below  $T_F$ , around  $0.33(7) T_F$ , not much higher than the initial temperature of  $0.23 T_F$ .

Alternatively, the temperature increase can be estimated from the heat released

by pair formation. Molecule formation heats the sample by transferring the binding energy and excess kinetic energy of the molecules to the remaining atoms, and also by creating holes in the Fermi sea. For small values of  $k_F a$ , the total energy release per molecule is therefore  $\hbar^2/(ma^2) + 2E_F$ . From the energy per particle [29] for an ideal homogeneous degenerate Fermi gas  $E = 0.6 E_F [1 + (5\pi^2/12)(T/T_F)^2]$  one obtains

$$\frac{T}{T_F} = \sqrt{\frac{4\eta}{\pi^2} \left( 1 + \frac{1}{(k_F a)^2} \right)} \quad (5.3)$$

for the final temperature with a small molecule fraction  $\eta$  (assuming initially  $\eta = 0$  and  $T = 0$ ). Evaluating this result at  $k_F a = 1$ , where the two-body binding energy is  $2E_F$ , one finds that molecule fractions of higher than 20 % result in a final temperature above  $0.4T_F$ , an estimate which is somewhat higher than the measurement reported above.

### 5.3.5 Kinetic energy and release energy

Jo et al. reported in [25] evidence for ferromagnetic domains also based on the observation of a non-monotonic behavior of the kinetic energy when measured at increasing interaction strengths. Given the negative results obtained via noise measurements it is appropriate to reexamine the kinetic energy findings employing an experimental setup with better time resolution.

The energy of a trapped interacting gas is the sum of three contributions: the kinetic energy, the interaction energy, and the potential energy in the trapping potential.

$$E = T + U_{\text{int}} + U_{\text{trap}} \quad (5.4)$$

By suddenly releasing the atoms from the trap and measuring the radius of the cloud, it is possible to measure either the release energy ( $T + U_{\text{int}}$ ) or the kinetic energy  $T$ , depending on whether the interactions are left on or are switched off, respectively,

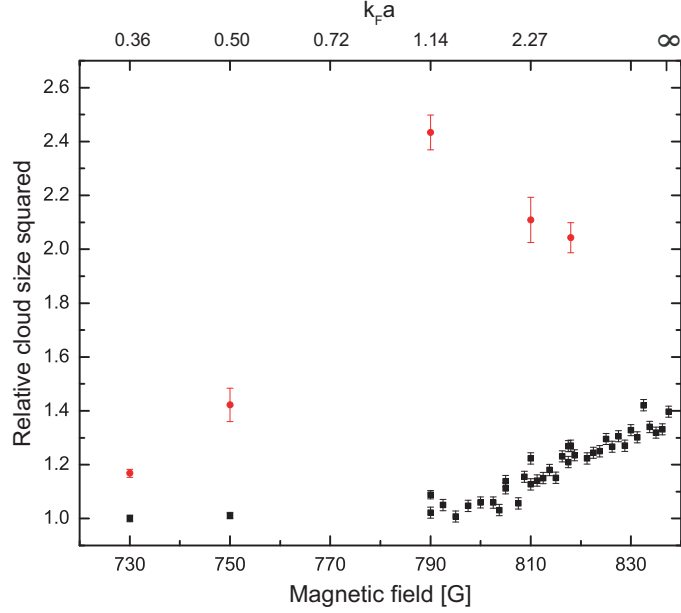


Figure 5-6: Measured transverse mean square cloud size after time-of-flight expansion as a function of the interaction strength before the release in units of the value of the noninteracting cloud. The interactions are switched off (black squares) or left on (red circles) at the time of release. For sufficiently long time-of-flight the transverse 2D release energy is directly proportional to the measured mean square width of the cloud. The expansion is either isotropic (in the case of switched off interactions) or mostly transverse (in case of strong interactions leading to hydrodynamic expansion) [93, 94]. Uncertainties as indicated by the error bars are purely statistical.

at the time of release, by leaving the external magnetic field constant or rapidly switching it to a value away from the Feshbach resonance.

As described before the system is prepared with variable interaction strength by switching the magnetic field to a value near the Feshbach resonance. For the kinetic energy measurement, the field is again rapidly switched to 5 G, after which the atoms are released from the trap. After 8 ms of free expansion, the size of the cloud reflects the width of the in-trap momentum distribution and the average in-trap kinetic energy. The in Figure 5-6 documented increase in kinetic energy with increasing interaction strength reflects the onset of pair anti-correlations of opposite-spin atoms - those anti-correlations reduce the repulsive potential energy at the price of increased kinetic energy. This increase in kinetic energy is consistent with the observations in

reference [25]. However, no minimum in kinetic energy as in [25] is observed, since the interactions are suddenly increased and the cloud cannot adiabatically expand during the ramp as was the case in the earlier work. For fully spin-polarized domains, the kinetic energy would increase by a factor of  $2^{2/3}$  which provides an upper bound (since the true ground state must have an energy lower than or equal to the fully phase-separated state). The smaller observed energy increase (factor of 1.3) implies that fully spin polarized domains have not formed. It should be noted that the kinetic energy increase is insensitive to the correlation length or size of domains and cannot clearly distinguish between ferromagnetic domains and strong anti-correlations [78, 95].

In-trap kinetic plus interaction energies are measured when the magnetic field is left at its value near the Feshbach resonance while the trap is switched off. After 4 ms of the 8 ms free expansion the field is switched to 5 G for imaging. The resulting cloud size is directly related to the release energy of the cloud, the sum of the in-trap kinetic and interaction energies. Starting around  $k_F a = 0.5$ , a strong increase of the transverse release energy by a factor of about 2 is observed<sup>4</sup>. The comparison of kinetic energy and release energy at 790G and 810G shows that the extra energy due to repulsive interactions is clearly dominated by repulsive potential energy and not by kinetic energy. The latter would occur for ferromagnetic domains. In case of fully spin-polarized domains, the repulsive interaction energy would vanish, and kinetic energy and release energy should be the same. Therefore, these energy measurements support the conclusions derived from the noise measurements and help to rule out a ferromagnetic phase.

The interaction-strength dependence of the release energy shows a maximum at 790 G, but the ground state energy should vary monotonically with the strength of the repulsive interactions. Therefore, the observed maximum is most likely related to non-equilibrium excitations caused by the sudden jump in the scattering length, indicating that these energy measurements are possibly affected by systematic errors

---

<sup>4</sup>This implies that the total energy has increased by a factor of 5/3 compared to the non-interacting case since the interactions modify the expansion from ballistic to hydrodynamic.

and need to be interpreted with caution.

### 5.3.6 Time scales for domain growth vs. experimental resolution

When investigating the molecule production dynamics two separate time scales were found - a sub-ms timescale for rapid pair formation, followed by a slower time scale of tens of milliseconds where further cooling led to a full conversion of the atomic into a molecular gas. For comparison it is important to discuss in more detail over what time scale one could have observed ferromagnetic domain formation if it had happened.

As mentioned before, Pekker et al. [85] predicted in uniform systems fast growth rates for small domains. Unstable modes with wavevector  $q \approx k_F/2$  grow at a rate of up to  $E_F/4\hbar$  when the cloud is quenched sufficiently far beyond the critical interaction strength. This corresponds to a growth time of around  $100\mu\text{s}$ . For a wide range of interactions and wavevectors, the predicted growth time is faster than  $10\hbar/E_F$  or  $250\mu\text{s}$ . During this time one would expect the thermal fluctuations to increase by a factor of  $e$ .

Wavevectors  $q \approx k_F/2$  will develop “domains” of half a wavelength or size  $\xi = \pi/q = 2\pi/k_F$ , which is  $2.3\mu\text{m}$  at the experimental density of  $3 \times 10^{11} \text{ cm}^{-3}$  corresponding to  $k_F = 2.7 \times 10^4 \text{ cm}^{-1}$ . For speckle imaging the smallest effective probe volume is given by the nominal optical resolution of the lens system which is approximately equal to the bin size of  $2.6\mu\text{m}$  in this experiment. For a bin size  $d$ , the measured fluctuations are an integral over fluctuations at all wavevectors  $q$  with an effective cutoff around  $1/d$ . Due to a mode density factor  $q^2$  the largest contribution comes from wavevectors around  $\pi/d$  which is equal to  $0.4 k_F$  for the given experimental parameters, fortuitously close to the wavevector of the fastest growing unstable modes. Therefore, for a quench across a ferromagnetic phase transition, one would have expected a sub-millisecond growth time for the spin fluctuations, which was not observed.

Since the experiment starts with a balanced two-state mixture with zero spin density, formation of random (i.e. uncorrelated) domains requires spin diffusion. Full sensitivity to domains requires spin transport over a distance equal to the effective measurement bin size. Assuming diffusive motion at resonant interactions with a spin diffusivity  $D_s \approx h/m$  as observed in [96] results in a corresponding minimum wait time of about  $300\mu s$ . This means that after crossing a ferromagnetic phase transition, formation of domains of a few to tens of particles should have occurred on ms scales and should have resulted in an observable increase of spin fluctuations.

## 5.4 Conclusions

The experiment has not shown any evidence for a possible ferromagnetic phase in an atomic gas in “chemical” equilibrium with dimers. This implies one of the following possibilities.

- (i) The system can be described by a simple Hamiltonian with strong short range repulsion; however, this Hamiltonian does not lead to ferromagnetism. This would be in conflict with the results of recent quantum Monte-Carlo simulations [86, 87] and second order perturbation theory [77], and in agreement with conclusions based on Tan relations [97].
- (ii) The temperature of the gas was too high to observe ferromagnetism. This would then imply a critical temperature around or below  $0.2 T/T_F$ , lower than generally assumed.
- (iii) The presence of a small molecule fraction alters the system sufficiently so that it cannot be described anymore by the simple model of an atomic gas with short-range repulsive interactions.

A previous experiment [25] reported evidence for ferromagnetism by presenting non-monotonic behavior of atom loss rate, kinetic energy and cloud size when approaching the Feshbach resonance, in agreement with predictions based on the Stoner

model. The new measurements confirm that the properties of the gas change near  $k_F a = 1$ . Similar to [25], features in kinetic and release energy measurements are observed near the resonance. However, the behavior is more complex than that captured by simple models. Furthermore, the atomic fraction decays non-exponentially (see Figure 5-5), and therefore an extracted decay time will depend on the details of the measurement such as time resolution. Reference [25] found a maximum of the loss rate of  $200 \text{ s}^{-1}$  for a Fermi energy of 28 kHz. The now measured lower bound of the decay rate of  $3 \times 10^3 \text{ s}^{-1}$  is 15 times faster at a five times smaller Fermi energy. In view of all this it appears very unlikely that reference [25] has observed ferromagnetic behavior.

Overall one can conclude that an ultracold gas with strong short range repulsive interactions near a Feshbach resonance remains in the paramagnetic phase. The fast formation of molecules and the accompanying heating makes it impossible to study such a gas in equilibrium, confirming predictions of a rapid conversion of the atomic gas to pairs [85, 98]. Therefore, the Stoner criterion cannot be applied to ultracold Fermi gases with short-range repulsive interactions since the neglected competition with pairing is crucial.

Interesting topics for future research on ferromagnetism and pair formation include the effects of dimensionality [99, 100], spin imbalance [101, 102], mass imbalance [103], and lattice and band structure [104, 105].

# Chapter 6

## Conclusions and outlook

In summary this thesis reported on the successful realization of universal noise measurements in quantum degenerate Fermi gases. Starting from theoretical considerations about the fluctuation properties of noninteracting and interacting quantum gases, a noise measurement and analysis concept based on finely resolved atom counting was developed and experimentally implemented for an expanded noninteracting Fermi gas. The new technique was carefully characterized and the measurement results were found to quantitatively reproduce the theoretical expectations.

In a second step the introduction of speckle imaging made it possible to adapt the previous strategies to the requirements of in-situ measurements in interacting gases. Speckle imaging, relying on the conversion of density fluctuations into imaging light wavefront phase ripple that is then converted into intensity noise on the light detector, turned out to be a simple and versatile tool for the study of atom-atom correlations in two-component mixtures. The obtained results allowed conclusions about microscopic properties of the interacting gas along the BEC-BCS crossover.

Finally a third experiment explored via speckle imaging the correlation properties of a repulsively interacting metastable Fermi gas. Following the Stoner model of ferromagnetism several theories suggested for this system a phase transition to a ferromagnetic state accompanied by the formation of macroscopic pseudospin domains. A recent experimental study reported further evidence for such a phase transition, but against all expectations the noise measurements could not confirm these findings.

Instead, a detailed analysis of competing atom pair formation processes led to the conclusion that the fast decay dynamics into molecules inhibits any proper domain growth.

While it might be interesting to pursue additional research along one of these directions, it will be most rewarding in the future to take the fluctuation measurements one step further by applying them to the study of a variety of systems in optical lattices and other new quantum phases yet to explore. In this sense the work presented in this thesis contributed towards the implementation of a universal quantum simulator.

# Appendix A

## Suppression of Density Fluctuations in a Quantum Degenerate Fermi Gas

This appendix contains a printout of *Phys. Rev. Lett.* 105, 040402 (2010): Christian Sanner, Edward J. Su, Aviv Keshet, Ralf Gommers, Yong-il Shin, Wujie Huang, and Wolfgang Ketterle, *Suppression of Density Fluctuations in a Quantum Degenerate Fermi Gas*.



## Suppression of Density Fluctuations in a Quantum Degenerate Fermi Gas

Christian Sanner, Edward J. Su, Aviv Keshet, Ralf Gommers, Yong-il Shin, Wujie Huang, and Wolfgang Ketterle

*MIT-Harvard Center for Ultracold Atoms, Research Laboratory of Electronics, and Department of Physics,  
Massachusetts Institute of Technology, Cambridge Massachusetts 02139, USA*

(Received 7 May 2010; published 19 July 2010)

We study density profiles of an ideal Fermi gas and observe Pauli suppression of density fluctuations (atom shot noise) for cold clouds deep in the quantum degenerate regime. Strong suppression is observed for probe volumes containing more than 10 000 atoms. Measuring the level of suppression provides sensitive thermometry at low temperatures. After this method of sensitive noise measurements has been validated with an ideal Fermi gas, it can now be applied to characterize phase transitions in strongly correlated many-body systems.

DOI: 10.1103/PhysRevLett.105.040402

PACS numbers: 03.75.Ss, 05.30.Fk, 67.85.Lm

Systems of fermions obey the Pauli exclusion principle. Processes that would require two fermions to occupy the same quantum state are suppressed. In recent years, several classic experiments have directly observed manifestations of Pauli suppression in Fermi gases. Antibunching and the suppression of noise correlations are a direct consequence of the forbidden double occupancy of a quantum state. Such experiments were carried out for electrons [1–3], neutral atoms [4,5], and neutrons [6]. In principle, such experiments can be done with fermions at any temperature, but in practice low temperatures increase the signal. A second class of (two-body) Pauli suppression effects, the suppression of collisions, requires a temperature low enough such that the de Broglie wavelength of the fermions becomes larger than the range of the interatomic potential and  $p$ -wave collisions freeze-out. Experiments observed the suppression of elastic collisions [7] and of clock shifts in radio frequency spectroscopy [8,9].

Here we report on the observation of Pauli suppression of density fluctuations. This is, like the suppression of collisions between different kinds of fermions [10], a many-body phenomenon which occurs only at even lower temperatures in the quantum degenerate regime, where the Fermi gas is cooled below the Fermi temperature and the low lying quantum states are occupied with probabilities close to 1. In contrast, an ideal Bose gas close to quantum degeneracy shows enhanced fluctuations [11].

The development of a technique to sensitively measure density fluctuations was motivated by the connection between density fluctuations and compressibility through the fluctuation-dissipation theorem. In this Letter, we validate our technique for determining the compressibility by applying it to the ideal Fermi gas. In future work, it could be extended to interesting many-body phases in optical lattices which are distinguished by their incompressibility [12]. These include the band insulator, Mott insulator, and also the antiferromagnet for which spin fluctuations, i.e., fluctuations of the difference in density between the two spin states are suppressed.

Until now, sub-Poissonian number fluctuations of ultracold atoms have been observed only for small clouds of bosons with typically a few hundred atoms [13–16] and directly [17,18] or indirectly [19] for the bosonic Mott insulator in optical lattices. For fermions in optical lattices, the crossover to an incompressible Mott insulator phase was inferred from the fraction of double occupations [20] or the cloud size [21]. Here we report the observation of density fluctuations in a large cloud of fermions, showing sub-Poissonian statistics for atom numbers in excess of 10 000 per probe volume.

The basic concept of the experiment is to repeatedly produce cold gas clouds and then count the number of atoms in a small probe volume within the extended cloud. Many iterations allow us to determine the average atom number  $N$  in the probe volume and its variance  $(\Delta N)^2$ . For independent particles, one expects Poisson statistics, i.e.,  $(\Delta N)^2/\langle N \rangle = 1$ . This is directly obtained from the fluctuation-dissipation theorem  $(\Delta N)^2/\langle N \rangle = nk_B T \kappa_T$ , where  $n$  is the density of the gas, and  $\kappa_T$  the isothermal compressibility. For an ideal classical gas  $\kappa_T = 1/(nk_B T)$ ,

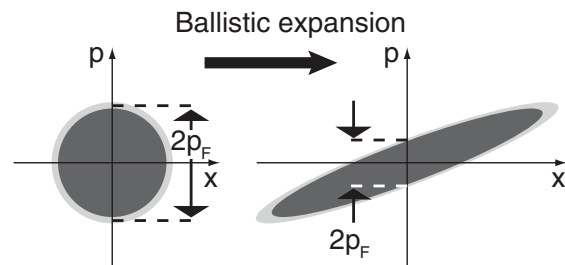


FIG. 1. Phase space diagram of ballistic expansion of a harmonically trapped Fermi gas. Ballistic expansion conserves phase space density and shears the initially occupied spherical area into an ellipse. In the center of the cloud, the local Fermi momentum and the sharpness of the Fermi distribution are scaled by the same factor, keeping the ratio of local temperature to Fermi energy constant. The same is true for all points in the expanded cloud relative to their corresponding unscaled in-trap points.

and one retrieves Poissonian statistics. For an ideal Fermi gas close to zero temperature with Fermi energy  $E_F$ ,  $\kappa_T = 3/(2nE_F)$ , and the variance  $(\Delta N)^2$  is suppressed below Poissonian fluctuations by the Pauli suppression factor  $3k_B T/(2E_F)$ . All number fluctuations are thermal, as indicated by the proportionality of  $(\Delta N)^2$  to the temperature in the fluctuation-dissipation theorem. Only for the ideal classical gas, where the compressibility diverges as  $1/T$ , one obtains Poissonian fluctuations even at zero temperature.

The counting of atoms in a probe volume can be done with trapped atoms, or after ballistic expansion. Ballistic expansion maintains the phase space density and therefore the occupation statistics. Consequently, density fluctuations are exactly rescaled in space by the ballistic expansion factors as shown in Fig. 1 [22,23]. Note that this rescaling is a unique property of the harmonic oscillator potential, so future work on density fluctuations in optical lattices must employ in-trap imaging. For the present work, we chose ballistic expansion. This choice increases the number of fully resolved bins due to optical resolution and depth of field, it allows adjusting the optimum optical density by choosing an appropriate expansion time, and it avoids image artifacts at high magnification.

We first present our main results, and then discuss important aspects of sample preparation, calibration of absorption cross section, data analysis and corrections for photon shot noise. Figure 2(a) shows an absorption image of an expanding cloud of fermionic atoms. The probe volume, in which the number of atoms is counted, is

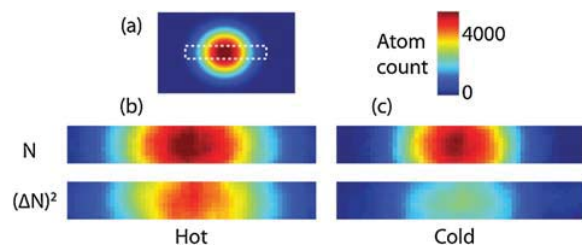


FIG. 2 (color online). Comparison of density images to variance images. For Poissonian fluctuations, the two images at a given temperature should be identical. The variance images were obtained by determining the local density fluctuations from a set of 85 images taken under identical conditions. (a) Two dimensional image of the optical density of an ideal Fermi gas after 7 ms of ballistic expansion. The noise data were taken by limiting the field of view to the dashed region of interest, allowing for faster image acquisition. (b) For the heated sample, variance and density pictures are almost identical, implying only modest deviation from Poissonian statistics. (c) Fermi suppression of density fluctuations deep in the quantum degenerate regime manifests itself through the difference between density and variance picture. Especially in the center of the cloud, there is a large suppression of density fluctuations. The variance images were smoothed over  $6 \times 6$  bins. The width of images (b) and (c) is 2 mm.

chosen to be  $26 \mu\text{m}$  in the transverse directions, and extends through the entire cloud in the direction of the line of sight. The large transverse size avoids averaging of fluctuations due to finite optical resolution. From 85 such images, after careful normalization [24], the variance in the measured atom number is determined as a function of position. After subtracting the photon shot noise contribution, a 2D image of the atom number variance  $(\Delta N)^2$  is obtained. For a Poissonian sample (with no suppression of fluctuations), this image would be identical to an absorption image showing the number of atoms per probe volume. This is close to the situation for the hottest cloud (the temperature was limited by the trap depth), whereas the colder clouds show a distinct suppression of the atom number variance, especially in the center of the cloud where the local  $T/T_F$  is smallest.

In Fig. 3, profiles of the variance are compared to theoretical predictions [25,26]. Density fluctuations at wave vector  $q$  are proportional to the structure factor  $S(q, T)$ . Since our probe volume (transverse size  $26 \mu\text{m}$ ) is much larger than the inverse Fermi wave vector of the expanded cloud ( $1/q_F = 1.1 \mu\text{m}$ ),  $S(q = 0, T)$  has been integrated along the line of sight for comparison with the experimental profiles. Within the local density approximation,  $S(q = 0, T)$  at a given position in the trap is the binomial variance  $n_k(1 - n_k)$  integrated over all momenta, where the occupation probability  $n_k(k, \mu, T)$  is obtained from the Fermi-Dirac distribution with a local chemical potential  $\mu$  determined by the shape of the trap. Figure 4 shows the dependence of the atom number variance on atom number for the hot and cold clouds. A statistical analysis of the data used in the figure is in [24].

The experiments were carried out with typically  $2.5 \times 10^6$   ${}^6\text{Li}$  atoms per spin state confined in a round crossed dipole trap with radial and axial trap frequencies  $\omega_r = 2\pi \times 160 \text{ s}^{-1}$  and  $\omega_z = 2\pi \times 230 \text{ s}^{-1}$  corresponding to an in-trap Fermi energy of  $E_F = k_B \times 2.15 \mu\text{K}$ . The sam-

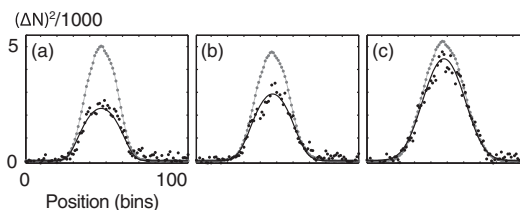


FIG. 3. Comparison of observed variances (black dots) with a theoretical model (black line) and the observed atom number (gray), at three different temperatures (a, b, and c), showing 50, 40, and 15% suppression. Noise thermometry is implemented by fitting the observed fluctuations, resulting in temperatures  $T/T_F$  of  $0.23 \pm .01$ ,  $0.33 \pm .02$ , and  $0.60 \pm .02$ . This is in good agreement with temperatures  $0.21 \pm .01$ ,  $0.31 \pm .01$ , and  $0.6 \pm .1$  obtained by fitting the shape of the expanded cloud [32]. The quoted uncertainties correspond to 1 standard deviation and are purely statistical.

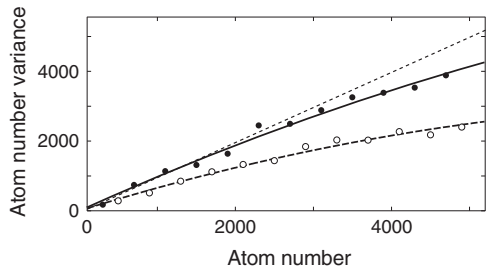


FIG. 4. Atom number variance vs average atom number. For each spatial position, the average atom number per bin and its variance were determined using 85 images. The filled and open circles in the figure are averages of different spatial bin positions with similar average atom number. For a hot cloud at  $T/T_F = 0.6$  (filled circles), the atom number variance is equal to the average atom number (dotted line, full Poissonian noise) in the spatial wings where the atom number is low. The deviation from the linear slope for a cold cloud at  $T/T_F = 0.21$  (open circles) is due to Pauli suppression of density fluctuations. There is also some suppression at the center of the hot cloud, where the atom number is high. The solid and dashed lines are quadratic fits for the hot and cold clouds to guide the eye.

ple was prepared by laser cooling followed by sympathetic cooling with  $^{23}\text{Na}$  in a magnetic trap.  $^6\text{Li}$  atoms in the highest hyperfine state were transferred into the optical trap, and an equal mixture of atoms in the lowest two hyperfine states was produced. The sample was then evaporatively cooled by lowering the optical trapping potential at a magnetic bias field  $B = 320 \pm 5$  G where a scattering length of  $-300$  Bohr radii ensured efficient evaporation. Finally, the magnetic field was increased to  $B = 520 \pm 5$  G, near the zero crossing of the scattering length. Absorption images were taken after 7 ms of ballistic expansion.

We were careful to prepare all samples with similar cloud sizes and central optical densities to ensure that they were imaged with the same effective cross section and resolution. Hotter clouds were prepared by heating the colder cloud using parametric modulation of the trapping potential. For the hottest cloud this was done near 520 G to avoid excessive evaporation losses.

Atomic shot noise dominates over photon shot noise only if each atom absorbs several photons. As a result, the absorption images were taken using the cycling transition to the lowest lying branch of the  $^2P_{3/2}$  manifold. However, the number of absorbed photons that could be tolerated was severely limited by the acceleration of the atoms by the photon recoil, which Doppler shifts the atoms out of resonance. Consequently, the effective absorption cross section depends on the probe laser intensity and duration. To remove the need for nonlinear normalization procedures, we chose a probe laser intensity corresponding to an average of only 6 absorbed photons per atom during a 4  $\mu\text{s}$  exposure. At this intensity, about 12% of the  $^6\text{Li}$  saturation intensity, the measured optical density was 20% lower than its low-intensity value [24]. For each

bin, the atom number variance  $(\Delta N)^2$  is obtained by subtracting the known photon shot noise from the variance in the optical density  $(\Delta \text{OD})^2$  [24]:

$$\frac{\sigma^2}{A^2} (\Delta N)^2 = (\Delta \text{OD})^2 - \frac{1}{\langle N_1 \rangle} - \frac{1}{\langle N_2 \rangle} \quad (1)$$

Here,  $\langle N_1 \rangle$  ( $\langle N_2 \rangle$ ) are the average photon numbers per bin of area  $A$  in the image with (without) atoms and  $\sigma$  is the absorption cross section.

The absorption cross section is a crucial quantity in the conversion factor between the optical density and the number of detected atoms. For the cycling transition, the resonant absorption cross section is  $2.14 \times 10^{-13} \text{ m}^2$ . Applying the measured 20% reduction mentioned above leads to a value of  $1.71 \times 10^{-13} \text{ m}^2$ . This is an upper limit to the cross section due to imperfections in polarization and residual line broadening. An independent estimate of the effective cross section of  $1.48 \times 10^{-13} \text{ m}^2$  was obtained by comparing the integrated optical density to the number of fermions necessary to fill up the trap to the chemical potential. The value of the chemical potential was obtained from fits to the ballistic expansion pictures that allowed independent determination of the absolute temperature and the fugacity of the gas. We could not precisely assess the accuracy of this value of the cross section, since we did not fully characterize the effect of a weak residual magnetic field curvature on trapping and on the ballistic expansion. The most accurate value for the effective cross section was determined from the observed atom shot noise itself. The atom shot noise in the wings of the hottest cloud is Poissonian, and this condition determines the absorption cross section. Requiring that the slope of variance of the atom number  $(\Delta N)^2$  vs atom number  $N$  is unity (see Fig. 4) results in a value of  $(1.50 \pm 0.12) \times 10^{-13} \text{ m}^2$  for the effective cross section in good agreement with the two above estimates.

The spatial volume for the atom counting needs to be larger than the optical resolution. For smaller bin sizes (i.e., small counting volumes), the noise is reduced since the finite spatial resolution and depth of field blur the absorption signal. In our setup, the smallest bin size without blurring was determined by the depth of field, since the size of the expanded cloud was larger than the depth of field associated with the diffraction limit of our optical system. We determined the effective optical resolution by binning the absorption data over more and more pixels of the CCD camera, and determining the normalized central variance  $(\Delta N)^2/N$  vs bin size [24]. The normalized variance increased and saturated for bin sizes larger than 26  $\mu\text{m}$  (in the object plane), and this bin size was used in the data analysis. We observe the same suppression ratios for bin sizes as large as 40  $\mu\text{m}$ , corresponding to more than 10 000 atoms per bin.

For a cold fermion cloud, the zero temperature structure factor  $S(q)$  becomes unity for  $q > 2q_F$ . This reflects the

fact that momentum transfer above  $2q_F$  to any particle will not be Pauli suppressed by occupation of the final state. In principle, this can be observed by using bin sizes smaller than the Fermi wavelength, or by Fourier transforming the spatial noise images. For large values of  $q$ , Pauli suppression of density fluctuations should disappear, and the noise should be Poissonian. However, our imaging system loses its contrast before  $q \approx 2q_F$  [24].

Observation of density fluctuations, through the fluctuation-dissipation theorem, determines the product of temperature and compressibility. It provides an absolute thermometer, as demonstrated in Fig. 3 if the compressibility is known or is experimentally determined from the shape of the density profile of the trapped cloud [17,27]. Because variance is proportional to temperature for  $T \ll T_F$ , noise thermometry maintains its sensitivity at very low temperature, in contrast to the standard technique of fitting spatial profiles.

Density fluctuations lead to Rayleigh scattering of light. The differential cross section for scattering light of wave vector  $k$  by an angle  $\theta$  is proportional to the structure factor  $S(q)$ , where  $q = 2k \sin(\theta/2)$  [26]. In this work, we have directly observed the Pauli suppression of density fluctuations and therefore  $S(q) < 1$ , implying suppression of light scattering at small angles (corresponding to values of  $q$  inversely proportional to our bin size). How are the absorption images affected by this suppression? Since the photon recoil was larger than the Fermi momentum of the expanded cloud, large-angle light scattering is not suppressed. For the parameters of our experiment, we estimate that the absorption cross section at the center of a  $T = 0$  Fermi cloud is reduced by only 0.3% due to Pauli blocking [28]. Although we have not directly observed Pauli suppression of light scattering, which has been discussed for over 20 years [28–30], by observing reduced density fluctuations we have seen the underlying mechanism for suppression of light scattering.

In conclusion, we have established a sensitive technique for determining atomic shot noise and observed the suppression of density fluctuations in a quantum degenerate ideal Fermi gas. This technique is promising for thermometry of strongly correlated many-body systems and for observing phase-transitions or cross-overs to incompressible quantum phases.

We acknowledge Joseph Thywissen and Markus Greiner for useful discussions. This work was supported by NSF and the Office of Naval Research, AFOSR (through the MURI program), and under Army Research Office grant no. W911NF-07-1-0493 with funds from the DARPA Optical Lattice Emulator program.

*Note added in proof.*—Results similar to ours are reported in Ref. [31].

- [1] W. D. Oliver, J. Kim, R. C. Liu, and Y. Yamamoto, *Science* **284**, 299 (1999).
- [2] M. Henny *et al.*, *Science* **284**, 296 (1999).
- [3] H. Kiesel, A. Renz, and F. Hasselbach, *Nature (London)* **418**, 392 (2002).
- [4] T. Rom *et al.*, *Nature (London)* **444**, 733 (2006).
- [5] T. Jelte *et al.*, *Nature (London)* **445**, 402 (2007).
- [6] M. Iannuzzi *et al.*, *Phys. Rev. Lett.* **96**, 080402 (2006).
- [7] B. DeMarco *et al.*, *Phys. Rev. Lett.* **82**, 4208 (1999).
- [8] M. W. Zwierlein, Z. Hadzibabic, S. Gupta, and W. Ketterle, *Phys. Rev. Lett.* **91**, 250404 (2003).
- [9] S. Gupta *et al.*, *Science* **300**, 1723 (2003).
- [10] B. DeMarco, S. B. Papp, and D. S. Jin, *Phys. Rev. Lett.* **86**, 5409 (2001).
- [11] J. Estève *et al.*, *Phys. Rev. Lett.* **96**, 130403 (2006).
- [12] Q. Zhou, Y. Kato, N. Kawashima, and N. Trivedi, *arXiv:0901.0606*.
- [13] C. S. Chuu *et al.*, *Phys. Rev. Lett.* **95**, 260403 (2005).
- [14] J. Estève *et al.*, *Nature (London)* **455**, 1216 (2008).
- [15] S. Whitlock, C. F. Ockeloen, and R. J. C. Spreeuw, *Phys. Rev. Lett.* **104**, 120402 (2010).
- [16] A. Itah *et al.*, *Phys. Rev. Lett.* **104**, 113001 (2010).
- [17] N. Gemelke, X. Zhang, C. L. Hung, and C. Chin, *Nature (London)* **460**, 995 (2009).
- [18] M. Greiner (unpublished).
- [19] M. Greiner, O. Mandel, T. W. Hänsch, and I. Bloch, *Nature (London)* **419**, 51 (2002).
- [20] R. Jördens *et al.*, *Nature (London)* **455**, 204 (2008).
- [21] U. Schneider *et al.*, *Science* **322**, 1520 (2008).
- [22] S. Gupta, Z. Hadzibabic, J. R. Anglin, and W. Ketterle, *Phys. Rev. Lett.* **92**, 100401 (2004).
- [23] G. M. Bruun and C. W. Clark, *Phys. Rev. A* **61**, 061601(R) (2000).
- [24] See supplementary material at <http://link.aps.org/supplemental/10.1103/PhysRevLett.105.040402> for additional details.
- [25] Y. Castin, in *Proceedings of the International School of Physics Enrico Fermi, Course CLXIV*, edited by M. Inguscio, W. Ketterle, and C. Salomon (IOS, Amsterdam, 2008).
- [26] D. Pines and P. Nozières, *The Theory of Quantum Liquids* (Addison-Wesley, MA, 1988), Vol. 1.
- [27] Q. Zhou and T. L. Ho, *arXiv:0908.3015*.
- [28] A. Görlitz, A. P. Chikkatur, and W. Ketterle, *Phys. Rev. A* **63**, 041601(R) (2001).
- [29] K. Helmerson, M. Xiao, and D. E. Pritchard, in *International Quantum Electronics Conference 1990, Book of Abstracts*, econf QTHH4 (1990).
- [30] B. Shuve and J. H. Thywissen, *J. Phys. B* **43**, 015301 (2010). (and references therein)
- [31] T. Mueller *et al.*, *Phys. Rev. Lett.* **105**, 040401 (2010).
- [32] W. Ketterle and M. W. Zwierlein, in *Proceedings of the International School of Physics Enrico Fermi, Course CLXIV*, edited by M. Inguscio, W. Ketterle, and C. Salomon (IOS, Amsterdam, 2008).

## Appendix B

# Speckle Imaging of Spin Fluctuations in a Strongly Interacting Fermi Gas

This appendix contains a printout of *Phys. Rev. Lett.* 106, 010402 (2011): Christian Sanner, Edward J. Su, Aviv Keshet, Wujie Huang, Jonathon Gillen, Ralf Gommers, and Wolfgang Ketterle, *Speckle Imaging of Spin Fluctuations in a Strongly Interacting Fermi Gas*.

## Speckle Imaging of Spin Fluctuations in a Strongly Interacting Fermi Gas

Christian Sanner, Edward J. Su, Aviv Keshet, Wujie Huang, Jonathon Gillen, Ralf Gommers, and Wolfgang Ketterle

*MIT-Harvard Center for Ultracold Atoms, Research Laboratory of Electronics, and Department of Physics, Massachusetts Institute of Technology, Cambridge Massachusetts 02139, USA*

(Received 8 October 2010; revised manuscript received 10 December 2010; published 6 January 2011)

Spin fluctuations and density fluctuations are studied for a two-component gas of strongly interacting fermions along the Bose-Einstein condensate-BCS crossover. This is done by *in situ* imaging of dispersive speckle patterns. Compressibility and magnetic susceptibility are determined from the measured fluctuations. This new sensitive method easily resolves a tenfold suppression of spin fluctuations below shot noise due to pairing, and can be applied to novel magnetic phases in optical lattices.

DOI: 10.1103/PhysRevLett.106.010402

PACS numbers: 05.30.Fk, 03.75.Ss, 67.85.Lm

One frontier in the field of ultracold atoms is the realization of quantum systems with strong interactions and strong correlations. Many properties of strongly correlated systems cannot be deduced from mean density distributions. This has drawn interest toward novel ways of probing cold atoms, e.g., via rf spectroscopy [1,2], Bragg and Raman scattering [3], interferometric methods [4,5], and by recording density correlations [6–8]. Further insight into quantum systems is obtained by looking not only at expectation values, but also at fluctuations. Several recent studies looked at density fluctuations, either of bosons around the Mott insulator transition [9–11], or of a gas of noninteracting fermions [12,13].

In this Letter, we extend the study of fluctuations of ultracold gases in several ways. First, we introduce the technique of speckle imaging as a simple and highly sensitive method to characterize fluctuations. Second, we apply it to a two-component Fermi gas across the Bose-Einstein condensate (BEC)-BCS crossover. Third, we directly measure fluctuations in the magnetization, i.e., the difference of the densities in the two different spin components, bypassing the need to measure the individual densities separately.

Our work is motivated by the prospect of realizing wide classes of spin Hamiltonians using a two-component gas of ultracold atoms in an optical lattice [14,15]. An important thermodynamic quantity to characterize two-component systems is the spin susceptibility, which provides a clear signature of phase transitions or crossovers involving the onset of pairing or magnetic order [16–19]. At a ferromagnetic phase transition the susceptibility diverges, whereas in a transition to a paired or antiferromagnetic phase the susceptibility becomes exponentially small in the ratio of the pair binding energy (or antiferromagnetic gap) to the temperature. The fluctuation-dissipation theorem relates response functions to fluctuations, consequently the spin susceptibility can be determined by measuring the fluctuations in the relative density of the two spin components.

In our experiment, we image the atom clouds using light detuned from resonance so that each atom's real

polarizability, which contributes to the refractive index, is much larger than its imaginary polarizability, which contributes to absorption. Since the detunings for the two spin states are different, spin fluctuations lead to fluctuations in the local refractive index, resulting in phase shifts of the imaging light that vary randomly in space. We measure these phase shifts by imaging the resulting speckle patterns.

These speckle patterns are created by propagation, which converts the spatially varying phase shifts of the imaging light into an intensity pattern on our detector without the use of a phase plate. Spin and density fluctuations occur on all spatial scales down to the interatomic separation; the smallest observable fluctuations have a wavelength equal to the imaging system's maximum resolution. In our system that length has a Rayleigh range, and hence a depth of field, smaller than the cloud size, so the recorded image is necessarily modified by propagation effects. Propagation mixes up amplitude and phase signals [Fig. 1]. This can be easily seen in the case of a phase grating, which creates an interference pattern further downstream; after propagating for a distance equal to the Rayleigh range of the grating spacing, the imprinted phase is converted into an amplitude pattern. This feature of speckle makes our imaging technique both simple and robust. It is insensitive against defocusing, and allows us to image fluctuations of the real part of the refractive index (i.e., a phase signal) without a phase plate or other Fourier optics.

Similar physics is responsible for laser speckle when a rough surface scatters light with random phases [20], and occurs when a Bose-Einstein condensate with phase fluctuations develops density fluctuations during expansion [21], or when a phase-contrast signal is turned into an amplitude signal by deliberate defocusing [22].

The experiments were performed with typically  $10^6$   $^6\text{Li}$  atoms in each of the two lowest hyperfine states  $|1\rangle$  and  $|2\rangle$  confined in an optical dipole trap oriented at  $45^\circ$  to the imaging axis with radial and axial trap frequencies  $\omega_r = 2\pi \times 108.9(6) \text{ s}^{-1}$  and  $\omega_z = 2\pi \times 7.75(3) \text{ s}^{-1}$ . For the

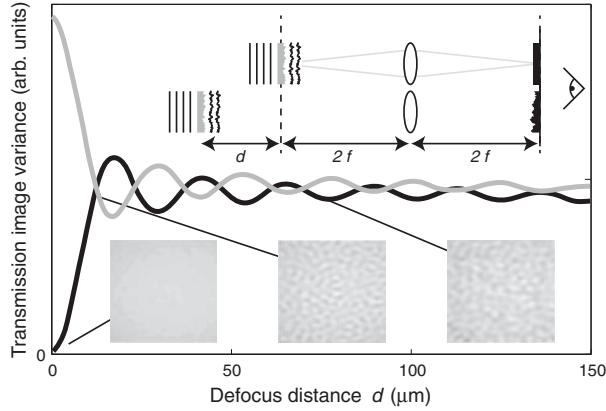


FIG. 1. Simulation of propagation effects after light has passed through a Poissonian phase noise object. Shown are the variance measured in the amplitude or in-phase quadrature (black line) and the out-of-phase quadrature (gray line) as a function of defocus distance, for an imaging system with a numerical aperture of 0.14. Within a distance less than 5% of our cloud size, noise becomes equally distributed between the two quadratures and the variances in transmission and phase-contrast images become the same. (Top inset) For small phase fluctuations, an in-focus phase noise object gives no amplitude contrast, but when it is out of focus it does. (Bottom inset) Sample intensity patterns for a defocused phase object.

samples imaged at 527 G, the sample preparation was similar to that described in [13], with a temperature of  $0.14(1)T_F$ . The samples imaged at other magnetic fields were prepared in a similar fashion, except that evaporation was performed at 1000 G to a final temperature of  $T = 0.13(1)T_F$  before ramping the magnetic field over 1.5 s to its final value. The temperature at 1000 G was determined by fitting a noninteracting Thomas-Fermi distribution in time of flight. The temperatures at other points in the crossover were related to that value assuming an isentropic ramp, using calculations presented in [23]. Using this method we obtain temperatures of  $0.13(1)T_F$  at 915 G,  $0.19(1)T_F$  at 830 G, and  $0.19(3)T_F$  at 790 G where additional evaporation was performed to achieve a central optical density similar to that at the other magnetic fields. The extent of the cloud along the imaging direction was  $135 \mu\text{m}$ , much larger than the Rayleigh range of  $8 \mu\text{m}$  for our imaging system with a NA of 0.14.

The superfluid to normal phase boundary was determined by measuring condensate fraction [Fig. 2] using the standard magnetic field sweep technique [24,25]. For this, the magnetic field was rapidly switched to 570 G to transfer atom pairs to more deeply bound pairs (molecules) which survive ballistic expansion. For resonant imaging of the molecules, the field was ramped back to 790 G over 10 ms. The condensate fraction was determined by fitting the one-dimensional density profiles with a bimodal distribution.

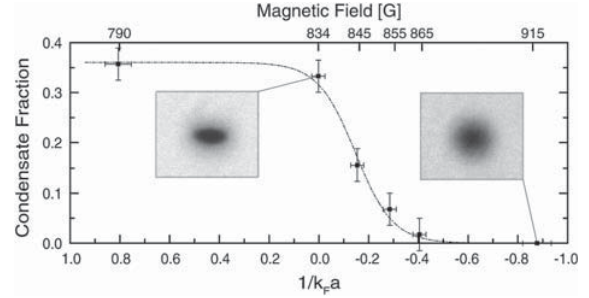


FIG. 2. Measured condensate fraction as a function of dimensionless interaction strength  $1/(k_F a)$ . Insets show typical images from which the condensate fraction was extracted by fitting a bimodal distribution. The dashed line is a sigmoidal fit to guide the eye.

As previously described, propagation converts spatial fluctuations in the refractive index into amplitude fluctuations on the detector. For different choices of the probe light frequency, the two atomic spin states will have different real polarizabilities and the local refractive index will be a different linear combination of the (line-of-sight integrated) column densities  $n_1$  and  $n_2$ . To measure the susceptibility we choose a probe light frequency exactly between the resonances for states  $|1\rangle$  and  $|2\rangle$ , so that the real polarizabilities are opposite and the refractive index is proportional to the magnetization ( $n_1 - n_2$ ). The intensity fluctuations on the detector after propagation are consequently proportional to the fluctuations in magnetization. Since a refractive index proportional to  $(n_1 + n_2)$  occurs only in the limit of infinite detuning, we measure the fluctuations in the total density by exploiting the fact that the fluctuations in total density can be inferred from the fluctuations in two different linear combinations of  $n_1$  and  $n_2$ . For convenience, we obtain the second linear combination using a detuning that has the same value, but opposite sign for state  $|2\rangle$ , and therefore three times the value for state  $|1\rangle$ . With this detuning, we record images of the fluctuations in  $(n_1/3 + n_2)$ .

In principle, this information can be obtained by taking separate absorption images on resonance for states  $|1\rangle$  and  $|2\rangle$ . However, the images would have to be taken on a time scale much faster than that of atomic motion and there would be increased technical noise from the subtraction of large numbers. The use of dispersive imaging has the additional advantage over absorption in that the number of scattered photons in the forward direction is enhanced by superradiance. As a result, for the same amount of heating, a larger number of signal photons can be collected [26]. This is crucial for measuring atomic noise, which requires the collection of several signal photons per atom. The choice of detuning between the transitions of the two states has the important feature that the index of refraction for an equal mixture fluctuates around zero, avoiding any lensing and other distortions of the probe beam. This is not

the case for other choices of detuning, and indeed, we observe some excess noise in those images (see below). At the detunings chosen, 10% residual attenuation is observed, some due to off-resonant absorption, some due to dispersive scattering of light out of the imaging system by small scale density fluctuations. The contribution to the variance of the absorption signal relative to the dispersive signal scales as  $(2\Gamma)^2/\delta^2 \approx 0.006$  and can be neglected in the interpretation of the data.

The noise analysis procedure was nearly identical to that performed in [13]. A high-pass filter with a cutoff wavelength of 13  $\mu\text{m}$  was applied to each image of the cloud to minimize the effect of fluctuations in total atom number. Then, for each pixel position, the variance of the optical densities at that position in the different images was computed. After the subtraction of the contribution of photon shot noise, the resulting variance image reflects the noise contribution from the atoms.

The goal of our noise measurements is to determine at various interaction strengths the normalized susceptibility  $\tilde{\chi} = \chi/\chi_0$  and compressibility  $\tilde{\kappa} = \kappa/\kappa_0$ , where  $\chi_0 = 3n/2E_F$  and  $\kappa_0 = 3/2nE_F$  are the susceptibility and compressibility of a zero-temperature noninteracting Fermi gas with the same total density  $n$  and Fermi energy  $E_F$ . Before studying spin fluctuations through the BEC-BCS crossover, we therefore calibrate our measurement by measuring the spin fluctuations in a noninteracting mixture, realized at 527 G where the scattering length between the two states vanishes. Figure 3 shows raw profiles of the variances  $\Delta_-^2$  and  $\Delta_+^2$  measured at the two detunings. These fluctuations in the speckle pattern are proportional to number fluctuations in the specified probe volume  $V$ :  $\Delta_-^2 = [c\Delta(N_1 - N_2)]^2$  and  $\Delta_+^2 = [c'\Delta(N_1/3 + N_2)]^2$ . In these relations  $c$  and  $c'$  are factors which have to be calibrated. Without interactions,  $N_1$  and  $N_2$  are uncorrelated, and one predicts  $[\Delta(N_1 - N_2)]^2/[\Delta(N_1/3 + N_2)]^2 = 2/[1 + (1/3)^2] = 1.8$ .

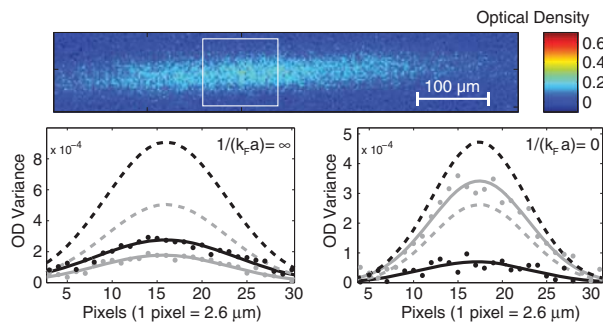


FIG. 3 (color online). (Top panel) Example speckle noise image, with white box indicating analysis region. (Bottom panels) Noise data for noninteracting (left panel) and resonantly interacting (right panel) cold clouds, showing  $\Delta_-^2$  (black dots) and  $\Delta_+^2$  (gray dots). Solid lines are Gaussian fits to the data, and dotted lines illustrate the expected full Poissonian noise for the corresponding quantities based on density determined from off-resonant absorption.

The observed ratio of  $\Delta_-^2/\Delta_+^2 = 1.56(14)$  reflects excess noise contributing to  $\Delta_+^2$  due to residual systematic dispersive effects and is accounted for by setting  $c'/c = \sqrt{1.8/1.56}$ . For high temperatures, the atomic noise of the noninteracting gas approaches shot noise; for lower temperatures we observe a reduction in noise due to Pauli blocking as in our previous work [13]. With our new method, we easily discern spin fluctuations with a variance of less than 10% of atom shot noise.

The fluctuation-dissipation theorem connects the variances  $[\Delta(N_1 - N_2)]^2$  and  $[\Delta(N_1 + N_2)]^2$  to the susceptibility  $\tilde{\chi}$  and the compressibility  $\tilde{\kappa}$  via  $[\Delta(N_1 - N_2)]^2 = 3N/2(T/T_F)\tilde{\chi}$  and  $[\Delta(N_1 + N_2)]^2 = 3N/2(T/T_F)\tilde{\kappa}$  with  $N = N_1 + N_2$  and  $T/T_F$  being the temperature measured in units of the Fermi temperature  $T_F$ . Recomposing the variances from the two experimentally accessible linear combinations these relations become  $\Delta_-^2/Nc^2 = 3/2(T/T_F)\tilde{\chi}$  and  $9/4\Delta_+^2/Nc'^2 - 1/4\Delta_-^2/Nc^2 = 3/2(T/T_F)\tilde{\kappa}$ . The constants  $c$  and  $c'$  are determined using the noise measurements at 527 G for a noninteracting Fermi gas for which  $\tilde{\chi} = \tilde{\kappa} = 1 + O((T/T_F)^2)$ . This analysis ignores line-of-sight integration corrections.

Figure 4 shows the spin susceptibility, the compressibility, and the ratio between the two quantities for the interacting mixtures as the interaction strength is varied through the BEC-BCS crossover. The susceptibility and compressibility reproduce the expected qualitative behavior: for the sample at unitarity, where the transition temperature is sufficiently high that a sizable portion of the sample is superfluid, and for the sample on the BEC side, the spin susceptibility is strongly suppressed relative to the compressibility. This reflects the fact that the atoms form bound

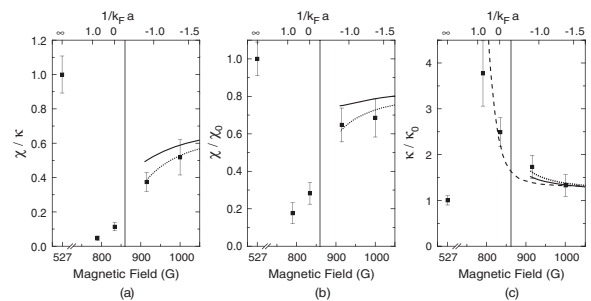


FIG. 4. (a) The ratio  $\chi/\kappa$ , (b) the normalized susceptibility  $\chi/\chi_0$ , and (c) the normalized compressibility  $\kappa/\kappa_0$  in the BEC-BCS crossover. The variances derived from sequences of images are converted into thermodynamic variables using the measured temperatures and a calibration factor determined from the noninteracting gas. The vertical line indicates the onset region of superfluidity, as determined via condensate fraction measurements. The curves show theoretical zero temperature estimates based on 1st (dotted) and 2nd order (solid) perturbative formulas obtained from Landau's Fermi-liquid theory integrated along the line of sight, and results from a Monte Carlo calculation (dashed) for the compressibility in a homogeneous system [32].

molecules or generalized Cooper pairs; the spin susceptibility should be exponentially small in the binding energy, while the enhanced compressibility reflects the bosonic character of the molecular condensate. At 915 G and 1000 G, where the sample is above the superfluid critical temperature, the susceptibility is larger but still below its value for the noninteracting gas, reflecting the persistence of pair correlations even in the normal phase of the gas.

Above the Feshbach resonance, for attractive interactions, we compare our results to first and second order perturbation theory in the small parameter  $k_F a$ . This ignores the instability to the superfluid BCS state at exponentially small temperatures. The perturbation theory is formulated for the Landau parameters for a Fermi liquid [16,27]. The susceptibility and compressibility are given by  $\chi_0/\chi = (1 + F_0^a)m/m^*$ ,  $\kappa_0/\kappa = (1 + F_0^s)m/m^*$ , where  $m^* = m(1 + F_1^s/3)$  is the effective mass, and  $F_l^s$ ,  $F_l^a$  are the  $l$ th angular momentum symmetric and antisymmetric Landau parameters, respectively. Although the experimental data are taken for relatively strong interactions outside the range of validity for a perturbative description, the predictions still capture the trends observed in the normal phase above the Feshbach resonance. This shows that more accurate measurements of the susceptibility, and a careful study of its temperature dependence, are required to reveal the presence of a possible pseudogap phase.

In our analysis we have neglected quantum fluctuations which are present even at zero temperature [16,28]. They are related to the large- $q$  static structure factor  $S(q)$  measured in [29] and proportional to the surface of the probe volume, scaling with  $N^{2/3} \log(N)$ . For fluctuations of the total density, their relative contribution is roughly  $N^{-1/3}/(T/T_F)$ , and at most 40% for our experimental parameters. Attractive interactions and pairing suppress both the thermal and quantum spin fluctuations, but it is not known at what temperature quantum fluctuations become essential.

Spin susceptibilities can also be obtained from the equation of state which can be determined by analyzing the average density profiles of imbalanced mixtures [30]. Our method has the advantage of being applicable without imbalance, and requires only local thermal equilibrium. Moreover fluctuations can be compared with susceptibilities determined from the equation of state to perform absolute, model-independent thermometry for strongly interacting systems [31].

In conclusion, we have demonstrated a new technique to determine spin susceptibilities of ultracold atomic gases using speckle imaging. We have validated and calibrated this technique using an ideal Fermi gas and applied it to a strongly interacting Fermi gas in the BEC-BCS crossover. This technique is directly applicable to studying pairing and magnetic ordering of two-component gases in optical lattices.

We acknowledge Qijin Chen and Kathy Levin for providing calculations of condensate fraction, Gregory Astrakharchik and Stefano Giorgini for providing Monte Carlo results for the compressibility, Sandro Stringari and Alessio Recati for discussions, and Yong-il Shin for experimental assistance. This work was supported by NSF and the Office of Naval Research, AFOSR (through the MURI program), and under Army Research Office Grant No. W911NF-07-1-0493 with funds from the DARPA Optical Lattice Emulator program.

- 
- [1] S. Gupta *et al.*, *Science* **300**, 1723 (2003).
  - [2] C. A. Regal and D. S. Jin, *Phys. Rev. Lett.* **90**, 230404 (2003).
  - [3] J. Stenger *et al.*, *Phys. Rev. Lett.* **82**, 4569 (1999).
  - [4] T. Kitagawa *et al.*, *arXiv:1001.4358*.
  - [5] Z. Hadzibabic, S. Stock, B. Battelier, V. Bretin, and J. Dalibard, *Phys. Rev. Lett.* **93**, 180403 (2004).
  - [6] T. Jeltes *et al.*, *Nature (London)* **445**, 402 (2007).
  - [7] T. Rom *et al.*, *Nature (London)* **444**, 733 (2006).
  - [8] M. Greiner *et al.*, *Phys. Rev. Lett.* **94**, 110401 (2005).
  - [9] N. Gemelke *et al.*, *Nature (London)* **460**, 995 (2009).
  - [10] W. S. Bakr *et al.*, *Science* **329**, 547 (2010).
  - [11] J. F. Sherson *et al.*, *Nature (London)* **467**, 68 (2010).
  - [12] T. Müller *et al.*, *Phys. Rev. Lett.* **105**, 040401 (2010).
  - [13] C. Sanner *et al.*, *Phys. Rev. Lett.* **105**, 040402 (2010).
  - [14] L.-M. Duan, E. Demler, and M. D. Lukin, *Phys. Rev. Lett.* **91**, 090402 (2003).
  - [15] A. B. Kuklov and B. V. Svistunov, *Phys. Rev. Lett.* **90**, 100401 (2003).
  - [16] A. Recati and S. Stringari, *arXiv:1007.4504*.
  - [17] G. M. Bruun *et al.*, *Phys. Rev. Lett.* **102**, 030401 (2009).
  - [18] N. Trivedi and M. Randeria, *Phys. Rev. Lett.* **75**, 312 (1995).
  - [19] C.-C. Chien and K. Levin, *Phys. Rev. A* **82**, 013603 (2010).
  - [20] J. W. Goodman, *Speckle Phenomena in Optics* (Ben Roberts and Company, Greenwood Village, CO, 2007).
  - [21] D. Hellweg *et al.*, *Phys. Rev. Lett.* **91**, 010406 (2003).
  - [22] L. D. Turner *et al.*, *Opt. Lett.* **29**, 232 (2004).
  - [23] Q. Chen, J. Stajic, and K. Levin, *Phys. Rev. Lett.* **95**, 260405 (2005).
  - [24] M. Greiner *et al.*, *Nature (London)* **426**, 537 (2003).
  - [25] M. W. Zwierlein *et al.*, *Phys. Rev. Lett.* **91**, 250401 (2003).
  - [26] W. Ketterle, D. S. Durfee, and D. M. Stamper-Kurn, in *Proceedings of the International School of Physics Enrico Fermi, Varenna, 1998* (IOS, Amsterdam, 1999).
  - [27] E. M. Lifshitz and L. P. Pitaevskii, *Statistical Physics Part 2, 3rd ed.*, Course of Theoretical Physics Vol. 9 (Pergamon Press Inc., Oxford, 1980);
  - [28] G. E. Astrakharchik, R. Combescot, and L. P. Pitaevskii, *Phys. Rev. A* **76**, 063616 (2007).
  - [29] E. D. Kuhnle *et al.*, *Phys. Rev. Lett.* **105**, 070402 (2010).
  - [30] C. Salomon (private communication).
  - [31] D. McKay and B. DeMarco, *arXiv:1010.0198*.
  - [32] G. E. Astrakharchik, J. Boronat, J. Casulleras, and S. Giorgini, *Phys. Rev. Lett.* **93**, 200404 (2004).

## Appendix C

# Correlations and Pair Formation in a Repulsively Interacting Fermi Gas

This appendix contains a printout of *Phys. Rev. Lett.* 108, 240404 (2012): Christian Sanner, Edward J. Su, Wujie Huang, Aviv Keshet, Jonathon Gillen, and Wolfgang Ketterle, *Correlations and Pair Formation in a Repulsively Interacting Fermi Gas*.

## Correlations and Pair Formation in a Repulsively Interacting Fermi Gas

Christian Sanner, Edward J. Su, Wujie Huang, Aviv Keshet, Jonathon Gillen, and Wolfgang Ketterle

MIT-Harvard Center for Ultracold Atoms, Research Laboratory of Electronics, and Department of Physics,  
Massachusetts Institute of Technology, Cambridge, Massachusetts 02139, USA

(Received 9 August 2011; published 13 June 2012)

A degenerate Fermi gas is rapidly quenched into the regime of strong effective repulsion near a Feshbach resonance. The spin fluctuations are monitored using speckle imaging and, contrary to several theoretical predictions, the samples remain in the paramagnetic phase for an arbitrarily large scattering length. Over a wide range of interaction strengths a rapid decay into bound pairs is observed over times on the order of  $10\hbar/E_F$ , preventing the study of equilibrium phases of strongly repulsive fermions. Our work suggests that a Fermi gas with strong short-range repulsive interactions does not undergo a ferromagnetic phase transition.

DOI: 10.1103/PhysRevLett.108.240404

PACS numbers: 03.75.Ss, 67.85.Lm, 75.10.Lp

Many-body systems can often be modeled using contact interactions, greatly simplifying the analysis while maintaining the essence of the phenomenon to be studied. Such models are almost exactly realized with ultracold gases due to the large ratio of the de Broglie wavelength to the range of the interatomic forces [1]. For itinerant fermions with strong short-range repulsion, textbook calculations predict a ferromagnetic phase transition—the so-called Stoner instability [2].

Here we investigate this system using an ultracold gas of fermionic lithium atoms, and observe that the ferromagnetic phase transition does not occur. A previous experimental study [3] employing a different apparatus found indirect evidence for a ferromagnetic phase, but did not observe the expected domain structure, possibly due to the lack of imaging resolution. Here we address this shortcoming by analyzing density and spin density fluctuations via speckle imaging [4]. When spin domains of  $m$  atoms form, the spin density variance will increase by a factor of  $m$  [5], even if individual domains are not resolved. One main result of this paper is the absence of such a significant increase which seems to exclude the possibility of a ferromagnetic state in the studied system.

The Stoner model assumes a two-component Fermi gas with a repulsive short-range interaction described by a single parameter, the scattering length. The predicted phase transition to a ferromagnetic state requires large repulsive scattering lengths on the order of the interatomic spacing. They can be realized only by short-range *attractive* potentials with a loosely bound state with binding energy  $\hbar^2/(ma^2)$ , with  $m$  being the atomic mass and  $a$  being the scattering length [6]. However, as shown schematically in Fig. 1, the repulsive gas is then by necessity only metastable with respect to decay into the bound state. Many theoretical studies of a Fermi gas with strong short-range repulsive interactions assume that the metastable state is sufficiently long-lived [7–18]. In recent Monte Carlo simulations, the paired state is projected out in the

time evolution of the system [19,20]. Theoretical studies concluded that the pairing instability is somewhat faster than the ferromagnetic instability [21]. The second major result of this paper is to show that pair formation occurs indeed on a very short time scale. The measured time constant of  $10\hbar/E_F$  (where  $E_F$  is the Fermi energy) indicates that the metastable repulsive state will never reach equilibrium and that, even in a metastable sense, a Fermi gas with strong short-range repulsive interactions does not exist. The fast pair formation could not be observed previously due to limited time resolution [3]. Instead, a much slower second phase in the conversion of atoms to pairs was observed leading to the wrong conclusion that the unpaired atoms have a much longer lifetime.

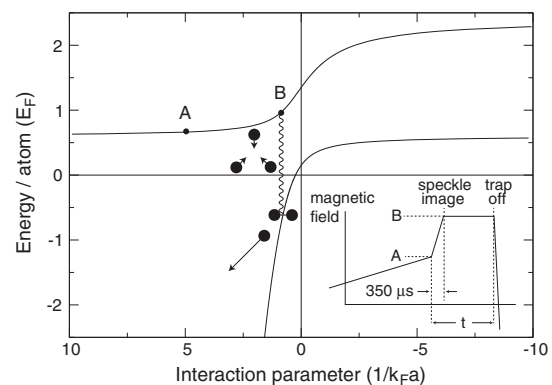


FIG. 1. Diagram showing energy levels and timing of the experiment. The upper (repulsive) and lower (attractive) branch energies, near a Feshbach resonance, are connected by three-body collisions. In our experiment, we quickly jump from a weakly interacting Fermi gas (A) to a strongly interacting one (B) with a rapid magnetic field change. The evolution of correlations and domains and the molecule formation (population of the lower branch) are studied as a function of hold time  $t$ . Adapted from [42].

The experiments were carried out with typically  $4.2 \times 10^5$   $^6\text{Li}$  atoms in each of the two lower spin states  $|1\rangle$  and  $|2\rangle$  confined in an optical dipole trap with radial and axial trap frequencies  $\omega_r = 2\pi \times 100(1) \text{ s}^{-1}$  and  $\omega_z = 2\pi \times 9.06(25) \text{ s}^{-1}$ . The sample was evaporatively cooled at a magnetic bias field  $B = 320 \text{ G}$ , identical to the procedure described in [22]. Then the magnetic field was slowly ramped to  $730 \text{ G}$  ( $k_F a = 0.35$ ) in  $500 \text{ ms}$ . The fraction of atoms being converted to molecules during the ramp was measured (see below for method) to be below  $5\%$ . The temperature of the cloud was typically  $0.23(3)T_F$  at  $527 \text{ G}$  with a Fermi energy of  $E_F = k_B T_F = h \times 6.1 \text{ kHz}$ . After rapidly switching the magnetic field from  $730 \text{ G}$  to the final value in less than  $350 \mu\text{s}$ , spin fluctuations were measured by speckle imaging. Optionally an appropriate rf pulse was applied directly before imaging to rotate the spin orientation along the measurement axis. Due to the use of  $20 \text{ cm}$  diameter coils outside the vacuum chamber, the inductance of the magnet coils was  $330 \mu\text{H}$  and the fast switching was accomplished by rapidly discharging capacitors charged to  $500 \text{ V}$ .

Experimentally, spin fluctuations are measured using the technique of speckle imaging described in Ref. [4]. For an appropriate choice of detuning, an incident laser beam experiences a shift of the refractive index proportional to the difference between the local populations of the two spin states  $N_1$  and  $N_2$ . Spin fluctuations create spatial fluctuations in the local refractive index and imprint a phase pattern into the incoming light, which is then converted into an amplitude pattern during propagation. The resulting spatial fluctuations in the probe laser intensity are used to determine the spin fluctuations in the sample.

In Ref. [4] we prepared samples on the lower branch of the Feshbach resonance, where positive values of  $k_F a$  correspond to a gas of weakly bound molecules. At  $k_F a = 1.2$ , we observed a sixfold suppression of spin fluctuations and a fourfold enhancement of density fluctuations. Typical fluctuations in the speckle images of a non-interacting Fermi gas at  $T = 0.23T_F$  amount to  $5\%$  of the average optical signal per pixel, corresponding to about  $50\%$  of Poissonian fluctuations. Those fluctuations are modified by factors between  $0.2$  and  $1.6$  due to pairing and interactions.

In this study, on the upper branch of the Feshbach resonance, the situation is reversed. For unbound atoms, as the interaction strength increases, the two spin components should develop stronger and stronger anticorrelations and enhanced spin fluctuations. Previous experimental work [3] and several theoretical studies [10,11,13–15,18,23] predicted a phase transition to a ferromagnetic state where the magnetic susceptibility and therefore the spin fluctuations diverge. Recent Monte Carlo simulations [19] predict such a divergence around  $k_F a = 0.83$ . We therefore expected an increase of spin fluctuations by one or several orders of magnitude, related to the size of magnetic domains.

Figure 2 shows the observed spin fluctuations enhancement compared to the non-interacting cloud at  $527 \text{ G}$ . The variance enhancement factor reaches its maximum value of  $1.6$  immediately after the quench, decreasing during the  $2 \text{ ms}$  afterward. The absence of a dramatic increase shows that no domains form and that the sample remains in the paramagnetic phase throughout. Similar observations were made for a wide range of interaction strengths and wait times. Note that first-order perturbation theory [24] predicts an increase of the susceptibility by a factor of  $1.5$  at  $k_F a = 0.5$  and by a factor of  $2$  at  $k_F a = 0.8$  (i.e., no dramatic increase for  $k_F a < 1$ ). Therefore, our data show no evidence for the Fermi gas approaching the Stoner instability.

Before we can fully interpret these findings, we have to take into account the decay of the atomic sample on the upper branch of the Feshbach resonance into bound pairs. We characterize the pair formation by comparing the total number of atoms and molecules  $N_a + 2N_{\text{mol}}$  (determined by taking an absorption image after ballistic expansion at high magnetic field where molecules and atoms have the same absorption resonance) to the number of free atoms (determined by rapidly sweeping the magnetic field to  $5 \text{ G}$  before releasing the atoms and imaging the cloud, converting pairs into deeply bound molecules that are completely shifted out of resonance) [25].

The time evolution of the molecule production (Fig. 3) shows two regimes of distinct behavior. For times less than  $1 \text{ ms}$ , we observe a considerable number of atoms converted into molecules, while the total number  $N_a + 2N_{\text{mol}}$  remains constant. The initial drop in atom number becomes larger as we increase the final magnetic field, and saturates at around  $50\%$  near the Feshbach resonance.

We attribute this fast initial decay in atom number to recombination [26,27] into the weakly bound molecular

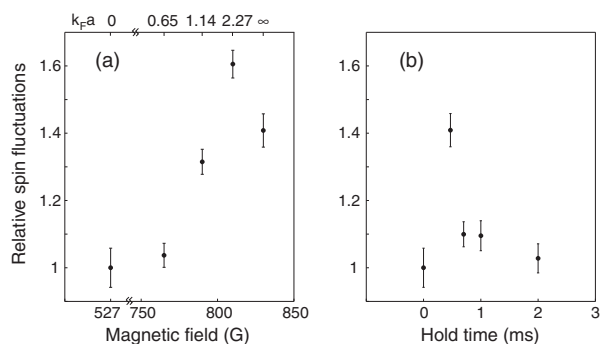


FIG. 2. Spin fluctuations (a) after  $350 \mu\text{s}$  as a function of magnetic field and (b) on resonance as a function of hold time scaled to the value measured at  $527 \text{ G}$ . Even at strong repulsive interactions, the measured spin fluctuations are barely enhanced, indicating only short-range correlations and no domain formation. The spin fluctuations were determined for square bins of  $2.6 \mu\text{m}$ , each containing on average 1000 atoms per spin state.

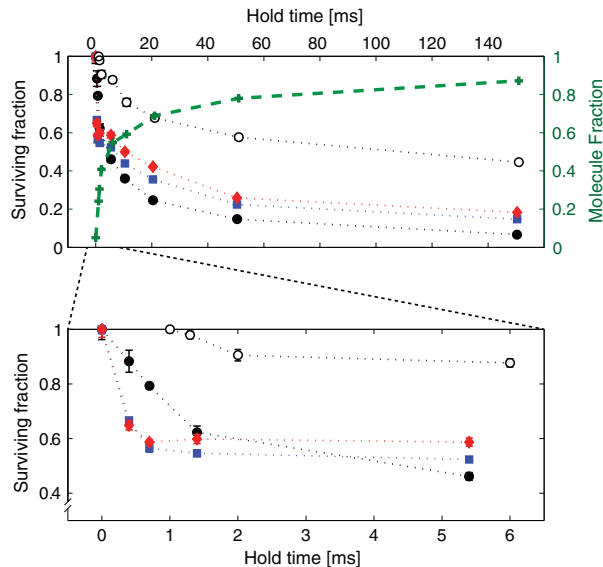


FIG. 3 (color online). Characterization of molecule formation at short and long hold times, and at different values of the interaction strength. The closed symbols, circles (black) at 790 G with  $k_F a = 1.14$ , squares (blue) at 810 G with  $k_F a = 2.27$  and diamonds (red) at 818 G with  $k_F a = 3.5$  represent the normalized number of free atoms, the open symbols the total number of atoms including those bound in Feshbach molecules (open circles at 790 G with  $k_F a = 1.14$ ). The crosses (green) show the molecule fraction. The characteristic time scale is set by the Fermi time  $\hbar/E_F = 43 \mu\text{s}$ , calculated with a cloud averaged Fermi energy.

state. We obtain an atom loss rate  $\dot{N}_a/N_a = 250 \text{ s}^{-1}$  at 790 G in the first 1 ms after the magnetic field switch. Assuming a three-body process we estimate the rate coefficient  $L_3$  at this field to be  $3.9 \times 10^{-22} \text{ cm}^6 \text{ s}^{-1}$ , though the interaction is already sufficiently strong for many-body effects to be significant. For stronger interactions, about 30% of atom loss occurs already during the relevant 100  $\mu\text{s}$  of ramping through the strongly interacting region, indicating a lower bound of around  $3 \times 10^3 \text{ s}^{-1}$  for the loss rate which is 13% of the inverse Fermi time  $E_F/\hbar$ , calculated with a cloud averaged Fermi energy.

After the first millisecond, the molecule formation rate slows down, by an order of magnitude at a magnetic field of 790 G (and even more dramatically at higher fields) when it reaches about 50%. It seems likely that the molecule fraction has reached a quasi-equilibrium value at the local temperature, which is larger than the initial temperature due to local heating accompanying the molecule formation. Reference [28] presents a simple model for the equilibrium between atoms and molecules (ignoring strong interactions). For phase space densities around unity and close to resonance, the predicted molecule fraction is 0.5, in good agreement with our observations [29].

For longer time scales (hundred milliseconds) we observe a steady increase of the molecule fraction to 90% for the longest hold time. This occurs due to continuous evaporation which cools down the system and shifts the atom-molecule equilibrium towards high molecule fractions. During the same time scale, a slow loss in both atom number and total number is observed caused by inelastic collisions (vibrational relaxation of molecules) and evaporation loss.

Is the rapid conversion into molecules necessarily faster than the evolution of ferromagnetic domains? Our answer is tentatively yes. First, for strong interactions with  $k_F a$  around 1, one expects both instabilities (pair formation and Stoner instability) to have rates which scale with the Fermi energy  $E_F$  and therefore with  $n^{2/3}$ . Therefore, one cannot change the competition between the instabilities by working at higher or lower densities. According to Ref. [21] the fastest unstable modes for domain formation have a wave vector  $q \approx k_F/2$  and grow at a rate of up to  $E_F/4\hbar$  when the cloud is quenched sufficiently far beyond the critical interaction strength. Unstable modes with such wave vectors will develop “domains” of half a wavelength or size  $\xi = \pi/q = 2\pi/k_F$  containing 5 atoms per spin state in a volume  $\xi^3$ . This rate is comparable to the observed conversion rates into pairs of  $0.13E_F$ . Therefore, at best, “domains” of a few particles could form, but before they can grow further and prevent the formation of pairs (in a fully polarized state), rapid pair formation takes over and populates the lower branch of the Feshbach resonance. Based on our observations and these arguments, it seems that it is not possible to realize ferromagnetism with strong short range interaction, and therefore the basic Stoner model cannot be realized in nature.

One possibility to suppress pair formation is provided by narrow Feshbach resonances. Here the pairs have dominantly closed channel character and therefore a much smaller overlap matrix element with the free atoms. However, narrow Feshbach resonances are characterized by a long effective range and do not realize the Stoner model which assumes short-range interactions. Other interesting topics for future research on ferromagnetism and pair formation include the effects of dimensionality [30,31], spin imbalance [32,33], mass imbalance [34], lattice and band structure [35,36].

We now discuss whether ferromagnetism is possible *after* atoms and molecules have rapidly established local equilibrium. In other words, starting at  $T = 0$ , one could heat up the fully paired and superfluid system and create a gas of atomic quasiparticles which are similar to free atoms with repulsive interactions. Density and temperature of the atoms are now coupled. It is likely that such a state is realized in our experiments after a few ms following the quench, until evaporative cooling converts the system into a molecular condensate over  $\approx 100$  ms. The possibility that such a quasiparticle gas could become ferromagnetic

has not been discussed in the literature. Our experiments do not reveal any major increase in spin fluctuations which seems to exclude a ferromagnetic state. In the simplest picture, we could regard the atomic quasiparticles as free atoms, and then apply the Stoner model to them. Ferromagnetic domain formation is analogous to phase separation between the two spin components [3]. Since dimers interact equally with the two spin components, one might expect that even a noticeable dimer fraction should not suppress the tendency of the atomic gas to form domains. Therefore, in a simple model, one may neglect dimer-atom interactions.

If the Stoner model applies to this quasiparticle gas, the next question is whether the temperature is low enough for the ferromagnetic phase transition. Available theoretical treatments do not predict an exact maximum transition temperature to the ferromagnetic state and obtain an unphysical divergence for large scattering lengths. Since the only energy scale is the Fermi temperature, one would expect a transition temperature which is a fraction of the Fermi temperature [37], higher or around the temperature scale probed in our experiments. However, even above the transition temperature, the susceptibility is enhanced. A simple Weiss mean field or Stoner model leads to the generic form of the susceptibility  $\chi(T) = \chi_0(T)/(1 - w\chi_0(T))$ , where  $\chi_0(T)$  is the Pauli susceptibility of the non-interacting gas and  $w$  the interaction parameter. This formula predicts a twofold increase in the susceptibility even 50% above the transition temperature, which is well within the sensitivity of our measurements.

Therefore, our experiment can rule out ferromagnetism for temperatures even slightly lower than the experimental temperatures. Temperatures are very difficult to measure in a transient way for a dynamic system which may not be in full equilibrium. For example, cloud thermometry requires full equilibration and lifetimes much longer than the longest trap period. We attempted to measure the temperature after the hold time near the Feshbach resonance by quickly switching the magnetic field to weak interactions at 527 G and then performing noise thermometry using speckle imaging [4]. We measure column-integrated fluctuations that are 0.61(8) of the Poisson value which implies an effective temperature well below  $T_F$ , around 0.33(7)  $T_F$ , not much higher than our initial temperature of 0.23  $T_F$ . Although the cloud is not in full equilibrium, an effective local temperature can still be obtained from noise thermometry.

Alternatively, we can estimate the temperature increase from the heat released by pair formation. A simple model [38] accounting for the relevant energy contributions predicts for  $k_F a = 1$  that molecule fractions of higher than 20% result in a final temperature above 0.4  $T_F$ , an estimate which is higher than the measurement reported above. One may hope that closer to resonance many-body

effects lower the released energy; however, as we show in the Supplemental Material (Fig. 1 of [38]) this is not necessarily the case due to the repulsive interaction energy.

Our experiment has not shown any evidence for a possible ferromagnetic phase in an atomic gas in “chemical” equilibrium with dimers. This implies one of the following possibilities. (i) This gas can be described by a simple Hamiltonian with strong short range repulsion. However, this Hamiltonian does not lead to ferromagnetism. This would be in conflict with the results of recent quantum Monte Carlo simulations [19,20] and second order perturbation theory [11], and in agreement with conclusions based on Tan relations [39]. (ii) The temperature of the gas was too high to observe ferromagnetism. This would then imply a critical temperature around or below  $0.2T/T_F$ , lower than generally assumed. (iii) The quasiparticles cannot be described by the simple model of an atomic gas with short-range repulsive interactions due to their interactions with the paired fraction.

A previous experiment [3] reported evidence for ferromagnetism by presenting non-monotonic behavior of atom loss rate, kinetic energy and cloud size when approaching the Feshbach resonance, in agreement with predictions based on the Stoner model. Our measurements confirm that the properties of the gas strongly change near  $k_F a = 1$ . Similar to [3], we observe features in kinetic and release energy measurements near the resonance (see Supplemental Material [38]). However, the behavior is more complex than that captured by simple models. The atomic fraction decays non-exponentially (see Fig. 3), and therefore an extracted decay time will depend on the details of the measurement such as time resolution. Reference [3] found a maximum of the loss rate of  $200 \text{ s}^{-1}$  for a Fermi energy of 28 kHz. Our lower bound of the decay rate of  $3 \times 10^3 \text{ s}^{-1}$  is 15 times faster at a five times smaller Fermi energy. Our more detailed study rules out that Ref. [3] has observed ferromagnetic behavior.

Our conclusion is that an ultracold gas with strong short range repulsive interactions near a Feshbach resonance remains in the paramagnetic phase. The fast formation of molecules and the accompanying heating makes it impossible to study such a gas in equilibrium, confirming predictions of a rapid conversion of the atomic gas to pairs [21,40]. The Stoner criterion for ferromagnetism obtains when the effective interaction strength times the density of states is larger than one. This is a at least an approximately valid criterion for multi-band lattice models [41]. We have shown here that this criterion cannot be applied to Fermi gases with short-range repulsive interactions (the basic Stoner model) since the neglected competition with pairing is crucial.

This work was supported by NSF and ONR, AFOSR MURI, and under ARO Grant No. W911NF-07-1-0493 with funds from the DARPA Optical Lattice Emulator

program. We are thankful to Eugene Demler, David Pekker, Boris Svistunov, Nikolay Prokof'ev, and Wilhelm Zwerger for valuable discussions and to David Weld for critical reading of the manuscript.

- 
- [1] W. Ketterle and M. W. Zwiernlein, in *Proceedings of the International School of Physics "Enrico Fermi,"* Course CLXIV (IOS, Amsterdam, 2007).
- [2] D. W. Snoke, *Solid State Physics: Essential Concepts* (Addison-Wesley, San Francisco, 2008).
- [3] G.-B. Jo, Y.-R. Lee, J.-H. Choi, C. A. Christensen, T. H. Kim, J. H. Thywissen, D. E. Pritchard, and W. Ketterle, *Science* **325**, 1521 (2009).
- [4] C. Sanner, E. J. Su, A. Keshet, W. Huang, J. Gillen, R. Gommers, and W. Ketterle, *Phys. Rev. Lett.* **106**, 010402 (2011).
- [5] This is illustrated by a simplified model assuming Poissonian fluctuations in a given probe volume within the atom sample. With on average  $N$  atoms in this volume, one would measure a standard deviation in the atom number of  $\sqrt{N}$ . However, if the atoms formed clusters each made of  $m$  atoms, the standard deviation of the number of clusters would be  $\sqrt{N/m}$ , leading to a variance in atom number of  $(m\sqrt{N/m})^2 = mN$ .
- [6] Potentials with a positive scattering length  $a$  have no bound state only if the effective range  $r_e$  is larger than  $a/2$ . Otherwise, the  $s$ -wave scattering amplitude  $f(k) = 1/(-1/a + r_e k^2/2 - ik)$  has a pole on the imaginary axis corresponding to a bound state.
- [7] M. Houbiers, R. Ferwerda, H. T. C. Stoof, W. I. McAlexander, C. A. Sackett, and R. G. Hulet, *Phys. Rev. A* **56**, 4864 (1997).
- [8] M. Amoruso, I. Meccoli, A. Minguzzi, and M. P. Tosi, *Eur. Phys. J. D* **7**, 441 (1999).
- [9] L. Salasnich, B. Pozzi, A. Parola, and L. Reatto, *J. Phys. B* **33**, 3943 (2000).
- [10] T. Sogo and H. Yabu, *Phys. Rev. A* **66**, 043611 (2002).
- [11] R. A. Duine and A. H. MacDonald, *Phys. Rev. Lett.* **95**, 230403 (2005).
- [12] H. Zhai, *Phys. Rev. A* **80**, 051605 (2009).
- [13] G. J. Conduit and B. D. Simons, *Phys. Rev. Lett.* **103**, 200403 (2009).
- [14] L. J. LeBlanc, J. H. Thywissen, A. A. Burkov, and A. Paramekanti, *Phys. Rev. A* **80**, 013607 (2009).
- [15] I. Berdnikov, P. Coleman, and S. H. Simon, *Phys. Rev. B* **79**, 224403 (2009).
- [16] X. Cui and H. Zhai, *Phys. Rev. A* **81**, 041602 (2010).
- [17] S. Zhang, H. Hung, and C. Wu, *Phys. Rev. A* **82**, 053618 (2010).
- [18] H. Heiselberg, *Phys. Rev. A* **83**, 053635 (2011).
- [19] S. Pilati, G. Bertainia, S. Giorgini, and M. Troyer, *Phys. Rev. Lett.* **105**, 030405 (2010).
- [20] S.-Y. Chang, M. Randeria, and N. Trivedi, *Proc. Natl. Acad. Sci. U.S.A.* **108**, 51 (2010).
- [21] D. Pekker, M. Babadi, R. Sensarma, N. Zinner, L. Pollet, M. W. Zwiernlein, and E. Demler, *Phys. Rev. Lett.* **106**, 050402 (2011).
- [22] C. Sanner, E. J. Su, A. Keshet, R. Gommers, Y. Shin, W. Huang, and W. Ketterle, *Phys. Rev. Lett.* **105**, 040402 (2010).
- [23] M. Sandri, A. Minguzzi, and F. Toigo, *Europhys. Lett.* **96**, 66004 (2011).
- [24] A. Recati and S. Stringari, *Phys. Rev. Lett.* **106**, 080402 (2011).
- [25] S. Jochim, M. Bartenstein, A. Altmeyer, G. Hendl, C. Chin, J. Hecker Denschlag, and R. Grimm, *Phys. Rev. Lett.* **91**, 240402 (2003).
- [26] C. Chin, R. Grimm, P. Julienne, and E. Tiesinga, *Rev. Mod. Phys.* **82**, 1225 (2010).
- [27] G. J. Conduit and E. Altman, *Phys. Rev. A* **83**, 043618 (2011).
- [28] C. Chin and R. Grimm, *Phys. Rev. A* **69**, 033612 (2004).
- [29] Note that the drop in molecule formation after 1 ms cannot be explained by the drop in atomic density by a factor of 2 due to conversion into molecules and to an increase in the size of the sample due to the increased repulsive interactions.
- [30] N. D. Drummond, N. R. Cooper, R. J. Needs, and G. V. Shlyapnikov, *Phys. Rev. B* **83**, 195429 (2011).
- [31] V. Pietilä, D. Pekker, Y. Nishida, and E. Demler, *Phys. Rev. A* **85**, 023621 (2012).
- [32] X.-J. Liu and H. Hu, *Phys. Rev. A* **82**, 043626 (2010).
- [33] H. Dong, H. Hu, X.-J. Liu, and P. D. Drummond, *Phys. Rev. A* **82**, 013627 (2010).
- [34] C. W. von Keyserlingk and G. J. Conduit, *Phys. Rev. A* **83**, 053625 (2011).
- [35] C.-C. Chang, S. Zhang, and D. M. Ceperley, *Phys. Rev. A* **82**, 061603 (2010).
- [36] G. Carleo, S. Moroni, F. Becca, and S. Baroni, *Phys. Rev. B* **83**, 060411 (2011).
- [37] X.-J. Liu, H. Hu, and P. D. Drummond, *Phys. Rev. A* **82**, 023619 (2010).
- [38] See Supplemental Material at <http://link.aps.org/supplemental/10.1103/PhysRevLett.108.240404> for a discussion of cloud release energy and heating due to molecule formation.
- [39] M. Barth and W. Zwerger, *Ann. Phys. (N.Y.)* **326**, 2544 (2011).
- [40] S. Zhang and T.-L. Ho, *New J. Phys.* **13**, 055003 (2011).
- [41] J. Bünenmann, W. Weber, and F. Gebhard, *Phys. Rev. B* **57**, 6896 (1998).
- [42] L. Pricoupenko and Y. Castin, *Phys. Rev. A* **69**, 051601 (2004).

# Bibliography

- [1] M. H. Anderson, J. R. Ensher, M. R. Matthews, C. E. Wiemann, and E. A. Cornell. Observation of Bose-Einstein condensation in a dilute atomic vapor. *Science*, 269:198, 1995.
- [2] K. B. Davis, M.-O. Mewes, M. R. Andrews, N. J. van Druten, D. S. Durfee, D. M. Kurn, and W. Ketterle. Bose-Einstein condensation in a gas of sodium atoms. *Phys. Rev. Lett.*, 75:3969, 1995.
- [3] B. DeMarco and D. S. Jin. Onset of Fermi degeneracy in a trapped atomic gas. *Science*, 285(5434):1703–1706, 1999.
- [4] M. Greiner, O. Mandel, T. Esslinger, T. W. Hänsch, and I. Bloch. Quantum phase transition from a superfluid to a Mott insulator in a gas of ultracold atoms. *Nature*, 415:39, 2002.
- [5] S. Nascimbene, N. Navon, K. J. Jiang, F. Chevy, and C. Salomon. Exploring the thermodynamics of a universal Fermi gas. *Nature*, 463:1057, 2010.
- [6] W. Hofstetter, J. I. Cirac, P. Zoller, E. Demler, and M. D. Lukin. High-temperature superfluidity of fermionic atoms in optical lattices. *Phys. Rev. Lett.*, 89:220407, 2002.
- [7] P. Horowitz and W. Hill. *The Art of Electronics*. Cambridge University Press, 1989.
- [8] R. Kubo. The fluctuation-dissipation theorem. *Rep. Prog. Phys.*, 29:255, 1966.

- [9] R. Brown. A brief account of microscopical observations [...], on the particles contained in the pollen of plants [...]. *Edinburgh new Philosophical Journal*, page 358, 1828.
- [10] A. Einstein. Über die von der molekularkinetischen Theorie der Wärme geforderte Bewegung von in ruhenden Flüssigkeiten suspendierten Teilchen. *Annalen der Physik*, 17:549, 1905.
- [11] M. Smoluchowski. Zur kinetischen Theorie der Brownschen Molekularbewegung und der Suspensionen. *Annalen der Physik*, 21:756, 1906.
- [12] G. Breitenbach, S. Schiller, and J. Mlynek. Measurement of the quantum states of squeezed light. *Nature*, 387:471, 1997.
- [13] R. Jördens, N. Strohmaier, K. Günter, H. Moritz, and T. Esslinger. A Mott insulator of fermionic atoms in an optical lattice. *Nature*, 455:204, 2008.
- [14] F. Werner, O. Parcollet, A. Georges, and S. R. Hassan. Interaction-induced adiabatic cooling and antiferromagnetism of cold fermions in optical lattices. *Phys. Rev. Lett.*, 95:056401, 2005.
- [15] C.-S. Chuu, F. Schreck, T. P. Meyrath, J. L. Hanssen, G. N. Price, and M. G. Raizen. Direct observation of sub-Poissonian number statistics in a degenerate Bose gas. *Phys. Rev. Lett.*, 95:260403, 2005.
- [16] J. Estève, C. Gross, A. Weller, S. Giovanazzi, and M. K. Oberthaler. Squeezing and entanglement in a Bose-Einstein condensate. *Nature*, 455:1216, 2008.
- [17] S. Whitlock, C. F. Ockeloen, and R. J. C. Spreeuw. Sub-Poissonian atom-number fluctuations by three-body loss in mesoscopic ensembles. *Phys. Rev. Lett.*, 104:120402, 2010.
- [18] A. Itah, H. Veksler, O. Lahav, A. Blumkin, C. Moreno, C. Gordon, and J. Steinhauer. Direct observation of a sub-Poissonian number distribution of atoms in an optical lattice. *Phys. Rev. Lett.*, 104:113001, 2010.

- [19] E. Altman, E. Demler, and M. D. Lukin. Probing many-body states of ultracold atoms via noise correlations. *Phys. Rev. A*, 70:013603, 2004.
- [20] M. Greiner, C. A. Regal, J. T. Stewart, and D. S. Jin. Probing pair-correlated fermionic atoms through correlations in atom shot noise. *Phys. Rev. Lett.*, 94:110401, 2005.
- [21] S. Fölling, F. Gerbier, A. Widera, O. Mandel, T. Gericke, and I. Bloch. Spatial quantum noise interferometry in expanding ultracold atom clouds. *Nature*, 434:481, 2005.
- [22] T. Rom, Th. Best, D. van Oosten, U. Schneider, S. Fölling, B. Paredes, and I. Bloch. Free fermion antibunching in a degenerate atomic Fermi gas released from an optical lattice. *Nature*, 444:733, 2006.
- [23] N. Gemelke, X. Zhang, C. Hung, and C. Chin. In situ observation of incompressible Mott-insulating domains in ultracold atomic gases. *Nature*, 460:995, 2009.
- [24] W. S. Bakr, J. I. Gillen, A. Peng, S. Fölling, and M. Greiner. A quantum gas microscope for detecting single atoms in a Hubbard-regime optical lattice. *Nature*, 462:74, 2009.
- [25] G. Jo, Y. Lee, J. Choi, C. A. Christensen, T. H. Kim, J. H. Thywissen, D. E. Pritchard, and W. Ketterle. Itinerant ferromagnetism in a Fermi gas of ultracold atoms. *Science*, 325:1521, 2009.
- [26] F. Schwabl. *Quantenmechanik für Fortgeschrittene*. Springer-Verlag, 1997.
- [27] F. Schwabl. *Statistische Mechanik*. Springer-Verlag, 2000.
- [28] F. Wegner. *Statistische Mechanik*. Vorlesungs-Skriptum, 2006.
- [29] S. Ma. *Statistical Mechanics*. World Scientific, 1985.
- [30] W. Greiner, L. Neise, and H. Stöcker. *Thermodynamik und Statistische Mechanik*. Verlag Harri Deutsch, 1993.

- [31] G. E. Astrakharchik, R. Combescot, and L. P. Pitaevskii. Fluctuations of the number of particles within a given volume in cold quantum gases. *Phys. Rev. A*, 76:063616, 2007.
- [32] Y. Castin. Basic theory tools for degenerate Fermi gases. *arXiv*, cond-mat/0612613v2, 2007.
- [33] L. D. Landau, E. M. Lifshitz, and L. P. Pitaevskii. *Statistical Physics, Part 2 (Course of Theoretical Physics; Vol. 9)*. Pergamon Press, 1980.
- [34] D. Pines and P. Nozières. *The Theory of Quantum Liquids, Volume 1*. Addison-Wesley, 1994.
- [35] A. Recati and S. Stringari. Spin fluctuations, susceptibility, and the dipole oscillation of a nearly ferromagnetic Fermi gas. *Phys. Rev. Lett.*, 106:080402, 2011.
- [36] M. Inguscio, W. Ketterle, and C. Salomon, editors. *Proceedings of the International School of Physics Enrico Fermi: Ultra-cold Fermi Gases*. IOS Press, 2007.
- [37] Stefano Giorgini, Lev P. Pitaevskii, and Sandro Stringari. Theory of ultracold atomic Fermi gases. *Rev. Mod. Phys.*, 80:1215–1274, 2008.
- [38] Georg M. Bruun and Charles W. Clark. Ideal gases in time-dependent traps. *Phys. Rev. A*, 61:061601, 2000.
- [39] D. S. Durfee. *Dynamic properties of dilute Bose-Einstein condensates*. PhD thesis, MIT, 1999.
- [40] C. A. Stan. *Experiments with interacting Bose and Fermi gases*. PhD thesis, MIT, 2005.
- [41] Z. Hadzibabic. *Studies of a quantum degenerate fermionic lithium gas*. PhD thesis, MIT, 2003.

- [42] R. Loudon. *The Quantum Theory of Light*. Oxford Science Publications, 2000.
- [43] W. Demtröder. *Laser Spectroscopy*. Springer, 2003.
- [44] H. J. Metcalf and P. van der Straten. *Laser Cooling and Trapping*. Springer, 1999.
- [45] M. Houbiers, H. T. C. Stoof, W. I. McAlexander, and R. G. Hulet. Elastic and inelastic collisions of  $^6\text{Li}$  atoms in magnetic and optical traps. *Phys. Rev. A*, 57:R1497, 1998.
- [46] M. Born and E. Wolf. *Principles of Optics*. Cambridge University Press, 1999.
- [47] B. E. A. Saleh and M. C. Teich. *Fundamentals of Photonics*. Wiley-Interscience, 2007.
- [48] J. W. Goodman. *Speckle Phenomena in Optics*. Ben Roberts and Company, 2006.
- [49] S. Lowenthal and D. Joyeux. Speckle removal by a slowly moving diffuser associated with a motionless diffuser. *Journal of the Opt. Soc. of America*, 61:847, 1971.
- [50] B. DeMarco. *Quantum Behavior of an Atomic Fermi Gas*. PhD thesis, University of Colorado, 2001.
- [51] J. F. Kenney and E. S. Keeping. *Mathematics of Statistics, Pt. 2*. Van Nostrand, 1951.
- [52] Torben Müller, Bruno Zimmermann, Jakob Meineke, Jean-Philippe Brantut, Tilman Esslinger, and Henning Moritz. Local observation of antibunching in a trapped Fermi gas. *Phys. Rev. Lett.*, 105:040401, 2010.
- [53] Jakob Meineke, Jean-Philippe Brantut, David Stadler, Torben Müller, Henning Moritz, and Tilman Esslinger. Interferometric measurement of local spin fluctuations in a quantum gas. *Nature Physics*, 8:455, 2012.

- [54] Y. Castin and F. Werner. The unitary gas and its symmetry properties. *arXiv*, 1103.2851v2, 2011.
- [55] L. Pricoupenko and Y. Castin. One particle in a box: The simplest model for a Fermi gas in the unitary limit. *Phys. Rev. A*, 69:051601, 2004.
- [56] J. J. Sakurai. *Modern Quantum Mechanics*. Addison-Wesley, 1994.
- [57] M. Inguscio, S. Stringari, and C. E. Wieman, editors. *Proceedings of the International School of Physics Enrico Fermi: Bose-Einstein Condensation in Atomic Gases*. IOS Press, 1999.
- [58] R. Kaiser, C. Westbrook, and F. David, editors. *Les Houches Lecture Notes*. Springer, 2001.
- [59] Maxim Olshanii and Ludovic Pricoupenko. Rigorous approach to the problem of ultraviolet divergencies in dilute Bose gases. *Phys. Rev. Lett.*, 88:010402, 2001.
- [60] D. S. Petrov, C. Salomon, and G. V. Shlyapnikov. Weakly bound dimers of fermionic atoms. *Phys. Rev. Lett.*, 93:090404, 2004.
- [61] N. W. Ashcroft and N. D. Mermin. *Solid State Physics*. Brooks / Cole Thomson Learning, 1976.
- [62] S. Jochim, M. Bartenstein, A. Altmeyer, G. Hendl, C. Chin, J. Hecker Denschlag, and R. Grimm. Pure gas of optically trapped molecules created from fermionic atoms. *Phys. Rev. Lett.*, 91:240402, 2003.
- [63] M. Greiner, C. A. Regal, and D. S. Jin. Emergence of a molecular Bose-Einstein condensate from a Fermi gas. *Nature*, 426:537, 2003.
- [64] M. W. Zwierlein, J. R. Abo-Shaeer, A. Schirotzek, C. H. Schunck, and W. Ketterle. Vortices and superfluidity in a strongly interacting Fermi gas. *Nature*, 435:1047, 2005.

- [65] J. W. Goodman. Some fundamental properties of speckle. *J. Opt. Soc. Am.*, 66:1145, 1976.
- [66] A. Keshet. *A Next-Generation Apparatus for Lithium Optical Lattice Experiments*. PhD thesis, MIT, 2012.
- [67] Qijin Chen, Jelena Stajic, and K. Levin. Thermodynamics of interacting fermions in atomic traps. *Phys. Rev. Lett.*, 95:260405, 2005.
- [68] M. W. Zwierlein, C. A. Stan, C. H. Schunck, S. M. F. Raupach, S. Gupta, Z. Hadzibabic, and W. Ketterle. Observation of Bose-Einstein condensation of molecules. *Phys. Rev. Lett.*, 91:250401, 2003.
- [69] G. E. Astrakharchik, J. Boronat, J. Casulleras, and S. Giorgini. Equation of state of a Fermi gas in the BEC-BCS crossover: A quantum Monte Carlo study. *Phys. Rev. Lett.*, 93:200404, 2004.
- [70] D. C. McKay and B. DeMarco. Cooling in strongly correlated optical lattices: prospects and challenges. *Reports on Progress in Physics*, 74:054401, 2011.
- [71] D. W. Snoke. *Solid State Physics: Essential Concepts*. Addison-Wesley, 2008.
- [72] W. Zwirger. Itinerant ferromagnetism with ultracold atoms. *Science*, 325:1507–1509, 2009.
- [73] M. Houbiers, R. Ferwerda, H. T. C. Stoof, W. I. McAlexander, C. A. Sackett, and R. G. Hulet. Superfluid state of atomic  ${}^6\text{Li}$  in a magnetic trap. *Phys. Rev. A*, 56:4864, 1997.
- [74] M. Amoruso, I. Meccoli, A. Minguzzi, and M. P. Tosi. Collective excitations of a degenerate Fermi vapour in a magnetic trap. *Eur. Phys. J. D*, 7:441, 1999.
- [75] L. Salasnich, B. Pozzi, A. Parola, and L. Reatto. Thermodynamics of multi-component Fermi vapors”,. *J. Phys. B: At. Mol. Opt. Phys.*, 33:3943, 2000.
- [76] T. Sogo and H. Yabu. Collective ferromagnetism in two-component Fermi-degenerate gas trapped in a finite potential. *Phys. Rev. A*, 66:043611, 2002.

- [77] R. A. Duine and A. H. MacDonald. Itinerant ferromagnetism in an ultracold atom Fermi gas. *Phys. Rev. Lett.*, 95:230403, 2005.
- [78] Hui Zhai. Correlated versus ferromagnetic state in repulsively interacting two-component Fermi gases. *Phys. Rev. A*, 80:051605, 2009.
- [79] G. J. Conduit and B. D. Simons. Repulsive atomic gas in a harmonic trap on the border of itinerant ferromagnetism. *Phys. Rev. Lett.*, 103:200403, 2009.
- [80] L. J. LeBlanc, J. H. Thywissen, A. A. Burkov, and A. Paramekanti. Repulsive Fermi gas in a harmonic trap: Ferromagnetism and spin textures. *Phys. Rev. A*, 80:013607, 2009.
- [81] I. Berdnikov, P. Coleman, and S. H. Simon. Itinerant ferromagnetism in an atom trap. *Phys. Rev. B*, 79:224403, 2009.
- [82] Xiaoling Cui and Hui Zhai. Stability of a fully magnetized ferromagnetic state in repulsively interacting ultracold Fermi gases. *Phys. Rev. A*, 81:041602, 2010.
- [83] S. Zhang, H. Hung, and C. Wu. Proposed realization of itinerant ferromagnetism in optical lattices. *Phys. Rev. A*, 82:053618, 2010.
- [84] H. Heiselberg. Itinerant ferromagnetism in ultracold Fermi gases. *Phys. Rev. A*, 83:053635, 2011.
- [85] David Pekker, Mehrtash Babadi, Rajdeep Sensarma, Nikolaj Zinner, Lode Pollet, Martin W. Zwierlein, and Eugene Demler. Competition between pairing and ferromagnetic instabilities in ultracold Fermi gases near Feshbach resonances. *Phys. Rev. Lett.*, 106:050402, 2011.
- [86] S. Pilati, G. Bertaina, S. Giorgini, and M. Troyer. Itinerant ferromagnetism of a repulsive atomic Fermi gas: A quantum Monte Carlo study. *Phys. Rev. Lett.*, 105:030405, 2010.

- [87] Soon-Yong Chang, Mohit Randeria, and Nandini Trivedi. Ferromagnetism in the upper branch of the Feshbach resonance and the hard-sphere Fermi gas. *Proc. Natl. Acad. Sci.*, 108:51, 2011.
- [88] One possibility to suppress pair formation is provided by narrow Feshbach resonances. Here the pairs have dominantly closed channel character and therefore a much smaller overlap matrix element with the free atoms. However, narrow Feshbach resonances are characterized by a long effective range and do not realize the Stoner model which assumes short-range interactions.
- [89] Cheng Chin, Rudolf Grimm, Paul Julienne, and Eite Tiesinga. Feshbach resonances in ultracold gases. *Rev. Mod. Phys.*, 82:1225, 2010.
- [90] G. J. Conduit and E. Altman. Effect of three-body loss on itinerant ferromagnetism in an atomic Fermi gas. *Phys. Rev. A*, 83:043618, 2011.
- [91] Cheng Chin and Rudolf Grimm. Thermal equilibrium and efficient evaporation of an ultracold atom-molecule mixture. *Phys. Rev. A*, 69:033612, 2004.
- [92] Xia-Ji Liu, Hui Hu, and Peter D. Drummond. Three attractively interacting fermions in a harmonic trap: Exact solution, ferromagnetism, and high-temperature thermodynamics. *Phys. Rev. A*, 82:023619, 2010.
- [93] K. M. O'Hara, S. L. Hemmer, M. E. Gehm, S. R. Granade, and J. E. Thomas. Observation of a strongly interacting degenerate Fermi gas of atoms. *Science*, 298:2179, 2002.
- [94] C. Menotti, P. Pedri, and S. Stringari. Expansion of an interacting Fermi gas. *Phys. Rev. Lett.*, 89:250402, 2002.
- [95] Gyu-Boong Jo, Ye-Ryoung Lee, Jae-Hoon Choi, Caleb A. Christensen, Tony H. Kim, Joseph H. Thywissen, David E. Pritchard, and Wolfgang Ketterle. Response to comment by Tin-Lun Ho on "Itinerant ferromagnetism in a strongly interacting Fermi gas of ultracold atoms", *Science* 325, 1521 (2009). *arXiv:0910.3419v2*, 2009.

- [96] A. Sommer, M. Ku, G. Roati, and M. W. Zwierlein. Universal spin transport in a strongly interacting Fermi gas. *Nature*, 472:201, 2011.
- [97] Marcus Barth and Wilhelm Zwerger. Tan relations in one dimension. *Annals of Physics*, 326:2544, 2011.
- [98] Shizhong Zhang and Tin-Lun Ho. Atom loss maximum in ultracold Fermi gases. *New J. Phys.*, 13:055003, 2011.
- [99] N. D. Drummond, N. R. Cooper, R. J. Needs, and G. V. Shlyapnikov. Quantum Monte Carlo calculation of the zero-temperature phase diagram of the two-component fermionic hard-core gas in two dimensions. *Phys. Rev. B*, 83:195429, 2011.
- [100] Ville Pietilä, David Pekker, Yusuke Nishida, and Eugene Demler. Pairing instabilities in quasi-two-dimensional Fermi gases. *Phys. Rev. A*, 85:023621, 2012.
- [101] Xia-Ji Liu and Hui Hu. Virial expansion for a strongly correlated Fermi gas with imbalanced spin populations. *Phys. Rev. A*, 82:043626, 2010.
- [102] H. Dong, H. Hu, X. Liu, and P. D. Drummond. Mean-field study of itinerant ferromagnetism in trapped ultracold Fermi gases: Beyond the local-density approximation. *Phys. Rev. A*, 82:013627, 2010.
- [103] C. W. von Keyserlingk and G. J. Conduit. Itinerant ferromagnetism in an interacting Fermi gas with mass imbalance. *Phys. Rev. A*, 83:053625, 2011.
- [104] Chia-Chen Chang, Shiwei Zhang, and David M. Ceperley. Itinerant ferromagnetism in a Fermi gas with contact interaction: Magnetic properties in a dilute Hubbard model. *Phys. Rev. A*, 82:061603, 2010.
- [105] G. Carleo, S. Moroni, F. Becca, and S. Baroni. Itinerant ferromagnetic phase of the Hubbard model. *Phys. Rev. B*, 83:060411, 2011.